NONLINEAR TEMPERATURE DISTRIBUTIONS

Dissertation for the Degree of Ph. D.
MICHIGAN STATE UNIVERSITY
MARSHALL P. CADY, JR.
1976

LIBRARY
Michigan State
University

LIBRARY
Michigan State
University

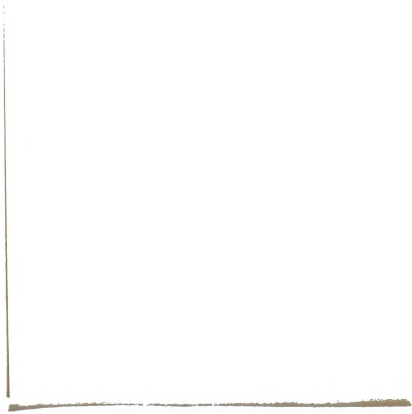

ABSTRACT

NONLINEAR TEMPERATURE DISTRIBUTIONS

By

Marshall P. Cady, Jr.

Pure, one-component fluids can exhibit large nonlinear temperature distributions in nonequilibrium situations in which nearly linear distributions are usually expected. This dissertation includes (a) a theoretical analysis of molecular energy transport mechanisms which can create nonlinear temperature distributions and (b) a Bryngdahl interferometric study of the quantitative aspects of temperature nonlinearities in liquids. The nonequilibrium thermodynamic regimes studied include time-independent and nonconvecting, time-independent and convecting, and time-dependent and convecting.

The possibility that molecular vibrational degrees of freedom can create or contribute to spatial nonlinear, time-independent temperature distributions is explored with a stochastic diffusional energy transport model. Computations indicate that liquids may exhibit temperature jumps at the liquid-boundary interface but that the diffusional mechanism

of energy transport cannot contribute to nonlinearities of significant spatial extent. However, the diffusional mechanism can produce gas phase nonlinearities which extend 0.01 cm from boundaries provided that $P \lesssim 1 \times 10^{-2}$ atm. Computations also show the nonlinear magnitude to be 0.03 K for gases when 1 vibrational degree of freedom in 10^4 at the boundary fails to be described by a Boltzmann distribution. A temperature jump of 0.03 K is expected for liquids when 1 vibrational degree of freedom in 10^2 belongs to the nonequilibrium distribution. The diffusion model has applications in describing energy transport away from catalytic surfaces, near boundaries of polyatomic gases in the "temperature jump" regime, and near boundaries of strongly emitting and absorbing liquids.

The diffusional energy transport model is characterized by energy transport via diffusion of fluid molecules, the Landau-Teller transition probabilities for resonant exchange of vibrational energy during bimolecular collisions, and the assumption of non-Boltzmann distribution of molecular vibrational degrees of freedom at boundaries. The non-Boltzmann distribution is the result of boundary-fluid interactions. Two parameters describing temperature nonlinearity associated with diffusion are deduced. They provide a measure of the spatial extent of the nonlinearity from boundaries and of the magnitude of the nonlinearity.

Bryngdahl interferometry is used to examine temperature distributions in liquids bound by horizontal,

parallel, silver plates which are maintained at different temperatures. For nonconvecting states the linear temperature distributions expected for pure thermal conduction are found at distances greater than 0.3 cm from boundaries for ethyl acetate, benzene, and carbon tetrachloride. However, at shorter distances the distributions are highly nonlinear. As the metal-liquid interface is approached, the temperature gradient increases 4.5% for ethyl acetate, 12.5% for benzene, and 30% for carbon tetrachloride. Full details of the observed temperature distributions and gradient distributions are reported. In addition, we find that the ratio of integrated absolute deviation from linearity($1/\underline{1}\ \int_0^{\underline{1}} |T-T_{3.33}|\,dz$ where $T_{3.33}$ is the solution of $\nabla\cdot k\nabla T = 0$) is 1/2.4/4.7/14.6 for ethyl acetate, benzene, carbon tetrachloride, and water, respectively. The very large integrated absolute deviation exhibited by water is caused by temperature jump phenomena. It appears that the temperature jump is a property of the boundary-liquid system and is not caused by plate temperature control and temperature measurement.

Knowledge of liquid nonlinear temperature distributions makes possible an increase in the accuracy of experimentally determined Soret coefficients, thermal conductivities, and nonisothermally determined refractive index temperature derivatives.

Finally, experimental studies of nonlinear temperature distributions in convecting liquids are presented.

The Rayleigh numbers for the critical flow transitions are found to be $R_I = 1667 \pm 137$, $R_{III} = 3.3 \times 10^4 \pm 12\%$, and $R_{IV} = 4.42 \times 10^4 \pm 14\%$. At R_I a transition from nonconvection to steady state convection occurs; at R_{III} there is a transition from three-dimensional steady flow to three-dimensional time-dependent flow; and at R_{IV} there is a transition from time-dependent flow to time-dependent flow of increased frequency. Bryngdahl interferometry is uniquely suited to the study of the time-dependent phenomena. Frequencies of temperature oscillations are determined via Fourier transform of the Bryngdahl interferometric image autocorrelation function. Four major bands are observed at approximately 10, 30, 90, and 140 min^{-1}. The band intensity is proportional to $\epsilon = \langle \Delta T \rangle_{IV} - \Delta T$ and decays exponentially with angular frequency 75.8 min^{-1}.

NONLINEAR TEMPERATURE DISTRIBUTIONS

By

Marshall P. Cady, Jr.

A DISSERTATION

Submitted to
Michigan State University
in partial fulfillment of the requirements
for the degree of

DOCTOR OF PHILOSOPHY

Department of Chemistry

1976

6/02777

To Sharmaine

ACKNOWLEDGMENTS

I thank Professors F.H. Horne and R.I. Cukier for their efforts to improve the manuscript. In addition, I thank my wife, Sharmaine, whose typing, encouragement, and prodding made this dissertation possible.

Finally, I express recognition of the influence Professor F.H. Horne has had upon my scientific development. The excellence of his lectures in mathematical physics, thermodynamics, and nonequilibrium thermodynamics is admired and has provided the fundamental basis of this dissertation.

TABLE OF CONTENTS

Chapter Page

LIST OF TABLES

Table | Page

LIST OF FIGURES

Figure Page

CHAPTER 1

INTRODUCTION

1.1 Aperçu

The study of nonlinear temperature distributions in pure, one-component fluids provides macroscopic, continuum data on which molecular theories of energy transport processes may be based. Clearly, all temperature distributions in nonequilibrium media are the consequence of molecular energy transport via vibrational, rotational, translational, and electronic degrees of freedom. Because of this relationship between molecular mechanism and macroscopic observation, nonequilibrium thermodynamic studies are an important complement to the modern effort[1,2] to catalog molecular energy levels and transition probabilities.

Particulars of this work include both the conceptual illumination of molecular mechanisms which can cause nonlinear, steady state temperature distributions and Bryngdahl interferometric evaluation of temperature distributions in pure, one-component liquids. The possibility that vibrational degrees of freedom play a contributing role in the establishment of nonlinear, steady state temperature distributions in nonconvecting fluid media is explored in Chapter 2. On the

assumption that the temperature distribution far from the walls of the fluid container is linear, mechanisms are presented which invalidate the steady state Fourier-Laplace equation description of the temperature distribution when wall effects are important. Molecular diffusion and energy flux models of vibrational energy transfer are used to analyze the problem quantitatively. Fluid-dependent parameters characterizing the magnitude of the temperature nonlinearity and its extension from the container-fluid interface are deduced. Energy transport by diffusion is shown to contribute negligibly to nonlinear temperature distributions observed within the liquid phase, but this mechanism may contribute significantly to the establishment of nonlinearities within low pressure gases.

Before experimental evidence of nonlinear temperature distributions in both nonconvecting liquids(Chapter 4) and convecting liquids(Chapter 5) is presented, it is necessary to discuss details of the Bryngdahl interferometer which is used as a temperature probe. This is the purpose of Chapter 3. After a survey of the applications of Bryngdahl interferometry in Section 3.2, details of the optical apparatus, the horizontal parallel plate-cell composite, and experimental procedure are described in Section 3.3. The horizontal parallel plate arrangement heats the liquid cell at either the upper or lower plate and cools it from the opposite plate. This results in a continuous vertical temperature distribution across the liquid which causes refraction of the interferometric light beam. Beam refraction must be accounted for when spatial derivatives of the refractive index are mapped from the unrefined Bryngdahl

interferometric data. The mapping is

$$dW/dz \longrightarrow dn/dz \qquad (1.1)$$

where W, n, and z are the optical path, refractive index, and vertical coordinate, respectively. The left side of Equation 1.1 is called the unrefined data; the right is called the refined data. The mathematical mapping procedures are established in Section 3.4. Once the refined data have been mapped from the unrefined Bryngdahl interferometric data, one can either assume knowledge of the temperature gradient and compute the temperature derivative of the refractive index with the chain rule expression

$$dn/dT = (dn/dz)/(dT/dz) \qquad (1.2a)$$

or assume knowledge of the temperature derivative of the refractive index and compute the temperature gradient with the equation

$$dT/dz = (dn/dz)/(dn/dT). \qquad (1.2b)$$

The alternative mathematical prodecures are established in Sections 3.5 and 3.6, respectively.

Direct interferometric observations of nonlinear, steady state temperature distributions in nonconvecting liquids are reported in Chapter 4. After an introductory discussion of linear and nonlinear distributions in Section 4.1, the qualitative and quantitative features of nonlinearities exhibited by ethyl acetate, benzene, and carbon tetrachloride are presented in Section 4.2. Besides a thorough detailing of problems inherent in nonequilibrium experimental studies, Section 4.2 includes data which lead to (1) correlation of the dependence of the nonlinearity upon the impressed temperature

difference between the liquid boundaries, (2) specification of the spatial domain of the nonlinearity, and (3) comparison of the relative magnitudes of exhibited nonlinearities between liquids. All measurements are at ambient pressure. Mean temperatures are between 24°C and 29°C, and boundary temperature differences are between 2°C and 13°C for the 1.349 cm high liquid cell. In Section 4.3 the temperature dependence of the refractive index of water between 24°C and 40°C at 632.8 nm and atmospheric pressure is obtained. Temperature gradients range from 4 deg cm^{-1} to 16 deg cm^{-1}. Results comparable to isothermal determinations of the temperature dependence are found when the data analysis does not include the measured temperature difference between the upper and lower plates of the horizontal parallel plate system. The presence of temperature jumps would explain discrepancies which occur when the temperature difference is used in the analysis.

Finally, the Bryngdahl interferometric examination of convecting thermodynamic states exhibited by water is presented in Chapter 5. There are four major features. These include the determination of the critical Rayleigh number for two types of transitions: the transitions from nonconvection to steady state convection and from steady state convection to time-dependent, turbulent convection. The nonlinear temperature distributions between these transitions are mapped. Frequencies of aperiodic motions in the turbulent states are determined.

1.2 The Interior Conducibility

The nonequilibrium description of temperature(T) in a one-component, pure, nonreacting fluid depends upon two fundamental statements. The first is the law of conservation of energy:

$$\dot{E} + \nabla \cdot \underset{\sim}{J}^i = \sigma^i \tag{1.3}$$

where $E = E(\underset{\sim}{r},t)$, $\underset{\sim}{J}^i = \underset{\sim}{J}^i(\underset{\sim}{r},t)$, and $\sigma^i = \sigma^i(\underset{\sim}{r},t)$ are the specific internal energy per unit volume, the i'th form of heat flux, and the i'th form of energy source per unit volume per unit time, respectively. The heat flux and energy source have been given the superscript i because differing physical interpretations and mathematical descriptions of the energy source are associated with nonequivalent heat flux. The i'th form of the energy source is associated with the i'th form of the heat flux.

The second important statement is a phenomenological relationship between heat flux and temperature gradient. For isotropic media it is

$$J^i = -k^i \nabla T \tag{1.4}$$

where $k^i = k^i(r)$ is the i'th form of the conductivity.

For temperature fields which are uniform in the horizontal plane and for which $\dot{E} = 0$, Equations 1.3 and 1.4 simplify to

$$(d/dz)k^i(dT/dz) = -\sigma^i. \tag{1.5}$$

The solution of this differential equation subject to the boundary conditions

$$T(0) = T_U \quad \text{and} \quad T(\underline{l}) = T_L \tag{1.6}$$

is the temperature field. $\underline{l}$ is the distance between

horizontal boundaries. Equation 1.5 is also used in the experimental evaluation of k^i. One integration yields:

$$-k^i(z) = (J_T + \int \sigma^i(z)dz)/(dT(z)/dz) \qquad (1.7)$$

where J_T is the total heat flux in the z direction and will be called the heat flux. The heat flux, $dT(z)/dz$, and $T(z)$ are experimentally determined; then, $\sigma^i(z)$ is assumed and $k^i(z)$ computed with Equation 1.7. A final mapping $k^i(z) \longrightarrow k^i(T)$ yields the i'th form of the conductivity.

A particularly important form of the conductivity is given by Fourier's[3] "interior conducibility," $k(T)$, which is defined by

$$J_z = -k(dT/dz). \qquad (1.8)$$

This constitutive conductivity form is recognized by many modern authors[4-11] of nonequilibrium thermodynamics. There are two criteria to help with the deduction of the energy source form(hereafter called the energy source) which is conjugate to the interior conducibility. The first is due to Truesdell(as reported by Petroski[8]): the energy source is determined by given functions E and $\underset{\sim}{J}$ and Equation 1.3. Secondly, we wish to construct the interior conducibility to be a property of the media being studied. Therefore, the interior conducibility must describe energy transport by all possible modes of energy transport solely characteristic of that media. Energy transport modes associated wtih container walls and the external world are not described by the interior conducibility. Very little is known about the

energy source,[8] but with these criteria the necessary concepts will be developed in the next section.

The multitude of possible energy transport mechanisms is illustrated by the interior conducibility of amorphous silica in Figure 1.1. At very low temperatures $k \sim T^3$. This dependence is the result of phonon processes for which

$$k \sim CVL \tag{1.9}$$

where C is the heat capacity per unit volume, V an averaged phonon velocity, and L an averaged phonon mean path. At low temperatures L is constant because of crystal boundary and grain size restrictions; the temperature dependence of Equation 1.9 is then determined by the heat capacity. At low temperatures this dependence is the famous T^3-law of the Debye theory of heat capacity of crystals. With increasing temperature, a second region of extreme complexity is found which is called "the knee." The knee is apparently caused by resonance scattering of phonons by local defects.[12] At still higher temperature a very broad region exists in which the interior conducibility is very weakly dependent upon temperature. In this region k is limited by phonon-phonon processes and by the relative inability of many of the vibrational modes, due to high spatial localization, to transmit energy. Finally, at very high temperature there is a fourth region of strong T^3 dependence;[13-16] energy transport by photon processes have become very important. A photon or radiation transport process is to be understood as either the induced or spontaneous emission of a photon

Figure 1.1

Qualitative features of the interior conducibility, k(T), of amorphous silica.

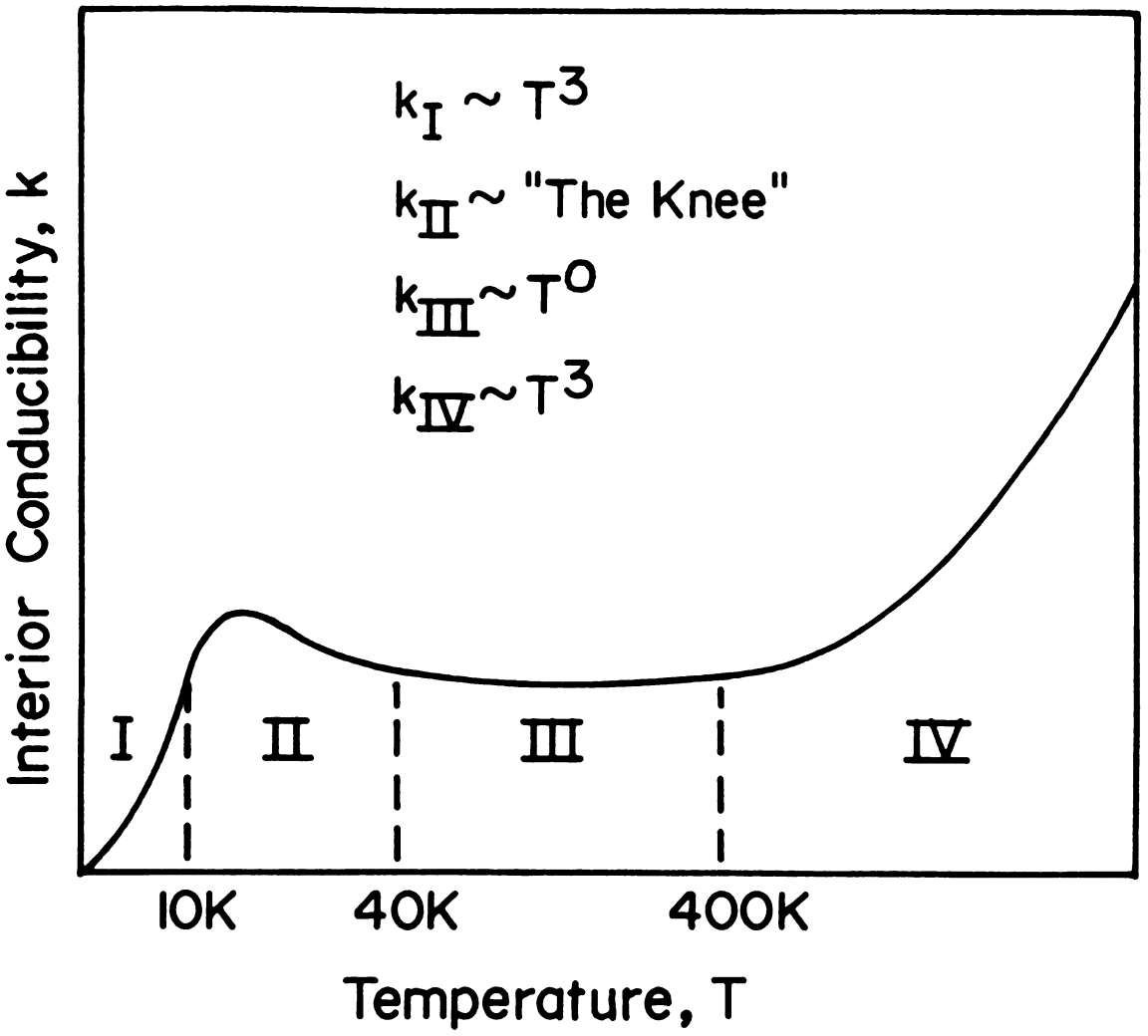
$k_I \sim T^3$
$k_{II} \sim$ "The Knee"
$k_{III} \sim T^0$
$k_{IV} \sim T^3$
Interior Conducibility, k
I
II
III
IV
10K
40K
400K
Temperature, T

by a degree of freedom of the medium and the absorption of that photon by another degree of freedom. Vibrational degrees of freedom are major contributors to this mechanism via infrared photons.

The second major conductivity form is called the "thermal conductivity." In this form the conjugate energy source contains all radiation transport processes, both those in which the photons originate within the medium and those in which the photons originate in the external world. Energy transport processes due solely to thermal motion of the elementary particles of the media are described by the thermal conductivity.[17-21] Our objection to this division of conduction and radiation is based on the presupposed ability to write mathematically and nonphenomenologically a term describing all photon processes. This term is necessary in the Equation 1.7 evaluation of the thermal conductivity. By this procedure each photon model yields a characteristic thermal conductivity and those of different laboratories are impossible to compare properly unless full computational details are published. We believe that once any model of radiation transport for a particular medium has been experimentally proven, then the above division of conduction and radiation becomes a valid procedure. This, however, is not the usual practice. For the history of the separation of conduction, radiation, and convection see Brush;[22] for the first suggestion that conductivity theory can also include radiation transport, see Stokes.[23]

1.3 The Energy Source

Because the interior conducibility describes all energy transport processes characteristic of a given media, the energy source is zero far from boundaries and the external world. In this domain Equation 1.5 becomes the Fourier-Laplace equation:

$$(d/dz)k(dT/dz) = 0. \qquad (1.10)$$

The interior conducibilities of gases and liquids are very much like $k_{III}(T)$ of Figure 1.1; they exhibit a very weak temperature dependence in a broad temperature region which may be called the "ordinary temperatures." For example, for gaseous carbon monoxide at 1 atm: $9 \times 10^{-3}\ K^{-1} \geqslant (1/k)(dk/dT) \geqslant 6 \times 10^{-4}\ K^{-1}$ when $90\ K \leqslant T \leqslant 1100\ K$.[24,25] For carbon tetrachloride at 1 atm: $1.7 \times 10^{-3} K^{-1} \leqslant -(1/k)(dk/dT) \leqslant 2.2 \times 10^{-3} K^{-1}$ when $255\ K \leqslant T \leqslant 378\ K$.[26] This demonstrates that for liquids and gases subjected to temperature differences of the order of 10 deg cm^{-1}, thermal conducibilities are essentially constant at ordinary temperatures. Thus, the temperature of fluids far from boundaries is expected to be the solution of the Laplace equation:

$$T(z) \simeq a + bz \qquad (1.11)$$

where a and b are constants. This linear relationship is a consequence of the absence of an energy source term in Equation 1.10. Thus, Equation 1.11 emphasizes that the study of nonlinear temperature distributions in nonconvecting, steady state fluids must be the theoretical and experimental pursuit of the concepts behind the existence of non-zero energy source, source magnitude, and spatial domain of the source.

There are a number of nonlinear temperature distribution studies at ordinary temperatures and pressure (~1 atm). For a review of nonlinear observations within liquids see Section 4.1; see Figure 4.1 for an example of the nonlinearity within carbon tetrachloride. Nonlinearities at ordinary temperatures and pressure have also been found within some gases. In 1964 Gille and Goody[27] used horizontal aluminum boundary plates spaced 2 cm apart and a Michelson interferometer to study temperature distributions in dry air and ammonia. Linear temperature profiles were found at all distances from boundaries for dry air. Ammonia, however, displayed nonlinear temperature profiles. The nonlinearities were found to be antisymmetric about the intermediate vertical coordinate with a negative deviation from linearity on the half closest to the heated boundary and a positive deviation on the half closest to the cooled boundary. A maximum in the deviation from linearity appeared at about 0.4 cm from the boundaries. It was 0.18°C at 0.7 atm and 0.21°C at 1.3 atm. The nonlinear temperature profiles are explained on the basis of absorption and re-emission of radiation from plates and molecular diffusion. Schimmel et al[28] have used Mach-Zehnder interferometry to deduce boundary temperature gradients in pure gaseous CO_2, N_2O, and mixtures of CO_2-CH_4 and CO_2-N_2O in a cell bound by horizontal aluminum plates 2.55 cm apart. They report that for N_2O at a temperature difference between plates of 10.7°C and a mean temperature of 33°C the ratios of boundary temperature

gradient to the gradient predicted by Equation 1.11 are 1.09, 1.13, 1.17, 1.20, and 1.20 at pressures of 0.25 atm, 0.50 atm, 1.00 atm, 2.00 atm, and 3.00 atm, respectively. The ratios for CO_2 behave similarly with pressure, but are somewhat smaller. These nonlinearities are attributed to radiation transport processes. Experimental studies have shown the nonlinear phenomena to be important in vertical plate systems containing pure ammonia[29] and nitrogen-ammonia mixtures.[30]

The final example of nonlinear temperature distribution is provided by the observations in gases at low pressure ($\lesssim 10^{-2}$ atm) of what is called "temperature jump" and by the association of temperature jump with gas-wall thermal accommodation. For the history and early development of the concept of temperature jump see References 31 and 32; for the association with thermal accommodation see References 33-36; for the Boltzmann equation approach to the problem see References 37 and 38. We present a new conceptualization of the mechanism behind this nonlinearity.

Consider a gas bound by two parallel plates of infinite extent. These plates are maintained at different temperatures with the "lower" wall having lower temperature, and they are far enough apart that at intermediate distances from them all energy transport is due solely to the characteristics of the gas. Figure 1.2A depicts energy transport by thermal motion at these intermediate distances. The indicated particle positions are those of successive

Figure 1.2

Energy transport by translational degrees of freedom. The indicated positions of molecules labeled 1 and 2 are those at successive collisions.

(A) Transport far from walls.

(B) Transport in the presence of a reflecting boundary. See text.

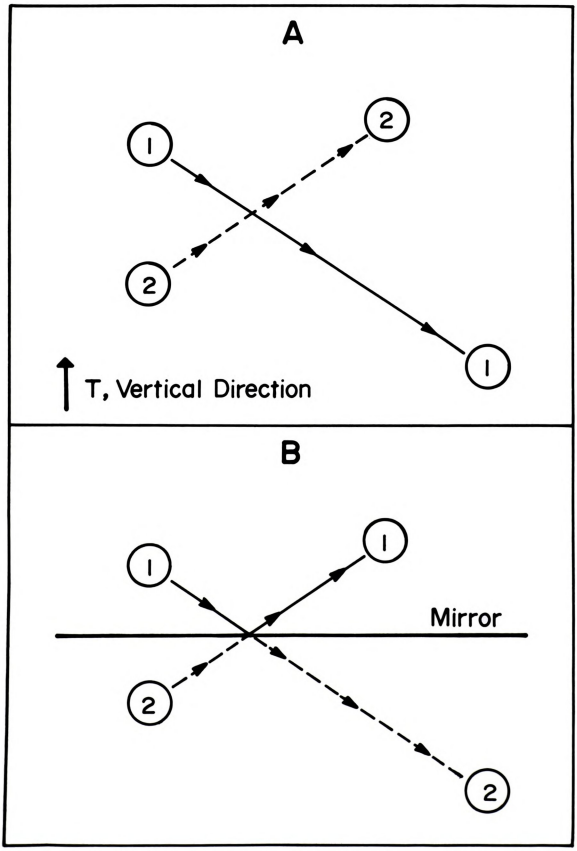
A
1
2
2
1
T, Vertical Direction
B
1
1
Mirror
2
2

gas molecule-molecule collisions. These translational motions and collisions transport thermal energy. For example, the motion and subsequent collision of molecule 1 results in the effective heating of the horizontal layer of the collision; the motion and subsequent collision of molecule 2 effectively cools the horizontal layer of the collision. All such energy transport processes are described by the interior conducibility. Suppose a perfect mirror which reflects molecules specularly and elasticly is placed between molecules 1 and 2, and then energy transport processes are altered. Molecule 1 is now reflected by the mirror to the collision indicated in Figure 1.2B. But the interior conducibility being ignorant of the mirror's presence describes the origin of the colliding molecule as corresponding to the initial position of molecule 2. This is the mirror image of the initial position of molecule 1. The interior conducibility is assigning less energy to the colliding molecule than it actually has. Thus, the temperature distribution near the lower boundary displays a positive deviation from linearity; the energy source is positive in this domain. Now, considering the reflection of molecule 2, molecule 2 is reflected into a collision but carries less energy into that collision than predicted by the interior conducibility. The interior conducibility describes the reflected molecule as having originated at the initial position of molecule 1. This position corresponds to a horizontal layer of higher temperature and, therefore, higher

energy than the horizontal layer of the true initial position of the reflected molecule. Thus, the temperature distribution near the upper boundary must display a negative deviation from linearity; the energy source is negative.

This conceptualization has assumed that the linear temperature distribution observed in the gas far from boundaries is maintained by some unspecified mechanism. On this basis it analyzes the effect of perfect mirrors which have a zero thermal accommodation coefficient(no energy is transferred from mirror to molecule during collision). This does not correspond to any possible laboratory experiment. However, within the framework of the model it can be easily reasoned that (1) the negative (positive) deviation from linearity prediction of this model at the upper(lower) boundary represents the maximum obtainable and (2) negative(positive) deviation from linearity at the lower(upper) boundary is not possible for any boundary-gas system which has a thermal accommodation coefficient between 0 and 1. The thermal accommodation coefficient is defined as being equal to $(T_i-T_r)/(T_i-T_w)$ where T_i corresponds to the temperature of molecules incident upon a wall, T_r corresponds to the temperature of molecules reflected by a wall, and T_w is the temperature of the wall.

Of course this conceptualization can be made physically realistic through the inclusion of adsorption,

desorption, and inelastic scattering of molecules by boundaries. The prescription for the mathematical development of the energy source is clear, however. It is the sum of energy transport processes which are occurring because of the presence of walls minus those energy transport processes which are described by the interior conducibility but are not occurring because of the presence of walls.

Nonlinear temperature distributions result from radiation energy transport via mechanisms which are analogous to the above translational model. This is discussed in Section 4.4. An analogous mechanism of phonon reflection and bulk phonon-grain surface phonon interaction may also be responsible for the belief that the Fourier heat law is not valid at very low temperatures in amorphous solids.[16] In this case the energy source grows with decreasing temperature.

CHAPTER 2

MOLECULAR VIBRATIONAL CONTRIBUTIONS TO NONLINEAR TEMPERATURE DISTRIBUTIONS NEAR WALLS

2.1 Introduction

In this chapter we examine quantitatively the possibility that vibrational degrees of freedom of a gas or a liquid contribute to spatial nonlinear temperature distributions within a single component fluid in the nonflowing steady state. A model in which molecular vibrational energy is transported during diffusion of molecules is considered in detail. Computations indicate that the diffusional mechanism of energy transport cannot contribute to nonlinearities of significant spatial extent within dense media. However, the diffusional mechanism can produce gas phase nonlinearities which extend 0.01 cm from boundaries provided that $P \lesssim 1 \times 10^{-2}$ atm. On the assumption of a non-Boltzmann distribution of molecular vibrational degrees of freedom at boundaries, computations show the nonlinear magnitude to be 0.03 K for gases when 1 vibrational degree of freedom in 10^4 at the boundary fails to be described by a Boltzmann distribution. A temperature jump at a liquid-boundary interface is expected when 1 vibrational degree of freedom in 10^2 belongs to the

nonequilibrium distribution.

To explore the possibility that the interaction between vibrational degrees of freedom of the fluid and the wall can result in nonlinear temperature distributions, consider Figure 2.1. The coordinate z measures distance from the upper plate, which is considered to extend to ($\pm$) infinity in the (x,y) plane. The distance between the two infinite plates is l. The upper plate is maintained at temperature T_U while the lower is at temperature T_L, with T_U T_L. Now imagine the fluid as being divided into layers, each layer having width z and the ith layer being associated with the temperature T(i).

Let the jth layer be far enough away from the wall that wall effects are negligible. The transfer of energy on the molecular level can be envisioned as follows: Energy is continually being transferred from the jth layer to the layers j+1 and j-1. For example, when a molecule goes from the jth layer to the layer j+1, it effectively heats layer j+1 because its translational, rotational, and vibrational degrees of freedom are distributed at T(j), which is greater than T(j+1). Once in layer j+1, this excess energy is dissipated. Conversely, when a molecule undergoes the layer transition $j+1 \rightarrow j$, the jth layer is cooled. Energy is also transferred via emission and absorption of photons between layers. Far from walls Fourier's interior conduci-

Figure 2.1

The horizontal plate arrangement.

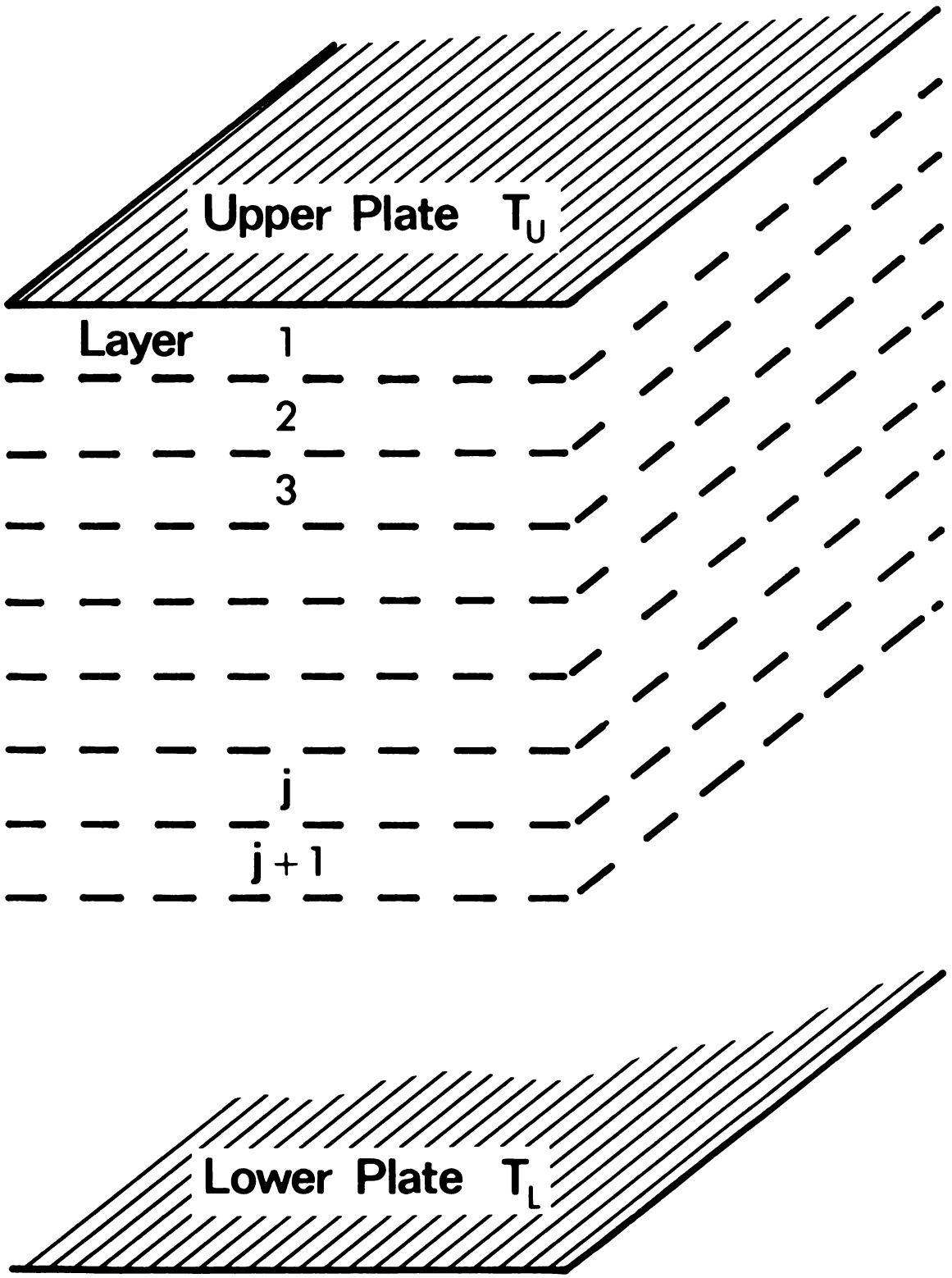
Upper Plate T_U
Layer 1
2
3
j
j + 1
Lower Plate T_L

bility incorporates all such processes, and Equation 1.10 describes the temperature distribution. There is no experimental evidence to the contrary.

Near the wall, however, the Fourier-Laplace equation may fail. For example, a molecule of the first layer is prevented from entering the "zeroth" layer by the presence of the wall. When reflected back to the first layer, it may have a translational energy corresponding to T_U but have its original vibrational energy distributed at temperature T_1. Since this reflected "reentry molecule" does not have the vibrational temperature T_U, where $T_U > T_1$, layer 1 exhibits a temperature lower than that predicted by $\nabla^2 T = 0$ in the steady state. Next to the lower plate, a reflected molecule may have its vibrational energy distributed at a temperature higher than T_L. As a consequence, the layers next to the lower wall will exhibit temperatures higher than that predicted by $\nabla^2 T = 0$. This is one way in which walls might interact with vibrational degrees of freedom to produce a nonlinear temperature distribution. Analogously, reflection by the walls of photons which have been emitted by vibrational degrees of freedom of the fluid results in nonlinear temperature distributions qualitatively identical to the temperature distributions which result from molecular reflection. Also, if the upper wall emits and absorbs photons at rates and extents different from the fluid at

the same temperature, it is possible that there is a difference in the net number of photons absorbed by the vibrational degrees of freedom in layers near the wall beyond that described by $\nabla^2 T = 0$ in the steady state. One final mechanistic example is that of a wall which catalyzes the production of molecules in higher vibrational states. Upon reentry into the layer next to the wall these molecules heat the layer with a resulting nonlinear temperature distribution.

In the following sections, the interaction between the fluid and the wall is not directly analyzed. Rather, it is proposed that these interactions, whatever they may be, result in a non-Boltzmann distribution of vibrational energy in the layer adjoining the wall. Furthermore, it is assumed that this nonequilibrium distribution is known. Temperature distributions can then be calculated once the energy source term which causes deviation from the Fourier-Laplace temperature description has been evaluated. Specific models of vibrational energy transfer are used to evaluate the energy source. The number of nonequilibrium molecules at the boundary needed to achieve deviations from linearity of 10^{-2} K at ordinary temperatures and pressures is estimated, and parameters which determine the thickness of the nonlinear boundary layer are deduced.

The concepts used to develop the above nonequilibrium problem are stochastic: the quantities of interest are probabilities and averages rather than classical deterministic quantities. Much of the mathematics and many of the stochastic concepts developed by Rubin, Shuler, and Montroll are applied directly.[1-5] The models developed belong to class of models which include first-passage time problems, harmonic oscillator relaxation in a heat bath, relaxation of two interacting systems of harmonic oscillators, relaxation of Rayleigh and Lorentz gases, reaction kinetics, and nucleation theory. Reviews of these stochastic processes are available.[6-13]

2.2 Model 1: The Diffusion Model

The time-independent temperature distribution is described by Equation 1.5:

$$k(d^2T/dz^2) = -\sigma \qquad (2.1)$$

where k is the temperature-independent interior conducibility and σ is the energy source which vanishes far from the boundaries. In order to describe temperature distributions in all domains, including that in which walls play an important role, we assert that we may divide the one

component fluid into two systems, the first of which is the "heat bath" (HB) system. The heat bath system of the ith layer has all degrees of freedom, vibrational included, distributed in a Boltzmann distribution at temperature T(i). Thus, the heat bath system is associated with the measured temperature T.

The second system is the system of interest(SI). The system of interest of the ith layer does not have its vibrational degrees of freedom distributed in a Boltzmann distribution at temperature T(i). Rather, the distribution is a nonequilibrium distribution which depends on the nature of the interaction between fluid and wall. The system of interest also interacts with the heat bath system via molecular collisions and perhaps radiative transfer, i.e., exchange of photons between HB and SI. This interaction results in a source of energy for the heat bath system, $\sigma(z)$. In order to evaluate the energy source, models must be developed which enable one to describe the number density of the vibrational states of the system of interest as a function of the spatial coordinate subject to a knowledge of the vibrational energy distribution at z=0 and z=1, i.e., subject to boundary conditions on the distributions. Once the vibrational distributions have been completely determined, it is possible to write the energy source term of the bath system and solve Equation 2.1 for the temperature distribution subject to the boundary conditions $T(z) = T_U$ at $z = 0$ and $T(z) = T_L$ at $z = 1$.

The first model, the diffusion model, has the following characteristics:

(a) Both the system of interest(SI) and the heat bath system(HB) are composed of harmonic oscillators of frequency υ. ρ_k is the number of SI molecules per unit volume in the kth vibrational state, and $\rho_k = \rho_k(\underline{r},t)$.

(b) The density of SI molecules is such that SI molecules collide only with HB molecules and never with other SI molecules. In these SI-HB molecular collisions, resonant transfer of vibrational energy is possible. Furthermore, we assume the Landau-Teller[14] transition probabilities per collision:

$$P_{n,m} = P_{1,0}((n+1)\delta_{m,n+1} + n\delta_{m,n-1}) = P_{m,n}, \qquad (2.2)$$

where $P_{n,m}$ is the probability per collision that a molecule originally in the nth harmonic state will undergo transition to the mth harmonic state, and $\delta_{m,n}$ is the Kronecker delta,

$$\delta_{m,n} = \begin{cases} 0 \text{ if } m \neq n \\ 1 \text{ if } m = n \end{cases} \qquad (2.3)$$

See References 7 and 9 for a more detailed discussion of Equation 2.2. For more recent developments, see References 15-17.

(c) SI molecules in the nth vibrational state diffuse at the rate $D\nabla^2\rho_n$, where D is the diffusion coefficient and is temperature independent.

Because of these characteristics, the rate of change of ρ_n at position $\underset{\sim}{r}$ can be decomposed into the sum of a diffusion term and an SI-HB interaction term. The SI-HB interaction term is given in Reference 4. The result is

$$(\partial\rho_n/\partial t) = (\partial\rho_n/\partial t)_{\text{diffusion}} + (\partial\rho_n/\partial t)_{\text{SI-HB}} \qquad (2.4a)$$

where

$$(\partial\rho_n/\partial t)_{\text{diffusion}} = D\nabla^2\rho_n \qquad (2.4b)$$

by characteristic (c), and

$$(\partial\rho_n/\partial t)_{\text{SI-HB}} = K(1-e^{-\theta})^{-1}(ne^{-\theta}\rho_{n-1} + (n+1)\rho_{n+1} - ((n+1)e^{-\theta} + n)\rho_n) \qquad (2.4c)$$

by characteristic (b). In the last equation, $\theta = (h\upsilon/kT)$, where h and k are the Planck and Boltzmann constants, respectively, υ is the vibrational frequency of the molecules, and T is the temperature at $\underset{\sim}{r}$. Both the diffusion constant and the interaction constant, K, are assumed to be temperature independent. For the steady-state case, Equation 2.4 becomes

$$D\nabla^2\rho_n + K(1-e^{-\theta})^{-1}(ne^{-\theta}\rho_{n-1} + (n+1)\rho_{n+1} - ((n+1)e^{-\theta} + n)\rho_n) = 0. \qquad (2.5)$$

The solution of this equation requires two boundary conditions: the vibrational distribution of SI at z = 0 and that at z = $\underline{1}$. In order to apply Montroll's and Shuler's[4] Fourier series solution to the problem, SI must first be separated into two systems. The first system is the nonequilibrium

distribution associated with the presence of the upper wall. Its vibration number density distribution is designated as $\{s_j\}$. The second nonequilibrium distribution is that associated solely with the presence of the lower wall. Its vibrational number density distribution is designated as $\{r_j\}$. The set $\{s_j\}$ satisfies Equation 2.5 in the coordinate system originating from the upper wall and also satisfies the distribution boundary condition on the upper wall. Similarly, the set $\{r_j\}$ satisfies Equation 2.5 in the coordinate system originating from the lower wall and also satisfies the distribution boundary condition on the lower wall. When the nonequilibrium distribution associated with both walls relaxes to a Boltzmann distribution within the distance $\underline{1}$, SI is the sum of these two distributions. We now make the assumption that SI is this simple sum. This is not a very restrictive assumption when SI is a small fraction of HB. For instance, suppose that SI is 1% of HB at the upper surface and that SI-HB interactions are negligibly weak. In such a case the nonequilibrium distribution associated with the upper wall is altered by 1% at the lower wall due to the presence of the lower wall. The fraction of molecules involved is then a mere 0.01% of HB, a number which is negligible relative to the number of molecules in the nonequilibrium distribution associated with the lower wall. Later it will be shown that either the nonequilibrium distributions relax well within the distance $\underline{1}$, or that SI is a small fraction of HB. With the two systems of SI

clearly defined, Equation 2.5 becomes

$$D\nabla^2 s_n + K(1-e^{-\theta})^{-1}(ne^{-\theta}s_{n-1} + (n+1)s_{n+1} - ((n+1)e^{-\theta} + n)s_n) = 0 \qquad (2.6)$$

which can be solved subject to the boundary condition $s_j(z) = s_j(0)$ at $z = 0$. The set $\{r_j\}$ satisfies an identical equation. To put this into dimensionless form, we make the following definitions:

$$\zeta = c_1 z/\underline{l},\ x_j(\zeta) = s_j(\zeta)/\sum_i s_i(\zeta),\ w_j(\zeta) = r_j(\zeta)/\sum_i r_i(\zeta),$$

$$c_1 = (K\underline{l}^2/D)^{1/2} \qquad (2.7)$$

Furthermore, we constrain $\sum_i s_i(\zeta)$ and $\sum_i r_i(\zeta)$ to equal $\sum_i s_i(0)$ and $\sum_i r_i(c_1)$, respectively; $\{x_i\}$ and $\{w_i\}$ are then probabilities. In accordance with the assumed form of SI, these probabilities must relax to a Boltzmann distribution far from their walls of origin. Equation 2.6 then becomes

$$(1-e^{-\theta})(d^2x_n/d\zeta^2) + (ne^{-\theta}x_{n-1} + (n+1)x_{n+1} - ((n+1)e^{-\theta} + n)x_n) = 0. \qquad (2.8)$$

It is easily shown that the variation of θ with ζ in Equation 2.8 is negligible to within 1% for $\underline{l} \leq 1$ cm when $\Delta T/\underline{l} \lesssim 5$ deg/cm at ordinary temperature. Since this corresponds to the usually experimental condition, we hereafter restrict ourselves to this case. With these conditions the Fourier solution of Equation 2.8 is(see Appendix)

$$x_n(\zeta) = \sum_{k=0}^{\infty} a_k^{(U)} \underline{l}_n(k) e^{-k^{1/2}\zeta} \tag{2.9a}$$

$$\underline{l}_n(v) = F(-n, v+1, 1; 1-e^{-\theta}) = e^{-n\theta} \sum_{\beta=0}^{\infty} (1-e^{\theta}) \binom{n}{\beta}\binom{v}{\beta} \tag{2.9b}$$

$$a_k^{(U)} = (1-e^{-\theta}) \sum_{m=0}^{\infty} \underline{l}_k(m) x_m(0). \tag{2.9c}$$

Comparison of this solution with the Appendix 1 solution of Montroll and Shuler[4] shows that only the exponential power is different, in that the square root is now required. This difference is a consequence of the diffusion differential equation being second order. In these equations, F(a, b, c; z) is the hypergeometric function,[18] and the binomial coefficients have the usual meaning,

$$\binom{n}{v} = \begin{cases} n!/v!(n-v)! & \text{if } n \geq v \\ 0 & \text{if } n < v \text{ or } v < 0. \\ 1 & \text{if } v = 0 \end{cases} \tag{2.10}$$

$x_m(0)$ is the boundary condition imposed on the reduced distribution function at $\zeta = 0$. $\underline{l}_n(v)$ is the Gottlieb polynomial.[19]

Figure 2.2 is a representation of the steady-state solution of the nonequilibrium distribution associated with the wall at $\zeta = 0$. By assumption, this distribution is independent of any effects related to the physical presence of the wall at $\zeta = c_1$. Figure 2.2 shows that the delta distribution center upon $n = 4$ at $\zeta = 0$ rapidly broadens and shifts toward the equilibrium distribution with increasing ζ. Intuitively this result is expected since

Figure 2.2

The probability distribution $\{x_n(\zeta)\}$ for various ζ when $\theta = 1$ and $x_4(0) = 1$.

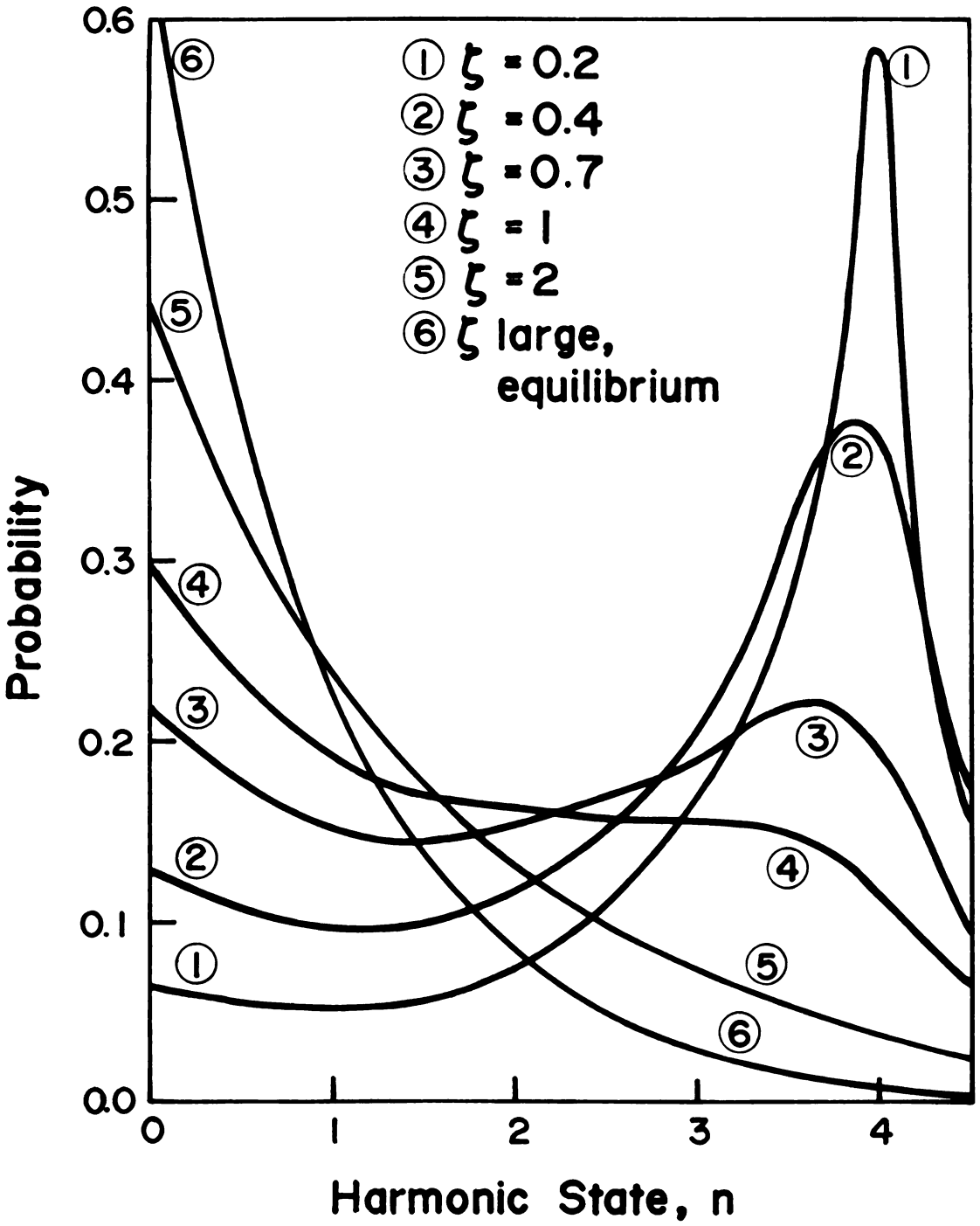
0.6
0.5
0.4
0.3
0.2
0.1
0.0
Probability
0
1
2
3
4
Harmonic State, n
① ζ = 0.2
② ζ = 0.4
③ ζ = 0.7
④ ζ = 1
⑤ ζ = 2
⑥ ζ large, equilibrium

the layers farther removed from the wall indicate the presence of the wall to a lesser degree. However, at $\zeta = 3$ the deviation from the equilibrium distribution is still significant. The figure indicates that molecules of the system leave the surface at $\zeta = 0$ with far more vibrational energy than the average heat bath molecules possess, gradually transfer this energy to heat bath molecules in collisions as they diffuse away from the surface, and approach the equilibrium distributions of heat bath layers far from the wall.

The solution of the distribution $\{w_j\}$ is analogous to that of Equation 2.9, *viz.*,

$$w_n(\zeta) = \sum_{k=0}^{\infty} a_k^{(L)} \underline{l}_n(k) e^{-k^{1/2}(c_1-\zeta)} \qquad (2.11a)$$

$$a_k^{(L)} = (1-e^{-\theta}) \sum_{m=0}^{\infty} \underline{l}_k(m) w_m(c_1) \qquad (2.11b)$$

$w_m(c_1)$ is the boundary condition imposed upon the nonequilibrium distribution associated with the lower wall at $\zeta = c_1$.

When the energy of the nth harmonic state is $E_n = h\nu(n+1/2)$, the steady-state source term of Equation 2.1 is given by

$$\begin{aligned}
\sigma &= -\sum_{n=0} E_n((\partial r_n/\partial t)_{\text{HB-SI}} + (\partial s_n/\partial t)_{\text{HB-SI}}) \\
&= \sum_{n=0} E_n((\partial r_n/\partial t)_{\text{diffusion}} + (\partial s_n/\partial t)_{\text{diffusion}}) \\
&= D \sum_{n=0} E_n(\nabla^2 r_n + \nabla^2 s_n) \\
&= D \sum_{n=0} E_n((\sum_j r_j(c_1))\nabla^2 w_n + (\sum_j w_j(0))\nabla^2 x_n). \qquad (2.12)
\end{aligned}$$

Integration of Equations 2.1 and 2.12, with the boundary conditions $T(\zeta) = T_U$ at $\zeta = 0$ and $T(\zeta) = T_L$ at $\zeta = c_1$, yields the temperature equation:

$$T(\zeta) = T_U - (T_U - T_L)(\zeta/c_1) + c_2 \sum_j s_j(0) H(\zeta) \tag{2.13a}$$

where

$$H(\zeta) = \sum_{n=0} (n+1/2)(x_n(0) - x_n(\zeta) - (x_n(0) - x_n(c_1))\zeta/c_1 + (w_n(0) - w_n(\zeta) - (w_n(0) - w_n(c_1))\zeta/c_1) \cdot \cdot (\sum_j r_j(c_1))/(\sum_j s_j(0))) \tag{2.13b}$$

and

$$c_2 = Dh\upsilon/k, \tag{2.13c}$$

where k is the interior conducibility and not the Boltzmann constant. The first two terms on the right-hand side of Equation 2.13a represent the linear terms which would be present even in the absence of a source. The third term accounts for the deviation from linearity of the temperature due to interaction between the walls and the vibrational degrees of freedon of the fluid. When the distributions $\{r_j(c_1)\}$ and $\{s_j(0)\}$ are zero, the expected linear steady-state distribution is obtained. In addition, it is easily shown by Equations 2.4c and 2.12, that whenever $\{r_j(\zeta)\}$ and $\{s_j(\zeta)\}$ are Boltzmann distributions, the source term vanishes, and the temperature distribution becomes spatially linear.

Figures 2.3, 2.4, and 2.5 indicate the importance of

the constant c_1. The graphs represent the temperature deviation from linearity divided by $c_2 \sum_j s_j(0)$ in the z coordinate system for $\theta = 1$, and various boundary conditions $\{x_n(0)\}$. It is necessary to divide by $c_2 \sum_j s_j(0)$ because the deviation from linearity is proportional to this process dependent quantity and elucidation of $\sum_j s_j(0)$ requires a body of theory not explored. Later developments will relate the magnitude of $\sum_j s_j(0)$ and that of the deviation of linearity. The choice $\theta = 1$ is made for convenience and plays no role in the relaxation of SI. If θ were larger, however, the energy transferred between SI molecules and HB molecules would be larger thereby causing larger deviations from linearity of the temperature when SI is a non-Boltzmann distribution. In order to study the wall effects, the graphs are plotted for the distribution $\{w_n(\underline{1})\} = 0$ only, and the effect of only one of the walls is examined. Figure 2.3 shows that when the nonequilibrium distribution at the wall contains less energy than the Boltzmann distribution at the temperature of the wall, the deviation from linearity is negative. The temperature near the wall is then less than that predicted by the Laplace equation $\nabla^2 T = 0$. Furthermore, as the ratio of the rate of HB-SI interactions to the rate of diffusion increases at constant $\underline{1}$, c_1 increases and the deviation from linearity approaches $-0.582 c_2 s_0(0)$ at $z = 0$. This asymptotic value when $x_0(0) = 1$ represents the maximum deviation from linearity for this

Figure 2.3

Negative of H(z) for $\theta = 1$, $x_0(0) = 1$, and various c_1.

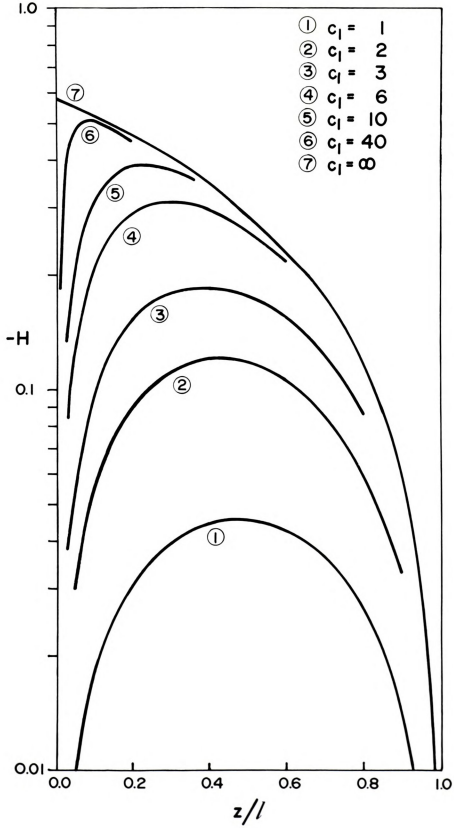
1.0
0.1
0.01
-H
0.0
0.2
0.4
0.6
0.8
1.0
z/l
① c_1 = 1
② c_1 = 2
③ c_1 = 3
④ c_1 = 6
⑤ c_1 = 10
⑥ c_1 = 40
⑦ c_1 = ∞

Figure 2.4

$H(z)$ for $\theta = 1$, $x_1(0) = 1$, and various c_1.

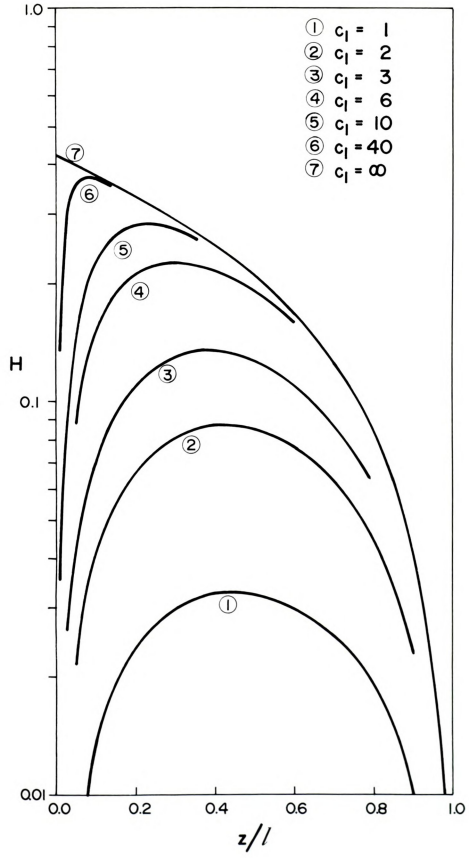
1.0
0.1
0.01
H
0.0
0.2
0.4
0.6
0.8
1.0
z/l
① c_1 = 1
② c_1 = 2
③ c_1 = 3
④ c_1 = 6
⑤ c_1 = 10
⑥ c_1 = 40
⑦ c_1 = ∞

Figure 2.4

H(z) for $\theta = 1$, $x_1(0) = 1$, and various c_1.

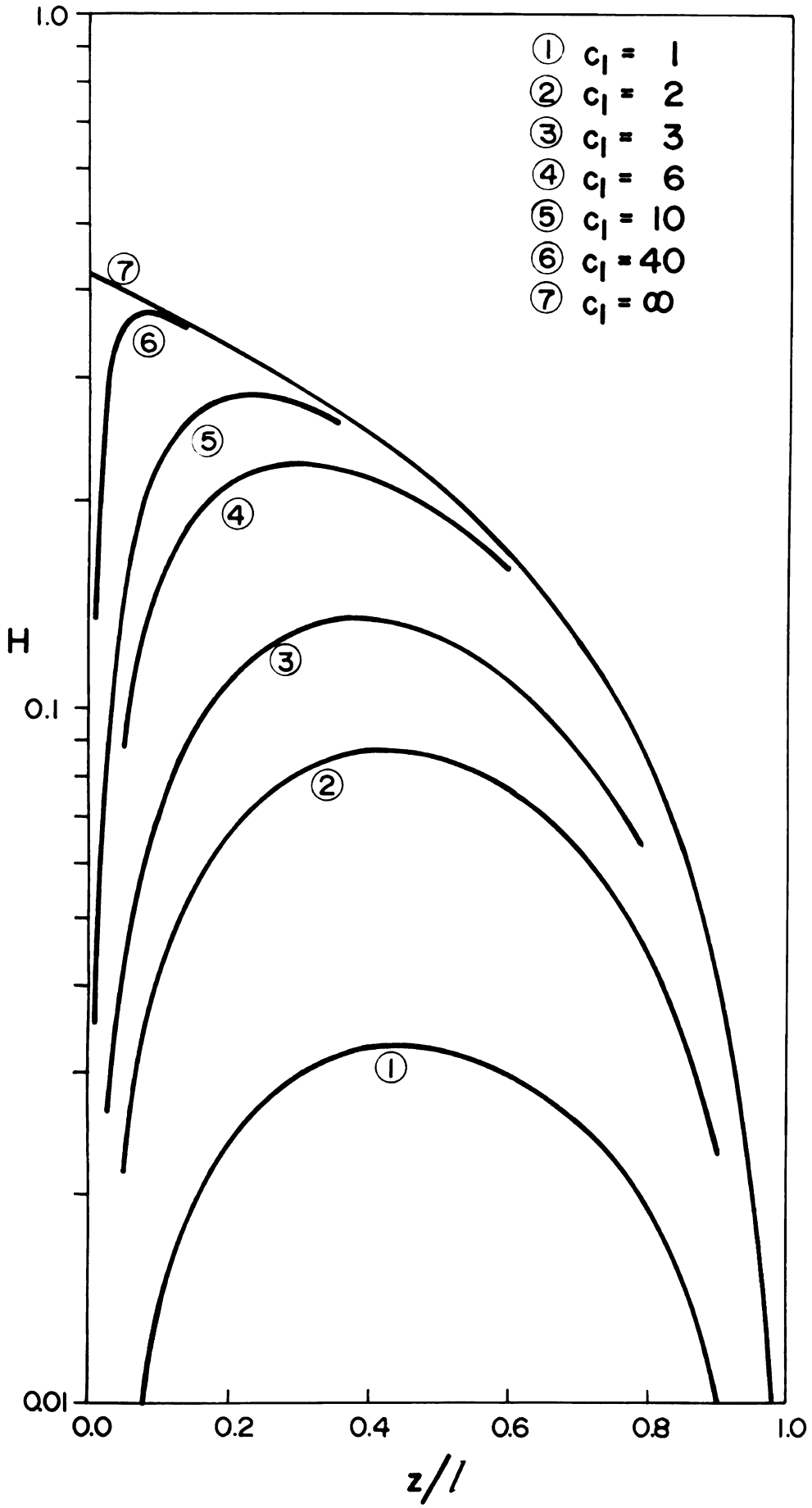
1.0
0.1
0.01
H
0.0
0.2
0.4
0.6
0.8
1.0
z/l
① c_1 = 1
② c_1 = 2
③ c_1 = 3
④ c_1 = 6
⑤ c_1 = 10
⑥ c_1 = 40
⑦ c_1 = ∞

Figure 2.5

$H(z)$ for $\theta = 1$, $x_4(0) = 1$, and various c_1.

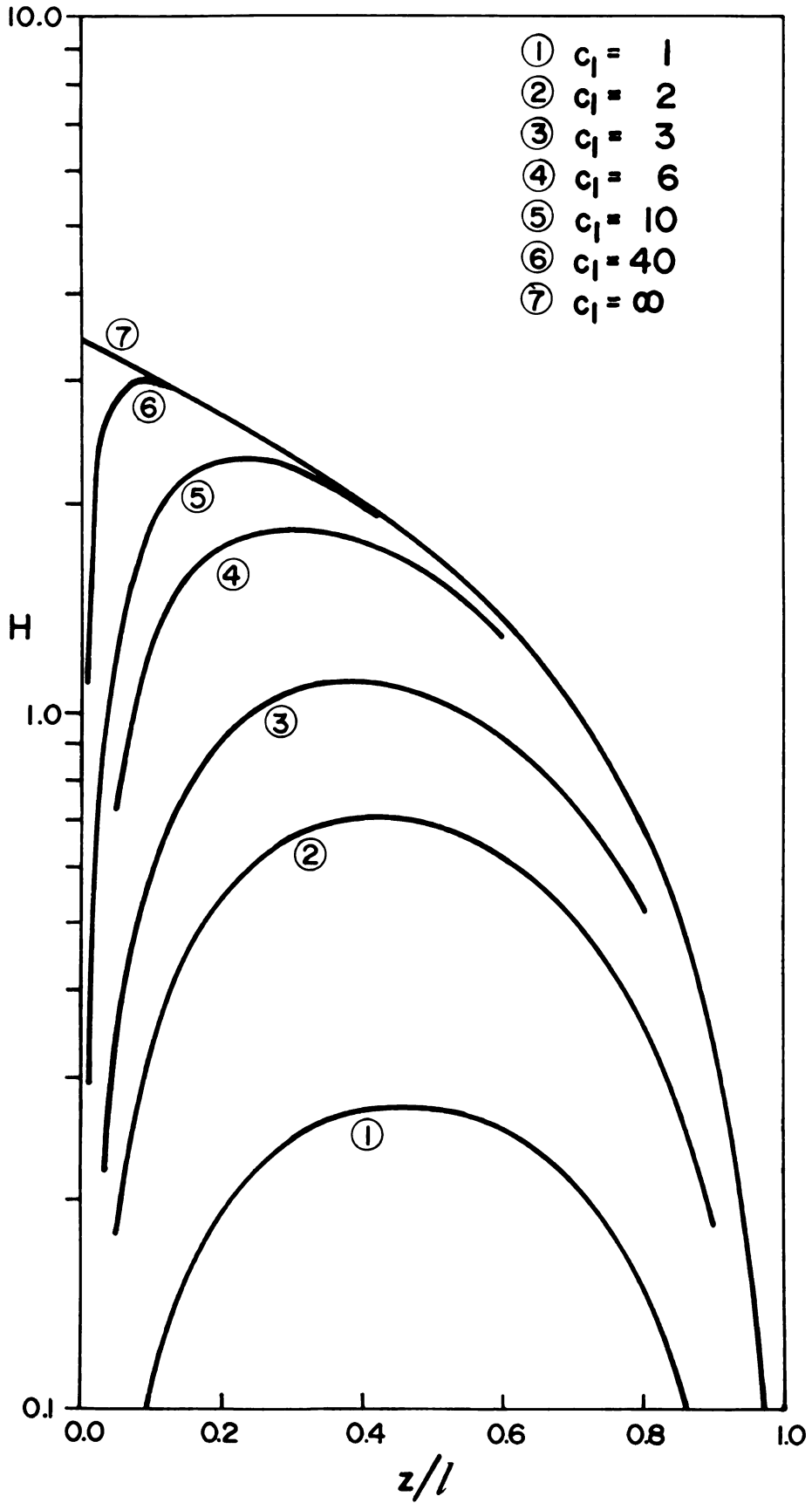
10.0
1.0
0.1
H
0.0
0.2
0.4
0.6
0.8
1.0
z/l
① c_1 = 1
② c_1 = 2
③ c_1 = 3
④ c_1 = 6
⑤ c_1 = 10
⑥ c_1 = 40
⑦ c_1 = ∞

nonequilibrium boundary distribution. The physical reasoning is that for very large values of c_1 the HB-SI interaction term is so much larger than the diffusion term that all SI molecules leaving the surface immediately absorb energy from HB and relax to a Boltzmann distribution. Thus, non-Boltzmann SI molecules do not exist further away from the surface and no further alteration of the temperature distribution can occur; the Laplace equation then describes the temperature. However, the energy absorbed by SI from HB in relaxing to a Boltzmann distribution lowers the temperature of the system. The consequence is that for very large values of c_1 the Laplace equation must be solved subject to the boundary conditions $T(\underline{1}) = T_L$ and $T(0) = T_U - 0.582c_2s_0(0)$. The boundary temperature jump thus represents the largest deviation form linearity of temperature possible.

Figures 2.4 and 2.5 both have nonequilibrium distributions at the wall which contain more energy than the Boltzmann distribution, and the graphs indicate a deviation from linearity which is a positive function of z. The temperature in these two cases is greater than that predicted by the Laplace equation. It is seen that, as c_1 increases, the limiting values of the temperature deviation are $0.418c_2s_1(0)$ and $3.418c_2s_4(0)$ for the cases $x_1(0) = 1$ and $x_4(0) = 1$, respectively. The general trend is that the greater the energy difference between $\{x_n(0)\}$ and the Boltzmann distribution at the surface, the greater is the temperature deviation from linearity divided by $c_2 \sum_j s_j(0)$.

When equilibrium distributions are associated with both walls, curves such as those in Figure 2.6 result. In this figure, the distribution $\{w_n(\underline{1})\}_{n\neq 1} = 0$, $w_1(\underline{1}) = 1$ is associated with the wall at $z = \underline{1}$. The distribution $\{x_n(0)\}_{n\neq 0} = 0$, $x_0(0) = 1$ is associated with the wall at $z = 0$. The total number of molecules in each of these boundary conditions is assumed to be identical simply for convenience. The curves result from the superposition of the curves given in Figures 2.3 and 2.4 and exhibit the same characteristics. One observes that in the central region between the plates the temperature distribution is linear, and hence Fourier's law applies. In the limit of very large values of c_1, the temperature distribution also appears to be linear. The source term for this limit is a simple delta function at the boundary which results in the appearance of a "temperature jump," or a discontinuity in temperature at the fluid-solid interface when a temperature gradient is present. This temperature jump is entirely analogous to those discussed in many other works;[20-23] see Section 1.3 for additional discussion and references.

2.3 Estimates of c_1 and c_2

The parameters c_1 and c_2 determine the spatial extent of the temperature nonlinearity from boundaries and the magnitude of the nonlinearity, respectively. The ratio

$$\underline{1}/c_1 = (D/K)^{1/2} \tag{2.14}$$

has the dimension of length and measures the spatial domain

Figure 2.6

H(z) for $\theta = 1$, $w_1(\underline{1}) = 1$, $x_0(0) = 1$, and various values of c_1.

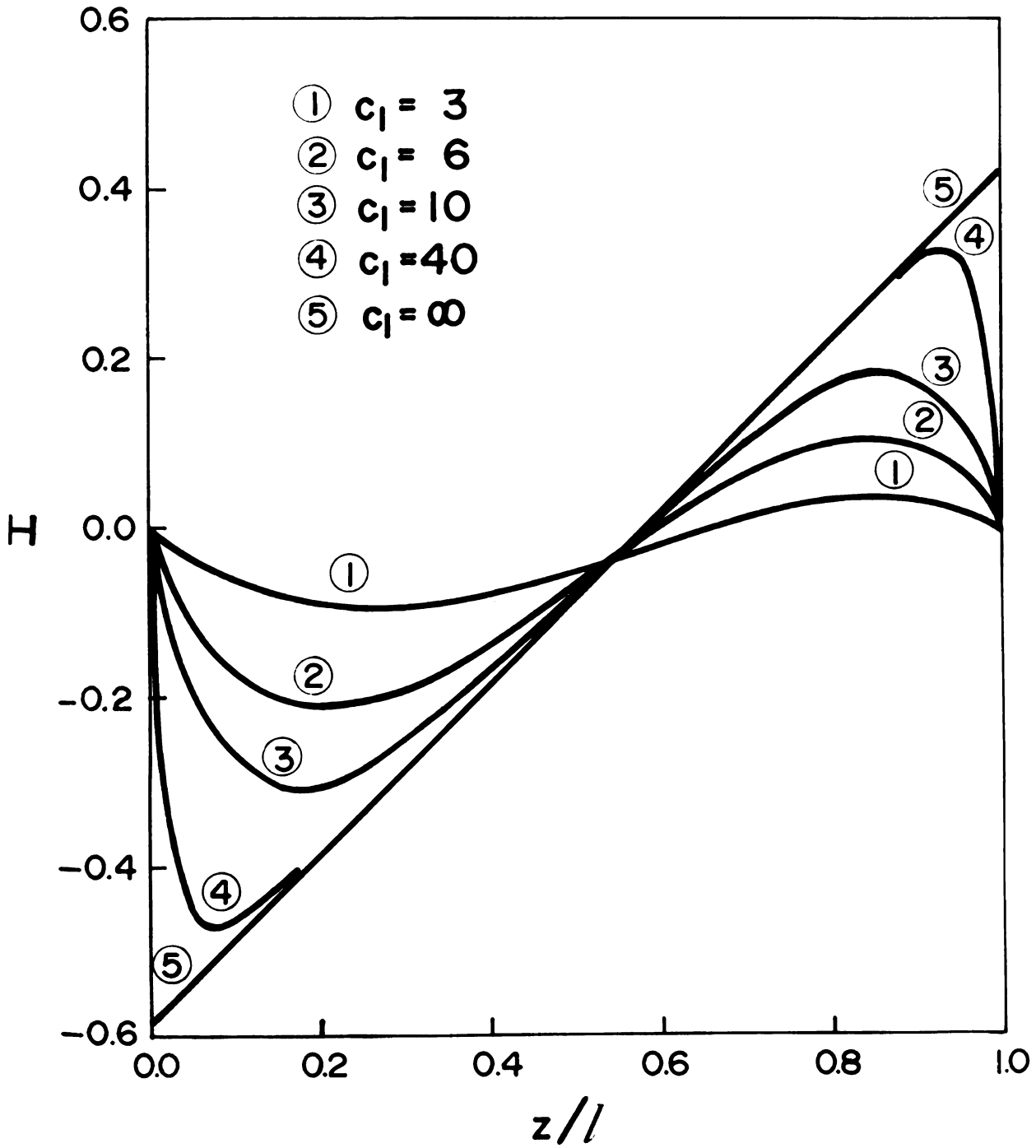
① $c_1 = 3$
② $c_1 = 6$
③ $c_1 = 10$
④ $c_1 = 40$
⑤ $c_1 = \infty$
H
z/l
0.6
0.4
0.2
0.0
-0.2
-0.4
-0.6
0.0
0.2
0.4
0.6
0.8
1.0

of the nonlinearity. Likewise,

$$\rho c_2 = \rho D h\upsilon/k \tag{2.15}$$

has the dimension of temperature and measures the magnitude of the nonlinearity; ρ is the number density of oscillators of frequency υ. By Equation 2.13 the product of ρc_2, the number fraction of SI vibrational degrees of freedom, and the function H-1 is the nonlinear magnitude. Equations 2.14 and 2.15 provide a convenient test of the diffusion mechanism's contribution to any observed nonlinear temperature distribution. The properties ( ), k, and D may be extracted from empirical tables, theoretical equations, or semiempirical equations. The rate of interaction between HB and SI, K, can be estimated by

$$K = Z_C P_{1,0} \tag{2.16}$$

where Z_C is the number of collisions per molecule per unit time and $P_{1,0}(\upsilon,T)$ is the probability per collision of the harmonic state transition $1 \rightarrow 0$. $P_{1,0}$ values for a number of gas phase systems have been determined experimentally by impact tube methods, infrared fluorescence photometry, and chemiluminescence spectrophotometry.[17,24-26] Fourier transform of infrared and Raman vibrational band contours[27,28] and picosecond spectroscopy[29-31] yield information concerning vibrational relaxation times and pathways within the liquid phase.

Table 2.1 contains estimates of $\underline{l}/c_1$ and c_2 for gas phase molecules. The computations utilize the $P_{1,0}(\upsilon,T)$ tabulations

Table 2.1

Gas phase parameters c_1 and c_2 of the molecular fundamental frequency $\tilde{\nu}$. ρ, the number density of the normal mode $\tilde{\nu}$, is the product of the degeneracy of the symmetry species and the molecular number density. T = 300 K; P = 1 atm.

Gas Molecules	$\tilde{\nu}/cm^{-1}$	Symmetry Species (36,37)	$10^3(1/c_1)/cm$	$10^{-2}\rho c_2/K$
N_2	2331		870	9.3
NO	1904		0.30	7.4
O_2	1554		610	6.1
F_2	892		2.0	3.4
Cl_2	557		0.63	2.0
CO_2	667	π_u	0.77	4.4
N_2O	589	π	0.35	3.8
COS	520	π	0.28	3.2
SO_2	518	a_1	0.077	1.6
NH_3	950	a_1	0.022	3.2
PH_3	992	a_1	0.11	3.3
BF_3	480	e	0.073	2.5
AsH_3	906	a_1	0.069	2.5
CH_4	1306	f_2	0.65	13.0
CH_3F	1049	a_1	0.29	3.5
CH_3Cl	732	a_1	0.11	2.3
CH_3Br	611	a_1	0.058	1.9
C_2H_2	612	π_g	0.11	3.5
C_2H_4	826	b_{2u}	0.10	2.3
C_2H_6	289	a_{1u}	0.013	0.77

of Stevens,[26] the ideal equation of state, the kinetic theory collision rate, and first order kinetic theory thermal conductivities and self-diffusion coefficients:[32]

$$Z_C = 4Pr_o^2(mkT/\pi)^{-1/2}, \tag{2.17}$$

$$D = 2.628 \times 10^{-3}(T^3/M)^{1/2}/(Pr_o^2\Omega^{(1,1)*}(T^*)), \tag{2.18}$$

and

$$k = 6.066 \times 10^{-5}R(T/M)^{1/2}((4C_V/9R)+1)/(r_o^2\Omega^{(2,2)*}(T^*)). \tag{2.19}$$

M is the molecular weight, $T^* = kT/\epsilon$, $\Omega^{(1,1)*}(T^*)$ and $\Omega^{(2,2)*}(T^*)$ are collision integrals tabulated by Hirschfelder et al.,[32] and $r_o(\mathring{A})$ and ϵ are the Lennard-Jones(12-6) potential parameters defined by

$$\phi(r) = 4\epsilon((r_o/r)^{12} - (r_o/r)^6). \tag{2.20}$$

The Table 2.1 computations utilize the r_o and ϵ tabulations of Stevens,[26] Ibele,[33] and Sherwood et al.[34] In Equations 2.17-2.19 D is in cm^2/sec when P is in atm; k is in cal/cm sec deg when R is in cal/mole deg. The term $(3/5)((4C_V/9R)+1)$ in Equation 2.19 is called the Eucken correction. It takes into account approximately the transfer of energy between translational and internal degrees of freedom. Heat capacities from the JANAF Thermochemical Tables[35] are used in the computation of this term.

Table 2.2 contains estimates of $\underline{1}/c_1$ and ρc_2 for liquid phase systems. The self-diffusion coefficients are

computed with Houghton's equation:[38]

$$D = (RTd/6\eta M)(M/dN)^{2/3} \qquad (2.21)$$

where d,η, and N are the mass density, viscosity, and Avogadro's number, respectively. Values of d, η, and k are extracted from standard thermophysical tables.[39,40] The collision rate within liquids is calculated with the cell model equation of Bartoli and Litovitz:[41]

$$Z_C = (8kT/\pi m)^{1/2}(2^{1/6}\rho^{-1/3} - r_o)^{-1}. \qquad (2.22)$$

This equation is valid because (a) it is consistent with the model of vibrational energy transfer via isolated binary molecular collisions, and (b) Calaway and Ewing[30,31] have demonstrated that the product of Equation 2.22 and $P_{1,0}$ values determined via gas phase experiments is comparable to vibrational relaxation times exhibited by liquid phase systems(1 psec). However, Equation 2.22 cannot be taken too seriously because it fails to deal properly with the concept of "collision" and is an inaccurate formula for the computation of collision frequencies.[42,43]

Table 2.1 reveals that the diffusional transport mechanism can produce nonlinear temperature distributions at 1 atm which extend 0.87 cm, 0.61 cm, and 0.002 cm from boundaries for gaseous N_2, O_2, and F_2, respectively. Furthermore, when SI contains 1 molecular vibrational degree of freedom out of 10^4, the nonlinear magnitude is 0.093 K, 0.061 K, and 0.034 K for gaseous N_2, O_2, and F_2, respectively.

Table 2.2

Liquid phase parameters c_1 and c_2 of the molecular fundamental frequency $\tilde{\nu}$. ρ, the number density of the normal mode $\tilde{\nu}$, is the product of the degeneracy of the symmetry species and the molecular number density. T = 300 K; P = 1 atm.

Liquid Molecules	$\tilde{\nu}/cm^{-1}$	Symmetry Species (36,37)	$10^8(1/c_1)/cm$	$\rho c_2/K$
Br_2	321		16	0.25
H_2O	1595	a_1	2.7	4.8
CS_2	397	π_u	25	3.4
CH_2Cl_2	282	a_1	5.1	0.95
$CHCl_3$	261	e	0.90	1.1
CCl_4	217	e	0.86	0.41
CH_3OH	1030	a'	0.86	6.4
C_6H_6	410	e_{2u}	2.9	2.0

For the other gases $\underline{l}/c_1 < 10^{-3}$ cm at 1 atm; therefore, the diffusional mechanism operating within these gases can only produce temperature jumps at the gas-boundary interface. The magnitude of the temperature jump is approximately 0.03 K when 1 vibrational degree of freedom in 10^4 is contained within SI. However, the extent increases as pressure decreases. From Equations 2.14 through 2.19, it is found that for gases

$$\underline{l}/c_1 \sim 1/P \qquad \text{and} \qquad \rho c_2 \sim P^0. \tag{2.23}$$

For example, a N_2O pressure decrease from 1 atm to 0.1 atm increases the nonlinearity extent from 3.5×10^{-4} cm to 3.5×10^{-3} cm; at 0.1 atm the nonlinear extent approaches measurable dimensions while the magnitude remains unchanged. Considering the typical gas parameters to be $\underline{l}/c_1 \simeq 1 \times 10^{-4}$ cm and $\rho c_2 \simeq 3 \times 10^2$ K at 1 atm, the diffusional mechanism can cause most gases to exhibit nonlinear temperature distributions which extend 0.01 cm from boundaries at 1.0×10^{-2} atm and have a magnitude of 0.03 K provided 1 vibrational degree of freedom in 10^4 belong to SI.

The diffusional energy transport mechanism can contribute only a temperature jump to observed nonlinear temperature distributions within liquids. Table 2.2 values of $\underline{l}/c_1$ lie between 10^{-8} and 10^{-7} cm, and the ratio has a very weak dependence upon pressure. The jump magnitude is typified by CS_2. It is 0.034 K when 1 molecular

vibrational degree of freedom($\tilde{\nu}$ = 397 cm^{-1}) in 10^2 belongs to SI.

2.4 Model 2

As a final example, we again consider the situation in which the fluid between the plates can be divided into two systems: the system of interest(SI) and the heat bath system(HB). In SI the vibrational degrees of freedom cannot always be described by a Boltzmann distribution while those in HB can be described by a Boltzmann distribution. In addition, it is assumed that molecules of SI are of such a density and relative position that resonant transfer of vibrational energy occurs between molecules of SI but no diffusion of molecules occurs. Model characteristics (a) and (b) are then identical to those of Model 1, and the HB-SI interaction term is given in Equation 2.4c. However, characteristic (c) for Model 2 is

(c) The propagation, or velocity-probability, of vibrational energy transfer, V, determines the SI-SI interactions according to the expression

$$(\partial \rho_n/\partial t)_{SI-SI} = V((\partial r_n/\partial z) - (\partial s_n/\partial z)), \qquad (2.24)$$

where $\{r_n\}$ is the number density distribution of SI associated with the wall at $z = \underline{1}$, and $\{s_n\}$ is the number density distribution associated with the wall at $z = 0$.

With this model, then, we have

$$(\partial \rho_n/\partial t) = (\partial r_n/\partial t) + (\partial s_n/\partial t) \qquad (2.25a)$$

where

$$(\partial r_n/\partial t) = V(\partial r_n/\partial z) + K(1-e^{-\theta})^{-1}(ne^{-\theta}r_{n-1} + (n+1)r_{n+1} - ((n+1)e^{-\theta} + n)r_n), \quad (2.25$$

$$(\partial s_n/\partial t) = -V(\partial s_n/\partial z) + K(1-e^{-\theta})^{-1}(ne^{-\theta}s_{n-1} + (n+1)s_{n+1} - ((n+1)e^{-\theta} + n)s_n). \quad (2.25$$

The signs of the gradient terms are chosen so that V is the velocity-probability in the direction away from the plate in question.

The steady-state solution of Equation 2.25 is easily obtained from Appendix I of Montroll and Shuler[4](see Appendix). With the following definitions,

$$\zeta' = c_1'z/\underline{l}, \quad c_1' = (K\underline{l}/V), \quad w_n = r_n/\sum_n r_n(c_1), \quad x_n = s_n/\sum_n s_n(0), \quad (2.26)$$

the solution of Equation 2.25, subject to the boundary conditions $\{r_n(c_1)\}$ and $\{s_n(0)\}$, and the constraint $\sum_n w_n = 1 = \sum_n x_n$, is

$$s_n(\zeta') = \sum_{k=0} a_k^{(U)} \underline{l}_n(k) e^{-k\zeta'}, \quad (2.27a$$

$$r_n(\zeta') = \sum_{k=0} a_k^{(L)} \underline{l}_n(k) e^{-k(c_1'-\zeta')}, \quad (2.27b$$

$$\underline{l}_n(v) = e^{-n\theta} \sum_{\beta=0} (1-e^{\theta}) \binom{n}{\beta}\binom{v}{\beta}, \quad (2.27c$$

$$a_k^{(U)} = e^{-k\theta}(1-e^{-\theta}) \sum_{n=0} e^{n\theta} \underline{l}_n(k) s_n(0), \quad (2.27d$$

$$a_k^{(L)} = e^{-k\theta}(1-e^{-\theta}) \sum_{n=0} e^{n\theta} \underline{l}_n(k) r_n(c_1'). \quad (2.27e$$

The first of Equation 2.12 can now be used in Equation 2.1 to determine the temperature distribution. Double integration and evaluation of the two resulting constants with the boundary conditions $T(\zeta') = T_U$ at $\zeta' = 0$ and $T(\zeta') = T_L$ at $\zeta' = c_1'$ yields, upon insertion of Equation 2.27,

$$T(\zeta') = T_U - (T_U-T_L)(\zeta'/c_1') + c_2' \sum_{n=0} (n+1/2) \sum_{k=1} k^{-1} \underline{1}_n(k)(a_k^{(U)} \cdot$$

$$\cdot (1-e^{-k\zeta'} - (\zeta'/c_1')(1-e^{-kc_1'})) \sum_{m=0} s_m(0)$$

$$+ a_k^{(L)}(1-e^{k\zeta'} - (\zeta'/c_1')(1-e^{kc_1'}))e^{-kc_1'} \sum_{m=0} r_m(c_1')), \tag{2.28a}$$

where

$$c_2' = (h\upsilon V^2/kK). \tag{2.28b}$$

The first two terms to the right of the equality are the linear terms; the third is the nonlinear term. In Equation 2.28b, k is the interior conducibility not the Boltzmann constant.

Model 2 corresponds physically to propagation of vibrational energy along large chains or local structures of molecules which might form in liquids due to the presence of walls. This mechanism would transfer energy far more rapidly than diffusion and would result in larger nonlinear temperature deviations. The mechanism is included as a speculative possibility which should be pursued experimentally.

For example, estimating the SI-SI interaction term

to be of the order of the velocity of sound in solids (10^5 cm/sec), we find

$$l/c_1' \sim 10^{-3}\text{cm} \qquad \text{and} \qquad \rho c_2' \sim 10^6 \text{ K} \tag{2.29}$$

for liquids.

2.5 Discussion

It indeed appears possible for vibrational degrees of freedom to contribute to nonlinear temperature distributions near walls. Model 1, the diffusion model, indicates that for gases with typical thermal conductivities and diffusion constants, only 1 in 10^4 molecules at the wall need be in variance with the Boltzmann distribution to achieve a temperature deviation of 10^{-2} degrees from linearity. The mere presence of walls may cause a variance of this magnitude by the reflection mechanism discussed in Section 1.3. Surface-catalyzed reactions and the absorption of reflected radiation by strongly emitting absorbing gases are also capable of producing variances of this magnitude. Weakly absorbing gases are not included in Model 1 because the effect of the wall has been treated as a boundary-value problem, which excludes direct, long-range interactions between fluid and wall via radiation. Liquids are expected to give nonlinear temperature deviations of 10^{-2} degrees when 1 in 10^2 molecules do not satisfy the Boltzmann distribution.

The strongly absorbing and emitting case of water

provides a specific application of the diffusion model. For water $\underline{l}/c_1$ is the order of a molecular spacing. Thus, the model predicts that only a temperature jump can be exhibited by the liquid. This agrees with experiment (see Section 4.3). The order of magnitude of this temperature jump is indicated by the Table 2.3 tabulation of $\rho c_2(v)H_\infty(v)$ at 300 K for various assumed delta distributions of the upper boundary SI molecules and for the v_2 bending mode, the v_L librational mode, and the hindered translational modes, v_T and v_{T_2}.[44,45] $H_\infty(v)$, which is $H(v)$ in the limit as $c_1 \to \infty$, is evaluated at $z = 0$ (*i.e.*, ignoring the SI distribution associated with the lower boundary). For example, if $x_n(v_2,0) = \delta_{n,1}$ and $s_1(v_2,0) = 0.01\rho$, then the contribution of v_2 to the temperature jump is 0.049 deg. Also, if $x_n(v_T,0) = \delta_{n,2}$ and $s_1(v_T,0) = 0.01\rho$, then the expected contribution to the temperature jump is 0.008 deg. Temperature jumps of these magnitudes are important in many experimental studies and must be considered. The weakness of models 1 and 2 is the boundary value nature of these models. This excludes the case of weakly absorbing and emitting gases and liquids which can interact with the walls via photon exchange at distances which are an appreciable fraction of $\underline{l}$.

Table 2.3

$\rho c_2(\upsilon)H_\infty(\upsilon)$ values for water at 300 K and various boundary conditions. ρ is the molecular number density, $\delta_{i,j}$ is the Kronecker delta, and table units are deg.

$x_n(0)$	$\tilde{\upsilon}_2$ 1595 cm^{-1}	$\tilde{\upsilon}_L$ 685 cm^{-1}	$\tilde{\upsilon}_T$ 193 cm^{-1}	$\tilde{\upsilon}_{T_2}$ 60 cm^{-1}
$\delta_{n,0}$	-0.0022	-0.079	-0.38	-0.55
$\delta_{n,1}$	4.9	2.0	0.21	-0.36
$\delta_{n,2}$	9.8	4.1	0.80	-0.18
$\delta_{n,3}$	15	6.2	1.4	0.0053

CHAPTER 3

BRYNGDAHL INTERFEROMETRY

3.1 Introduction

Ingelstam-Bryngdahl type wavefront shearing interferometry utilizes Savart plates to shear a plane polarized wavefront of monochromatic light after passage through a test object of non-uniform refractive index. The method was first described by Ingelstam[1,2] in 1955 and subsequently developed by Bryngdahl and coworkers.[3-8]

Section 3.2 is devoted to a survey of the application of Ingelstam-Bryngdahl interferoemtry to problems of nonequilibrium heat and mass transport phenomena in liquids. Section 3.3 introduces the particular Bryngdahl interferometer which we used to study (a) the temperature dependence of the refractive index of water; (b) temperature distributions in nonequilibrium, steady state experiments on ethyl acetate, benzene, carbon tetrachloride, and water; (c) the possibility of temperature jumps at the water-metal interface; and (d) the critical Rayleigh numbers associated with the Bénard problem.

Equations for the unrefined data, $(d^m W(Z)/dZ^m)_{m=1,2,..}$, where $W(Z)$ is the optical path associated with the vertical image coordinate Z, are also presented in Section 3.3. Unfortunately, the unrefined data are functions of the applied temperature field and the cell dimensions. Section 3.4 explores this problem and describes a program for mapping spatial derivatives of the refractive index from unrefined data. The spatial derivatives of the refractive index, $(d^m n/dz^m)_{m=1,2,..}$, are called the refined data. In the process of refining the data, the discussion is restricted to pure liquids which do not absorb the monochromatic radiation of the interferometer. From the refined data either the temperature derivatives of the refractive index or the spatial derivatives of the temperature(the temperature distribution) may be mapped. Equations which relate either $(d^m n/dT^m)_{m=1,2..}$ or $(d^m T/dz^m)_{m=1,2,..}$ to the refined data are developed in Sections 3.5 and 3.6, respectively.

3.2 Bryngdahl Interferometry: Applications

Gustafsson and coworkers[9-23] have been major pioneers in the application of wavefront shearing interferometry to problems of measurement of Soret coefficients[9,18], thermal conductivity coefficients[10,13,14], refractive indices[11,12,17,21], interdiffusion coefficients of transparent liquids[9,15,16,18,23], and interdiffusion coefficients of molten salts.[19,20,22] In 1965 Gustafsson *et al.*[9] measured the Soret coefficient for water solutions of $CdSO_4$, $AgNO_3$, and KCl by observing the time and space evolution of a Bryngdahl interferometric image of a "sandwich" type cell. The procedure involves application of a temperature gradient to an equilibrium system and analysis of the thermodiffusional demixing process; or, alternatively, removal of the temperature gradient from a nonequilibrium system and observation of the mixing process. In 1970 Wallin and Wallin[17] increased the sensitivity of the interferometer with a double exposure technique which is capable of measuring the Soret effect of water solutions a few thousandths molal in $CdSO_4$.[18] The second exposure is made after a 180° rotation of one of the Savart plates about the optical axis.

In 1967 and 1968 Gustafsson *et al*[10,13,14] used a plane source of heat in a transient method to measure the thermal conductivity of water, KNO_3, $LiNO_3$,

$NaNO_3$, $RbNO_3$, and $CsNO_3$. The Bryngdahl interferometer was used to display the time dependent temperature distribution close to the plane heat source. The average deviation of the measured thermal conductivity of water from the recommended values of McLaughlin[24] was 0.37%.

An isothermal method of measuring absolute refractive indices has been developed by Gustafsson's research group.[11,12,17,21] The method has been used to measure the temperature dependence of the refractive index of water[21] with an accuracy of about $\pm 1 \times 10^{-6}$, and that of the molten alkali nitrates[12] with an accuracy of about $\pm 3 \times 10^{-5}$. The wavefront shearing interferometer of this method combines two light beams, one passing through the liquid and the other through a rotatable quartz plate inside the liquid. The refractive index of the quartz plate serves as a reference. The rotatable reference plate technique is well known, and the equations which describe the optical path differences as a function of rotation angle were developed by Adams[25] in 1915.

Finally, Gustafsson's research group has developed an isothermal, bottom layer technique for the measurement of interdiffusion coefficients of transparent liquids. A crystal of the diffusing substance is dropped to the bottom of the liquid container in initiation of a bottom layer. Bryngdahl interferometry is used to observe the transient diffusion process. The procedure requires that the density of the crystal be much greater than that of the

liquid. In this way the amount of material being dissolved during the "drop" is negligible. The diffusion of KCl and $CdSO_4$ in pure water[15,16,23] at 22°C and the diffusion of silver ions[15] into the alkali nitrates $NaNO_3$, KNO_3, and $RbNO_3$ from 310°C to 380°C has been studied with the "drop", plane source technique. The plane source diffusion technique has also been used to measure the diffusion coefficients of F^- and Br^- in $LiNO_3$; F^-, Br^-, I^-, CO_3^{-2}, and SO_4^{-2} in $NaNO_3$; and I^- and CO_3^{-2} in $RbNO_3$.[20] The temperature range of melting point to 100°C above the melting point was studied. The interdiffusion coefficient of thallous ion(Tl^+) in $LiNO_3$ has been determined in the temperature range of 260°C to 355°C; Van der Waals interactions are shown to contribute significantly to the diffusion rate.[22]

Thomas and coworkers have used Bryngdahl interferometry to measure the diffusion coefficients of mono-, di-, and tri-ethanolamines in aqueous solutions at infinite dilution[26,27] and have made a comparison with existing semi-empirical equations. The results demonstrate the inadequacy of these equations and suggest that hydration of the ethanolamines plays an important role in the diffusion process. Thomas et al. have also used a special interferometric method with increased vertical shear in conjunction with

a pressure transducer to study absorption[28,29] and desorption[30] of gas at the gas-liquid interface. The absorption experimental systems include CO_2-water, C_2H_2-water, NH_3-water, SO_2-water, and CO_2-propylene carbonate. The desorption experimental systems include carbon dioxide-water acetylene-water, ammonia-water, sulphur dioxide-water, and acetone-water. Anomalously large transport of solute is explained in terms of convective disturbances, eddies, and microflows at the interface. The cellular structure of the disturbances is smaller than that which is directly observable by interferometric technique. Onset times of the disturbances were reported. Temperature effects at the interface which could produce such disturbances and could even be responsible for the observed fringe shift were reportedly eliminated by the proper choice of systems for examination,[30] and by using dilute solutions. The studies are then limited to buoyancy and surface tension effects.

Pepela *et al.*[31] have developed an isothermal diffusiometer which features Bryngdahl-Ingelstam interferometry. They have determined the diffusion coefficients at 25°C of aqueous solutions of sucrose, n-butyl alcohol, magnesium sulfate, tetra-n-propylammonium bromide, tetra-n-butylammonium bromide, thiourea, glycine anhydride, ϵ-caprolactam, and mannitol. The results for $MgSO_4$-water, n-Pr_4NBr-water, and thiourea-water are compared to Gouy interferometric and

conductance methods. Data obtained from the three methods are in excellent agreement. The authors believe that the diffusion coefficients may be measured with their technique to a precision of ±0.3%. Staker and Dunlop[32] have also used this isothermal technique to measure the diffusion coefficients at 25°C of the benzene-carbon tetrachloride binary liquid over the whole concentration range. The results agree with those of Gouy interferometry to within 1%.

Anderson and Horne[33] have used a nonisothermal, wavefront shearing method very similar to the demixing-mixing experiments of Gustafsson[9] to determine concentration and temperature dependence of the thermal diffusion factor and diffusion coefficient for the CCl_4-C_6H_{12} system between 20°C and 35°C. The standard error of the thermal diffusion factor is about 1% and that of the diffusion coefficient about 3%. This interferometer was also used by Olson and Horne[34] to measure the temperature dependence of the refractive indices of water, carbon tetrachloride, cyclohexane, and benzene at 25°C with a nonisothermal technique. They report unexpected parabolic steady state fringe patterns which are attributed to nonlinear temperature distributions associated with metal boundaries.

Mitchell and Tyrrell[35] use a Bryngdahl interferometer to measure the diffusion coefficients of dilute solutions of benzene, phenol, and resorcinol in propane-1,2-diol. The application of a temperature gradient creates a gradient of solute. The observation of the transient decay of the concentration gradient upon removal of the temperature gradient allows

the calculation of diffusion coefficients. Results show the importance of solute-solvent interactions in diffusion. The authors claim that diffusion coefficients as low as 5×10^{-8} $cm^2 sec^{-1}$ can be measured. In a later paper Skipp and Tyrrell[36] report interdiffusion coefficients for carbon tetrachloride, carbon tetrabromide, methyl pivalate, chlorobenzene, and phenol in propane-1,2-diol. The results show that spherical molecules(CCl_4, CBr_4, methyl pivalate) diffuse at a rate comparable to the prediction of the Stokes-Einstein relationship $D = kT/4\pi\eta r$, where the molecular radius(r) is calculated from molar volume data, and η is the viscosity. However, planar molecules diffuse about twice as fast as expected. The evidence suggests that free rotation of planar solutes during diffusion is prevented in propane-1,2-diol. In more mobile solvents free rotation is possible.

The final major research group included in this survey is that of Porsch and Kubin.[37-42] They have used Bryngdahl interferometry and isothermal, flowing-boundary cells to measure the diffusion coefficients of biphenyl-benzene,[37,39,41] sucrose-water,[39,41] and monodisperse polystyrene-toluene[39,41] at 25°C. Further, they have determined up to four average diffusion coefficients[38,40] for the polydisperse polyisobutylene-heptane system, and unfractionated polystyrenes in toluene. The average diffusion coefficients are related to the moments of the diffusion coefficient. Porsch

and Kubin have also measured the concentration dependence of the first four average diffusion coefficients of a polystyrene-toluene system[42] having a broad molecular weight distribution.

Bryngdahl wavefront shearing interferometry is one of a number of interferometric methods which have been used successfully to study heat and mass transport. Other methods include Gouy interferometry, Rayleigh interferometry, wedge-interference interferometry, Jamin, Mach-Zehnder, and Michelson interferometry, and multiple-beam interferometry. Useful reviews of these methods and their applications are available.[43-51]

3.3 Bryngdahl Interferometry: Apparatus, Cell, Data

The Bryngdahl interferometer, cell-water jacket assembly, and temperature measurement technique used in this work were developed by Anderson[52] and Olson.[53] The interferometer features a Spectra Physics Stabilite 120 helium-neon laser with 5.0 mw output power at 632.8 nm and a Spectra Physics 336 multiwavelength collimating lens of collimation within 1/8 wavelength over a 4.6 cm aperture. The laser is oriented so that the cell is illuminated with radiation polarized in the direction which bisects the x,z axes shown in Figure 3.1. After passage through a cell of height l and length a, the L1-L2 lens combination reduces the cell image to a size compatable with the modified Savart plates Q1 and Q2.

Figure 3.1

(A) The interferometer.

1. collimator
2. cell-water jacket assembly
3. lens, L1
4. lens, L2
5. modified Savart beam splitter, Q1
6. lens, L3
7. modified Savart beam splitter, Q2
8. analyser, A
9. lens (optional)
10. camera

(B) The cell-water jacket assembly.

1. lower assembly
2. upper assembly
3. cell

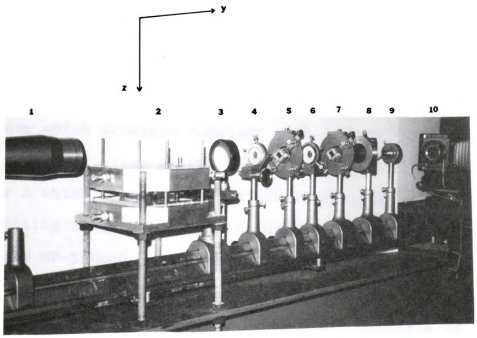

A

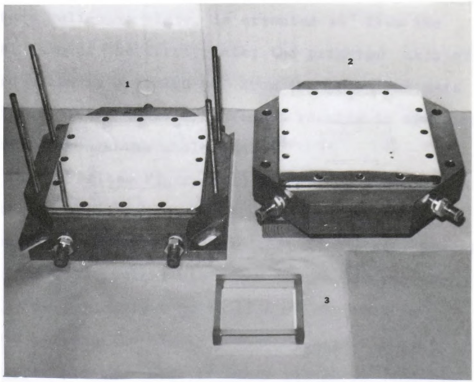

B

The first beam splitter, Q1, splits the wavefront into two identical, vertically sheared wavefronts. Before entering Q2 the double image passes through the converging lens L3. This introduces a small shear angle between the wavefronts which produces constant path length differences. After Q2 the radiation passes through a polarization analyser A which is crossed with the laser polarization. The resulting image is sharply focused and recorded with a Polaroid MP-3 Land Camera using Polaroid Type 42 black and white film. The modified Savart plates were manurfactured by Valpey Co., Halliston, Mass. Each plate consists of three 2 cm x 2 cm x 0.7 cm quartz subplates bonded without cement, flat to 1/20 wavelength, and parallel to 2 seconds of arc. The principal plane of the second subplate, which serves as a half-wave plate, is oriented 45^{o} from the principal axis of the first plate; the principal axis of the third plate is oriented 90^{o} from the principal axis of the first plate. This arrangement results in symmetrical light paths through the whole plate.[8]

The cell (see Figure 3.1) is made of four pieces of $\frac{1}{4}$ inch thick glass cemented together with Chemgrip epoxy adhesive (Chemical Rubber Co., Cleveland, Ohio). 7 cm is a typical width and length (a), and the height (l) is typically 4 mm to 15 mm. The cell is sandwiched between two highly polished, silver plated, $\frac{1}{4}$ inch copper plates. Each of these plates is secured to a magnesium water jacket which serves to control the

temperature of the plate. The volume of a water jacket is 230 ml. In the isothermal configuration water is fed to both water jackets from a single 10 liter Neslab water bath (Neslab Instruments, Durham, N.H.). In the nonisothermal configuration each water jacket is fed separately from 45 liter Neslab water baths. The temperature of each bath is controlled to ±0.003 deg with Versa-Therm proportional electronic temperature controllers (Cole-Palmer Instrument Co.) balanced against coils containing cold water feed from a 25 gallon Lab-Line heat bath (Lab-Line Instruments Inc., Melrose Park, Ill.) maintained at about 14°C. Water is pumped from the heat baths to the water jackets at a flow rate of 2.8 l/min.

Temperature measurement is made with 40 gauge copper-constantan thermocouples soldered to matched 20 gauge copper-constantan leads. The 20 gauge leads are placed in mercury containing tubes and inserted well within an air saturated ice-water slush in accordance with standard procedure.[54,55] Copper leads connect the mercury tubes with the potentiometer. Thermocouple electromotive force is measured with a Leeds and Northrup K-3 Universal Potentiometer. The Eppley unsaturated cadmium sulfate standard cell used in the potentiometer was calibrated in terms of the U.S. legal volt effective January 1, 1969, by Leeds and Northrup Co. prior to experimentation. Uncertainty in null detection is ±0.1 μv, which corresponds to ± 0.003 deg. Thermocouple electromotive

force is standardized in the 1968 International Practical Temperature Scale (IPTS-68)[54,56] with the secondary reference points: the ice point, the sodium decahydrate sulfate-monohydrate sulfate solution point, the pressure corrected[56] boiling point of water. The resulting calibration is

$$T = 2.5577\ 10^{-2}E - 5.2922\ 10^{-7}E^2 \qquad (3.1)$$

where E is electromotive force measured in μv, and T is temperature in ^{o}C. This calibration is in good agreement with National Bureau of Standard recommended (March,1974) reference tables based on the IPTS-68.[57] To determine the temperature of a silver plate, the temperatures of two thermocouples (one on each side of the cell, out of the optical path, and in intimate contact with the silver) are averaged.

In the technique practiced by Anderson[52] and Olson[53], the cell was greased, top and bottom, with silicone or fluorosilicone lubricant and loosely clamped between the silver plates. The cell was then filled through a filling tube which is part of the upper plate and was subsequently pushed away from the filling hole. This procedure results in a fluid tight seal but has the disadvantage that excess grease prevents the interferometric examination of the fluid near the top and bottom walls. We eliminated this difficulty by hand grinding the sealing surfaces of the glass cell to 0.001 inch flatness with progressively finer grades of the silicon carbide Crystolon

(Norton Abrasives, Worcester, Mass.). The cell is firmly clamped between the silver plates with four securing nuts. An interferometric check is made to insure that the glass cell is not distorted. Evaporation of liquids such as carbon tetrachloride and ethyl acetate through the silver-glass interface is apparent one day after filling. This is a very long time relative to the duration of the pure fluid experiments of this work. Additionlly, to improve the optical quality of the cell, the optical faces are ground with ferric oxide powder. Figure 3.2 demonstates the quality of the polished cell by comparing the best quality image obtainable with the interferometer, the image of a slit, with the image of the assembled polished cell-silver plate-water jacket assembly in the isothermal configuration. The comparison shows that the shear parameter, 2D, is blurred in the cell image and fringes are not as sharp. Blurring of the shear parameter is due to roughness of the cell edge. Degradation of the fringe shape is caused by optical face, surface, roughness. The quality of the cell image is satisfactory, however, and the cell height parameter, H, the shear parameter, 2D, and the distance between fringes δ can be measured within 1% accuracy.

The experimental procedure is:

1. Establish the isothermal configuration by determining the temperature difference

$$\Delta T_o = T_U - T_L$$

to be applied between the top and bottom silver plates.

Figure 3.2

(A) Best quality image obtainable with interferometer, the slit image. (B) Isothermal cell-water jacket assembly image. Z is the vertical image coordinate measured from the upper, bounding, plate. 2D is the shear parameter. H is the image cell height. δ is the distance between fringes in the isothermal cell configuration.

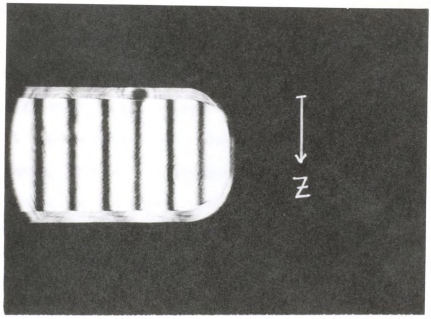

A

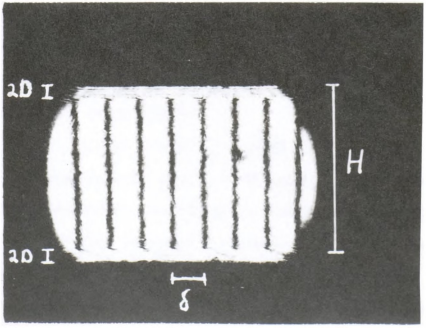

B

Adjust both plates to the mean temperature; i.e. $T_L + \Delta T_o/2$. T_L is the temperature of the lower plate in the nonisothermal configuration; T_U is the temperature of the upper plate.

2. Fill cell with liquid, wait for temperature equilibration, focus front face of cell onto camera.

3. Take photograph of isothermal cell image for evaluation of 2D, H, and δ (see Figure 3.2).

4. Apply ΔT_o and record number of fringes which evolve at image center in establishment of steady state.

5. Focus front face of cell. Take photogragh of steady state image.

For further details of the temperature switching device, see Anderson;[52] for details of the photomultiplier arrangement used in fringe counting, see Olson.[53] The nonisothermal image photograph is used to determine the exact number of fringes, N(Z), which evolve in the establishment of the steady state.

According to Bryngdahl[8] and Olson,[34,53] the image fringe pattern is described by

$$W(Z+D) - W(Z-D) = \pm\lambda N(Z) \qquad (3.2)$$

where W(Z) is the optical path of the light pencil associated with the vertical image coordinate Z which is optically conjugate to the cell vertical coordinate z; 2D is the shear parameter (see figure 3.2); λ is the wavelength of the interferometric light source (632.8 nm) and N(Z) is the number of fringes which have evolved at Z. The sign of Equation 3.2 is altered if Q2 is rotated 180^o or if

the sign of ΔT_o is altered. To write Equation 3.2 in a more useful form, expand $W(Z \pm D)$ in a Taylor series about Z. The even terms vanish leaving

$$\pm N(Z) = (2/\lambda) \sum_{n=1,3,5..} (D^n/n!)(d^n W(Z)/dZ^n). \qquad (3.3)$$

Furthermore, let X(Z) be the horizontal image coordinate of a particular fringe. Then

$$X(Z) = \delta N(Z) + \text{arbitrary constant.} \qquad (3.4)$$

Differentiation of Equation 3.3 m times with respect to Z yields the matrix equation

$$\pm \begin{bmatrix} N\delta \\ dX/dZ \\ d^2X/dZ^2 \\ d^3X/dZ^3 \\ d^4X/dZ^4 \\ \cdot \\ \cdot \\ \cdot \end{bmatrix} = (2\delta/\lambda) \begin{bmatrix} D & 0 & D^3/3! & 0 & D^5/5! & .... \\ 0 & D & 0 & D^3/3! & 0 & .... \\ 0 & 0 & D & 0 & D^3/3! & .... \\ 0 & 0 & 0 & D & 0 & .... \\ 0 & 0 & 0 & 0 & D & .... \\ \cdot & \cdot & \cdot & \cdot & \cdot & \\ \cdot & \cdot & \cdot & \cdot & \cdot & \\ \cdot & \cdot & \cdot & \cdot & \cdot & \end{bmatrix} \begin{bmatrix} dW/dZ \\ d^2W/dZ^2 \\ d^3W/dZ^3 \\ d^4W/dZ^4 \\ d^5W/dZ^5 \\ \cdot \\ \cdot \\ \cdot \end{bmatrix} . \qquad (3.5)$$

The parameters δ and D are known from the isothermal cell photographs. N(Z) and $(d^mX/dZ^m)_{m=1,2..}$ are measurable from the nonisothermal image photographs. Thus, the inverse of Equation 3.5 serves to determine the derivatives of the optical path with respect to the vertical coordinate; i.e. $(d^mW/dZ^m)_{m=1,2..}$. These derivatives are called the "unrefined data" for reasons which will become apparent in the next section. Assuming that the higher order fringe derivatives, $(d^mX/dZ^m)_{m=5,6..}$, are equal to zero and that the

D matrix is non-singular, inversion of Equation 3.5 yields

$$\pm\begin{bmatrix} \bar{d}W/dZ \\ d^2W/dZ^2 \\ d^3W/dZ^3 \\ d^4W/dZ^4 \\ d^5W/dZ^5 \end{bmatrix} = (\lambda/2D\delta)\begin{bmatrix} 1 & 0 & -D^2/6 & 0 & 7D^4/360 \\ 0 & 1 & 0 & -D^2/6 & 0 \\ 0 & 0 & 1 & 0 & -D^2/6 \\ 0 & 0 & 0 & 1 & 0 \\ 0 & 0 & 0 & 0 & 1 \end{bmatrix}\begin{bmatrix} \bar{N}\delta \\ dX/dZ \\ d^2X/dZ^2 \\ d^3X/dZ^3 \\ d^4X/dZ^4 \end{bmatrix}. \quad (3.6)$$

All quantities on the right hand side of the equality are experimentally determined. Equation 3.6 is the working equation for the determination of the unrefined data.

3.4 Refined Data; Refraction of Light

Defining the optical path to be the path experienced by a radiation pencil traversing the cell, spatial derivatives of the optical path are not properties of the liquid. The optical path depends upon the length of the cell, a, and the magnitude of the applied temperature gradient. Relative to the isothermal liquid state, a temperature gradient causes an increase in the optical path experienced by the interferometer photon beam transversing the liquid. The beam curves toward the cooler temperatures due to the drag effect of greater density. This is illustrated in Figure 3.3. In radial temperature fields this effect is termed "thermal blooming."[66] To remove experimental configurational aspects of the unrefined data, it is necessary (a) to determine the light path, z(y) in Figure 3.3, of a photon beam of infinitesimal cross section which enters the liquid at z_o; (b) to determine the dependence of the unrefined data upon cell length, and upon spatial derivatives of the refractive index; and (c) to

Figure 3.3

Refraction of light in a one dimensional gradient. $z(y)$ is the path of a photon pencil of infinitesimal cross section which enters the liquid cell at $z = z_o$. z_f is the exit coordinate. $T_U > T_L$.

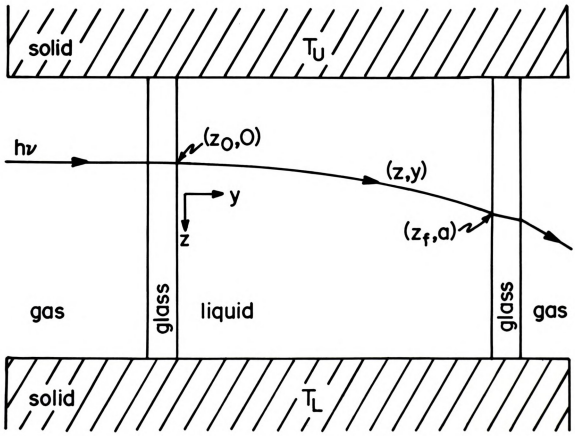
solid
T_U
$h\nu$
$(z_0,0)$
(z,y)
y
z
(z_f,a)
gas
glass
liquid
glass
gas
solid
T_L

determine eventually either the temperature dependence of the refractive index or the spatial derivatives of the temperature. The spatial derivatives of the refractive index are called the "refined data."

Many of the equations derived below have been studied and published with slight modification.[50,58-62] We discuss these equations in detail here for the purpose of establishing an iterative method for the numerical mapping of refined data from unrefined. The analysis is restricted to one component fluids in one dimensional refractive index fields, but it could be extended to multicomponent systems if the variation of the optical path with mole fraction were included. The possiblity of absorption of interferometric light by the liquid is totally neglected. This neglect is justified for the one component, weakly absorbing liquids examined in this work because there is no experimental observation of significant thermal blooming in these liquids.[63,64] However, in cases for which the liquid is moderately or strongly absorbing, the temperature field within the liquid is altered. This results in significant thermal blooming[65-67] and necessitates the inclusion of absorption effects.

Abnormally large thermal diffusion coefficients may render thermal blooming very important in binary mixtures near the consolute critical point.[64,68,69] This is a Soret effect (diffusion in a temperature gradient) response to the temperature gradient associated with absorbed interferometric

radiation. Concentration differences across the beam of a few parts in 10^7 give appreciable thermal blooming at very low powers of the illumination radiation.[64]

Consider a beam of light of infinitesimal cross section and frequency υ which enters the liquid at the coordinate $(z_o,0)$ indicated in Figure 3.3. The path, s, traveled by this beam through the liquid is classically determined by Fermat's variational principle[70] for the optical path;

$$\delta W(z_o) = \delta\int n(z)ds = 0 \qquad (3.7)$$

where $W(z_o)$ is the optical path of the photon pencil entering the liquid at z_o, and $n(z)$ is the refractive index. In a one dimensional refractive index field, the path differential is

$$ds = ((dy/dz)^2 + 1)^{1/2}dz. \qquad (3.8)$$

Substitution into Equation 3.7 yields

$$\delta\int n(z)((dy/dz)^2 + 1)^{1/2}dz = 0. \qquad (3.9)$$

It is well known[71] that this variation statement implies that the integrand satisfies Euler's equation,

$$(d/dz)(\partial/\partial(dy/dz))(n(1 + (dy/dz)^2)^{1/2}) - (\partial/\partial y)(n(1 + (dy/dz)^2)^{1/2}) = 0. \qquad (3.10)$$

The second term is zero,and the first is equivalent to

$$(d/dz)(n(dy/dz)(1 + (dy/dz)^2)^{-1/2}) = 0. \qquad (3.11)$$

Integration, evaluation of the integration constant at $z = z_o$, and use of the experimental criterion $dz(0)/dy = 0$ yields

$$((n(z)/n(z_o))^2 - 1)(dy/dz)^2 = 1; \qquad (3.12)$$

or,

$$dy = \pm dz/((n(z)/n(z_o))^2 - 1)^{1/2}. \qquad (3.13)$$

Because y and z must not be imaginary,

$$n(z)/n(z_o) > 1, \qquad (3.14)$$

and the light beam must curve toward the higher refractive indices; that is, toward the lower temperatures. Thus, if the temperature decreases with increasing z in a particular experimental configuration, then the positive sign is used in Equation 3.13. If temperature increases with increasing z, then the negative sign must be retained.

We now restrict the discussion to the case of heating from above with the z coordinate originating from the upper wall. The resulting equations apply to the case of heating from below but with the coordinate system originating from the lower wall. To facilitate the integration of Equation 3.13, expand $n(z)/n(z_o)$ in a Taylor series about $z = z_o$. Then,

$$n(z)/n(z_o) = \sum_{m=0} N^m (\Delta z)^m \qquad (3.15a)$$

where

$$N^m = (1/m!\, n(z_o))(d^m n(z_o)/dz_o{}^m) \qquad (3.15b)$$

and

$$\Delta z = z - z_o. \qquad (3.15c)$$

Furthermore,

$$(n(z)/n(z_o))^2 = \sum_{v=0} M_v (\Delta z)^v \qquad (3.16a)$$

where

$$M_v = \sum_{m=0}^{v} N^m N^{v-m}. \qquad (3.16b)$$

With Equations 3.15c, 3.16a, and the requirement $y(z_o)=0$,

integration of Equation 3.13 yields

$$y = \int_0^{\Delta z} \left(\sum_{v=1} M_v w^v \right)^{-1/2} dw. \qquad (3.17)$$

Table 3.1 shows that for water in a temperature gradient of 10 deg/cm, $(M_v)_{v=3,4,..}$ are of negligible magnitude relative to M_2. They can, therefore, be neglected. The refractive indices of most liquids have first order temperature variations which are less dependent upon temperature than those of water; for them, $(M_v)_{v=3,4..}$ are less important. Since $\Delta z < 1$cm, the third order term of Equation 3.17 is less than 0.1% of the second order term, and can safely by discarded. Equation 3.17 becomes

$$y = \int_0^{\Delta z} (M_1 w + M_2 w^2)^{-1/2} dw \qquad (3.18a)$$

$$= (-M_2)^{-1/2} \cos^{-1}(2M_2 M_1^{-1} \Delta z + 1). \qquad (3.18b)$$

Inversion yields the desired equation,

$$\Delta z = M_1 (2M_2)^{-1} (\cos((-M_2)^{1/2} y) - 1). \qquad (3.19)$$

This describes z(y) for a photon beam which enters the liquid at z_o normal to the cell face.

It is now possible to write the optical path as a function of the spatial derivatives of the refractive index and the length of the cell, a. Using the path integral expression for the optical path (Equation 3.7), Equations 3.8, 3.12, and 3.16a, we find

$$W(z_o) = n(z_o) \sum_{v=0} M_v \int_0^a (\Delta z)^v dy. \qquad (3.20)$$

Table 3.1

Derivative estimates of M_v (Equation 3.16b) for water in a 10 deg/cm temperature gradient.

v	M_v	dM_v/dz	d^2M_v/dz^2
1	$10^{-3}cm^{-1}$	$-3x10^{-4}cm^{-2}$	$6x10^{-7}cm^{-3}$
2	$-10^{-4}cm^{-2}$	$-10^{-7}cm^{-3}$	———
3	$-10^{-7}cm^{-3}$	———	———
4	$10^{-8}cm^{-4}$	———	———

The indicated integration requires the use of Equation 3.19. The integrated form is

$$W(z_o)/n(z_o) = (1 + M_1^2/(8(-M_2)))a - (M_1^2/(16(-M_2)^{3/2}))\sin(2(-M_2)^{1/2}a). \quad (3.21)$$

Expansion in powers of a, yields

$$W(z_o)/n(z_o) = a + (M_1^2/12)a^3 - (M_1^2(-M_2)/60)a^5 + (M_1^2(-M_2)^2/630)a^7 - (M_1^2(-M_2)^3/11340)a^9 + \ldots . \quad (3.22)$$

The refined data, $(d^m n(z_o)/dz_o^m)_{m=1,2..}$, are now mapped from $(d^m W(z_o)/dz_o^m)_{m=1,2,..}$ by taking m derivatives with respect to z_o. The result is

$$a(d^m n(z_o)/dz_o^m) = d^m W(z_o)/dz_o^m - \sum_{i=0} B_i^m a^{2i+3} \quad (3.23a)$$

where

$$\begin{aligned} B_0^m &= (1/12)(d^m(nM_1^2)/dz_o^m) \\ B_1^m &= (1/60)(d^m(nM_1^2M_2)/dz_o^m) \\ B_2^m &= (1/630)(d^m(nM_1^2M_2^2)/dz_o^m) \\ B_3^m &= (1/11340)(d^m(nM_1^2M_2^3)/dz_o^m). \end{aligned} \quad (3.23b)$$

Additional equations are needed to associate the unrefined data with $(d^m W(z_o)/dz_o^m)_{m=1,2..}$. To find these equations, let (a) $Z(z_o)$ be the image coordinate associated with the cell face coordinate z_o, (b) y_I be the plane of focus within the cell, (c) $z_I(z_o)$ be the image plane

z coordinate of the photon pencil associated with z_o, and (d) note that $H/\underline{l}$ is the magnification factor of the interferometer. Then,

$$\underline{l}Z(z_o)/H = z_I(z_o) - z_I(0) \tag{3.24}$$

where $z_I(0) = 0$ when the front face of the cell is focused. Use of Equation 3.19 in Equation 3.24 yields

$$\underline{l}Z(z_o)/H = z_o + (M_1(z_o)/(2M_2(z_o)))(\cos((-M_2(z_o))^{1/2}y_I) - 1) - (M_1(0)/(2M_2(0)))(\cos((-M_2(0))^{1/2}y_I) - 1). \tag{3.25}$$

Taking m derivatives with respect to z_o, we find

$$(\underline{l}/H)(d^mZ(z_o)/dz^m) = \delta_{m,1} + (y_I^2/4)(d^mM_1(z_o)/dz_o^m) + \cdots \tag{3.26}$$

where m = 1,2.. Equation 3.25 is used to determine the conjugate image coordinate, Z, of a particular cell face coordinate, z_o; and Equation 3.26 is used to determine derivatives of the optical path with respect to cell face coordinate z_o.

The difficulty with using Equations 3.25, 3.26, and 3.23a is that the refined data, $(d^mn(z_o)/dz_o^m)_{m=1,2..}$, appears to the right of all equalities. A simple iteration procedure is possible, however. The $\underline{i}$th order iteration proceeds as follows:

1. Assume an $\underline{i}$th order approximation to the set $(d^mn(z_o)/dz_o^m)_{m=1,2..}$ and calculate $M_1(z_o)$ and $M_2(z_o)$ in the $\underline{i}$th order with Equation 3.16b. Use these in the right hand side of Equation 3.25 to determine $Z(z_o)$ in the $\underline{i}$th order. The unrefined data, $(d^mW/dZ^m)_{m=1,2..}$, are now

associated with z_o. A convenient 0th order approximation to M_1 is zero; i.e., $(M_1)_{0\text{th order}} = 0$.

2. Use the ith order approximation to $M_1(z_o)$ in the right hand side of Equation 3.26 to calculate $(d^m Z(z_o)/dz_o^m)_{m=1,2..}$.

3. Calculate $(d^m W(z_o)/dz_o^m)_{m=1,2..}$ with the chain rule equations

$$dW(z_o)/dz_o = (dZ/dz_o)(dW(Z)/dZ)$$

$$d^2W(z_o)/dz_o^2 = (d^2Z/dz_o^2)(dW(Z)/dZ) + (dZ/dz_o)^2(d^2W(Z)/dZ^2) \qquad (3.27)$$

etc.

4. Use the ith order approximation of $(d^m W(z_o)/dz_o^m)_{m=1,2..}$, M_1, M_2, and the derivatives of M_1 and M_2 in the right hand side of Equation 3.23 to calculate the i+1th order approximation of $(d^m n(z_o)/dz_o^m)_{m=1,2..}$.

5. Iterate until two successive approximations agree within the desired accuracy.

The refined data of any particular nonequilibrium experimental configuration are now unambiguiusly determined. From these data it is possible to map either the temperature derivatives of the refractive index or the spatial derivatives of the temperature. Section 3.5 and 3.6 establish the mathematical procedures for calculation of $(d^m n/dT^m)_{m=1,2...}$ and $(d^m T/dz^m)_{m=1,2..}$ from the refined data, respectively.

3.5 Refractive Index: Temperature Dependence

For a one component liquid the temperature derivatives of the refractive index are simply related to the refined data, $(d^m n(z)/dz^m)_{m=1,2..}$, by the chain rule expressions

$$\begin{aligned} dn/dT &= (dz/dT)(dn/dz) \\ d^2n/dT^2 &= (d^2z/dT^2)(dn/dz) \\ &\quad + (dz/dT)^2(d^2n/dz^2) \\ &\text{etc.} \end{aligned} \tag{3.28}$$

These equations can be used to evaluate the temperature derivatives of the refractive index provided the temperature distribution is known. In the absence of unusual energy sources or anomalous energy fluxes, the temperature distribution is easily determined in the nonflowing, steady state by[72-74]

$$(d/dz)k(dT/dz) = 0 \tag{3.29}$$

where k is the thermal conductivity. Equation 3.29 must be solved subject to the boundary conditions

$$\begin{aligned} T(z) &= T_U \quad \text{at } z = 0 \\ T(z) &= T_L \quad \text{at } z = \underline{l} \end{aligned} \tag{3.30}$$

where T_U is the temperature of the upper plate, and T_L is the temperature of the lower plate.

The temperature dependence of the thermal conductivity is adequately described by the second order, truncated Taylor series[24]

$$\begin{aligned} k(T) &= k(T_M) + (dk(T_M)/dT)(T - T_M) \\ &\quad + (1/2)(d^2k(T_M)/dT^2)(T - T_M)^2 \end{aligned} \tag{3.31}$$

where T_M is the mean temperature defined by

3.5 Refractive Index: Temperature Dependence

For a one component liquid the temperature derivatives of the refractive index are simply related to the refined data, $(d^m n(z)/dz^m)_{m=1,2..}$, by the chain rule expressions

$$\begin{aligned} dn/dT &= (dz/dT)(dn/dz) \\ d^2n/dT^2 &= (d^2z/dT^2)(dn/dz) \\ &\quad + (dz/dT)^2(d^2n/dz^2) \\ &\text{etc.} \end{aligned} \tag{3.28}$$

These equations can be used to evaluate the temperature derivatives of the refractive index provided the temperature distribution is known. In the absence of unusual energy sources or anomalous energy fluxes, the temperature distribution is easily determined in the nonflowing, steady state by[72-74]

$$(d/dz)k(dT/dz) = 0 \tag{3.29}$$

where k is the thermal conductivity. Equation 3.29 must be solved subject to the boundary conditions

$$\begin{aligned} T(z) &= T_U \quad \text{at } z = 0 \\ T(z) &= T_L \quad \text{at } z = \underline{l} \end{aligned} \tag{3.30}$$

where T_U is the temperature of the upper plate, and T_L is the temperature of the lower plate.

The temperature dependence of the thermal conductivity is adequately described by the second order, truncated Taylor series[24]

$$\begin{aligned} k(T) &= k(T_M) + (dk(T_M)/dT)(T - T_M) \\ &\quad + (1/2)(d^2k(T_M)/dT^2)(T - T_M)^2 \end{aligned} \tag{3.31}$$

where T_M is the mean temperature defined by

$$T_M = T_U - \Delta T_o/2 = T_L + \Delta T_o/2 \qquad (3.32a)$$

and

$$\Delta T_o = T_U - T_L. \qquad (3.32b)$$

With Equations 3.31 and 3.30, the integrated form of Equation 3.29 is

$$c_1 z = \sum_{n=0}^{2} (1/(n+1)!)(d^n k(T_M)/dT^n)((T - T_M)^{n+1} - (\Delta T_o/2)^{n+1}) \qquad (3.33a)$$

where

$$c_1 = -\underline{1}^{-1}(k(T_M)\Delta T_o + (1/3)(d^2 k(T_M)/dT^2)(\Delta T_o/2)^3). \qquad (3.33b)$$

$T(z)$ is a root of Equation 3.33a (a cubic equation) and is defined to be $T_{3.33}(z)$. It is numerically computed from the above equations.

From the refined data associated with z_o in a particular steady state experiment, Equation 3.33a is used to determine $T(z_o)$. The temperature derivatives of Equation 3.33a, evaluated at $T(z_o)$, are used in Equation 3.28 to calculate $(d^m n(T)/dT^m)_{m=1,2..}$.

3.6 Temperature Distribution

When the temperature dependence of the refractive index is known, it is possible to map the temperature distribution from the refined data. By the chain rule,

$$dT/dz = (dn/dz)(dT/dn)$$

$$d^2T/dz^2 = (d^2n/dz^2)(dT/dn) + (dn/dz)(dT^2/dn^2) \qquad (3.34)$$

etc.

On the right hand side of these equations, the $(d^m n(z_o)/dz_o^m)_{m=1,2..}$ are known, and the $(d^m T(z_o)/dn^m)_{m=1,2..}$ can be calculated from the empirical cubic equation

$$n(T) = A + BT + CT^2 + DT^3 \qquad (3.35)$$

provided $T(z_o)$ is known. Equation 3.35 is adequate for visible wavelengths in the ordinary temperature range 20^oC to 40^oC. The coefficient of the cubic term is usually vanishingly small. Because $T(z_o)$ is an unknown, an iteration procedure is necessary. A suitable ith order iteration is:

1. Assume an ith order approximation to $T(z_o)$; calculate the ith order approximation to $(d^m T(z_o)/dz_o^m)_{m=1,2..}$ with Equations 3.34 and 3.35. A convenient 0th order approximation to $T(z_o)$ is

$$(T(z_o))_{0th} = T_U - (\Delta T_o/2)z_o. \qquad (3.36)$$

2. Calculate the i+1th order approximation to $T(z_o)$ from the Taylor expansion

$$T(z_o) = \sum_{m=0} (d^m T(z_o - \epsilon)/dz^m)(\epsilon^m/m!), \qquad (3.37)$$

where ϵ is some small distance, and T_U is known.

CHAPTER 4

NONISOTHERMAL, NONCONVECTING LIQUID STATES

4.1 Introduction

As temperature increases, liquid density decreases. Consequently, when a horizontal parallel plate apparatus is heated from above, the liquid density increases as the lower plate is approached. This results in a liquid layer which is stable to convective motion(provided that cell end effects are unimportant). All liquid motion decays to stable, time-independent, nonconvecting thermodynamic states. Far from boundary or interface, measurements of liquid temperature distribution in these nonequilibrium, nonconvecting states have shown that the temperature is described by the Fourier-Laplace equation

$$\nabla \cdot k \nabla T = 0. \tag{4.1}$$

For horizontal parallel plates in the absence of end effects, Equation 4.1 becomes

$$(d/dz)k(dT/dz) = 0 \tag{4.2}$$

where the temperature distribution, $T(z)$, is a function of the vertical coordinate, z, which is measured from the upper plate.

The parameter k of Equation 4.2 is experimentally found to be a liquid property. At ordinary temperatures

k depends to a small degree upon temperature; it is independent of temperature gradient. Highly nonlinear temperature distributions which may be found in regions for which Equation 4.2 may not be valid(i.e., near walls or interfaces) are described by the experimentally found temperature, T(z), minus the temperature predicted by Equation 4.2, $T_{3.33}$. Equation 3.33 is the solution to Equation 4.2 subject to the boundary conditions which are taken to be the temperature of the upper and lower silver plates; these are T_U and T_L, respectively. The function $T(z) - T_{3.33}(z)$ is called the deviation from linearity because the temperature dependence of k is so small at ordinary temperatures that the solution of Equation 4.2 is essentially linear in the vertical coordinate.

Joseph Fourier[1] called k(T) the "interior conducibility." He recognized that Equation 4.2 describes all energy flux in the absence of external effects through the Fourier heat flux relationship,

$$J_z = -k dT/dz, \qquad (4.3)$$

where J_z is the total heat flux in the z direction. We concur with Fourier but restate the external effects provision:

> Equation 4.2 describes T(z) in the nonflowing, steady state provided that z is far enough away from any boundary interface. The interface may be solid-liquid, solid-solid, solid-gas, liquid-gas, etc.

This statement is valid because there is no experimental evidence to the contrary. Equation 4.2 describes all

temperature distributions which have been observed far from boundaries.

In this chapter we present quantitative, experimental temperature distributions for ethyl acetate, benzene, and carbon tetrachloride. The nonlinear temperature distributions which are found near the bounding silver walls of these pure liquids demonstrate the failure of Equation 4.2 as the liquid-solid interface is approached. The temperature distributions are determined with the Bryngdahl interferometer and mathematical analysis described in Chapter 3. Analysis of the dependence of the nonlinearity upon the temperature difference

$$\Delta T_o = T_U - T_L > 0 \qquad (4.4)$$

is made, and the variation of the exhibited magnitude of the nonlinearity from liquid to liquid is established. Evidence is presented which suggests that Equation 4.2 describes the temperature distribution in water at all distances from the solid-water interface but with a temperature jump or discontinuity at the interface. Such temperature discontinuity may be viewed as a degenerate nonlinearity in the sense that the nonlinearity is over a distance too small to be observed with the Bryngdahl interferometric probe.

Irregular temperature distributions near liquid-solid interfaces have been reported by a number of authors. In 1933 Bates[2] found that "temperature drops" across the solid-liquid interfaces resulted in significant variations

in the experimentally determined thermal conductivities of water and red oil when the solid boundary was either copper or Duco lacquered copper. He reported that a surface effect exists which must be considered different from the effects of the boundary layers associated with convecting fluids.

In 1957 Longsworth[3] used a nonisothermal technique and Rayleigh interferometry to study the Soret coefficients of KCl solutions. The Rayleigh cell was sandwiched between horizontal parallel plates($\underline{l} \simeq 1$ cm, $\Delta T_o \simeq 10^oC$). Pure water was found to exhibit highly nonlinear temperature distributions near bounding surfaces of either silver or stainless steel. Longsworth reported that the "temperature drop" in water is 2.4% to 3% of ΔT_o with silver plates and 7% for stainless steel. He takes these temperature drops into account in the evaluation of Soret coefficients.

Neglect of nonlinear temperature distribution near walls can cause systematic error in experimental thermal conductivity calculations. Recognizing this, Poltz has developed the concept of "effective thermal conductivity" for liquids.[4-7] He defines an effective thermal conductivity,[4] k_{eff}, such that

$$k_{eff} = (\underline{l}/\Delta T_o)J_z = (\underline{l}/\Delta T_o)(J_c + J_r) \qquad (4.5a)$$

$$= k_c + (\underline{l}/\Delta T_o)J_r \qquad (4.5b)$$

where $\underline{l}$ is the distance between the horizontal parallel plates, and J_z is the total heat flux(W/cm^2) in the z direction. The conductive heat flux, J_c, is defined to

be the total heat flux, J_z, minus the radiative heat flux, J_r. All fluxes are in the vertical, z, direction. The parameter k_c defined in Equation 4.5b is called the "thermal conductivity" by Poltz. From these definitions it is apparent that Poltz uses k_{eff} as the parameter in Equation 4.2. Thus, the validity of Equation 4.2 in describing the temperature distribution is extended to all domains whether near or far from walls. Consequently, the effective thermal conductivity depends upon (1) cell geometry and (2) the nature and magnitude of the solid-liquid interaction. Because it is not generally a property of the liquid, the effective thermal conductivity of Poltz and the interior conducibility of Fourier are not identical. Analyzing what he perceives to be the radiative heat flux, Poltz finds

$$k_{eff} = k_c + (16n^2\sigma T^3/3\underline{k})Y(e,\tau) \qquad (4.6)$$

where $Y(e,\tau)$ is a function such that

$$\lim_{\underline{l}\to\infty} \quad Y(e,\tau) = 1 \qquad (4.7)$$

and where n and $\underline{k}$ are the average refractive index and average absorption coefficient(cm^{-1}) of the liquid media, respectively. e is the emissivity of the plate surfaces, and σ is the Stefan-Boltzmann constant:

$$\sigma = 5.66910 \times 10^{-9} \ Wcm^{-2}k^{-4}. \qquad (4.8)$$

The optical density, τ, is defined by

$$\tau = \underline{l}\underline{k}. \qquad (4.9)$$

Taking the limit of Equation 4.6 as $\underline{l}\to\infty$, making the

fundamental assumption that k_c is a liquid property which is independent of cell geometry, and employing Equation 4.7 we find

$$\lim_{\underline{l}\to\infty} k_{eff} = k_c + 16n^2\sigma T^3/3\underline{k}. \qquad (4.10)$$

Because the right-hand side of Equation 4.10 is the sum of two properties, the limit as $\underline{l}\to\infty$ of k_{eff} must be a property. Being both a liquid property and the thermal parameter of Equation 4.2, the limiting value of k_{eff} must be equivalent to Fourier's interior conducibility:

$$\lim_{\underline{l}\to\infty} k_{eff} = k. \qquad (4.11)$$

Poltz's experimental program for determination of the interior conducibility is: (1) measure $k_{eff}(\underline{l})$ with Equation 4.5a at several cell heights and (2) extrapolate the results to $\underline{l} = \infty$. This yields the interior conducibility by Equation 4.11. Using copper plates($e = 0.04$), Poltz finds an increase in k_{eff} for toluene of 7% when $\underline{l}$ is increased from zero to infinity at a mean temperature of 80°C.[4] When the mean temperature is 20°C, k_{eff} increases by 3.6% but the increases is 85% complete for the cell height of 3 mm. Similar increases of 4-7% are found for the weak infrared absorbing liquids: benzene, m-xylene, carbon tetrachloride, and paraffin.[5,6] The effective thermal conductivity of the strong infrared absorbers n-propanol, iso-propanol, n-butanol, sec-butanol, and iso-butanol increases by less than 1% with increasing $\underline{l}$.[7]

In related work Novotny and co-workers[8,9] have

evaluated the radiative contribution to energy transport for carbon tetrachloride using experimental, frequency dependent, absorption spectra. This seems to be the only work of its kind for a liquid.

Direct interferometric observation of temperature distribution near and far from walls has been reported. In 1970 Schodel and Grigull[10] used horizontal parallel plates heated from above in conjunction with a Mach-Zehnder interferometer to establish and determine temperature distribution. They found nonlinear temperature distributions for carbon tetrachloride, paraffin, and carbon disulfide, while water and methanol exhibited linear temperature distributions. Figure 4.1A reproduces their data for carbon tetrachloride. The magnitude of the temperature gradient shown in Figure 4.1A increases by 25% as the solid-liquid interface is approached from the cell center. There is also a central region($0.25 \leq z/l \leq 0.75$) in which the temperature gradient is constant. The cell height is 1.5 cm; therefore, the nonlinearity lies within 0.4 cm of the liquid-silver interface($e = 0.05$).

Olson and Horne have used nonisothermal Bryngdahl interferometry to study the refractive indices[11] and thermal conductivities[12] of pure liquids in a horizontal parallel plate arrangement. Finding parabolic steady state fringe shapes for carbon tetrachloride, cyclohexane, and benzene,[11] they suggest that the observed parabolas are caused by slight nonlinearities in the steady state temperature distribution. Further,

Figure 4.1

(A) Reduced temperature gradient, $(dT/dz)/(dT/dz)_{\underline{l}/2}$, versus $z/\underline{l}$ for carbon tetrachloride when $\underline{l}$ = 1.5 cm, e = 0.05, and $\Delta T_o = 2.00^oC$. From G. Schodel and U. Grigull.[10]

(B) Deviation from linearity, $T - T_{3.33}$, of CCl_4 in a cell 0.810 cm high. $T_U = 26.40^oC$, $T_L = 23.60^oC$. From J. D. Olson.[12]

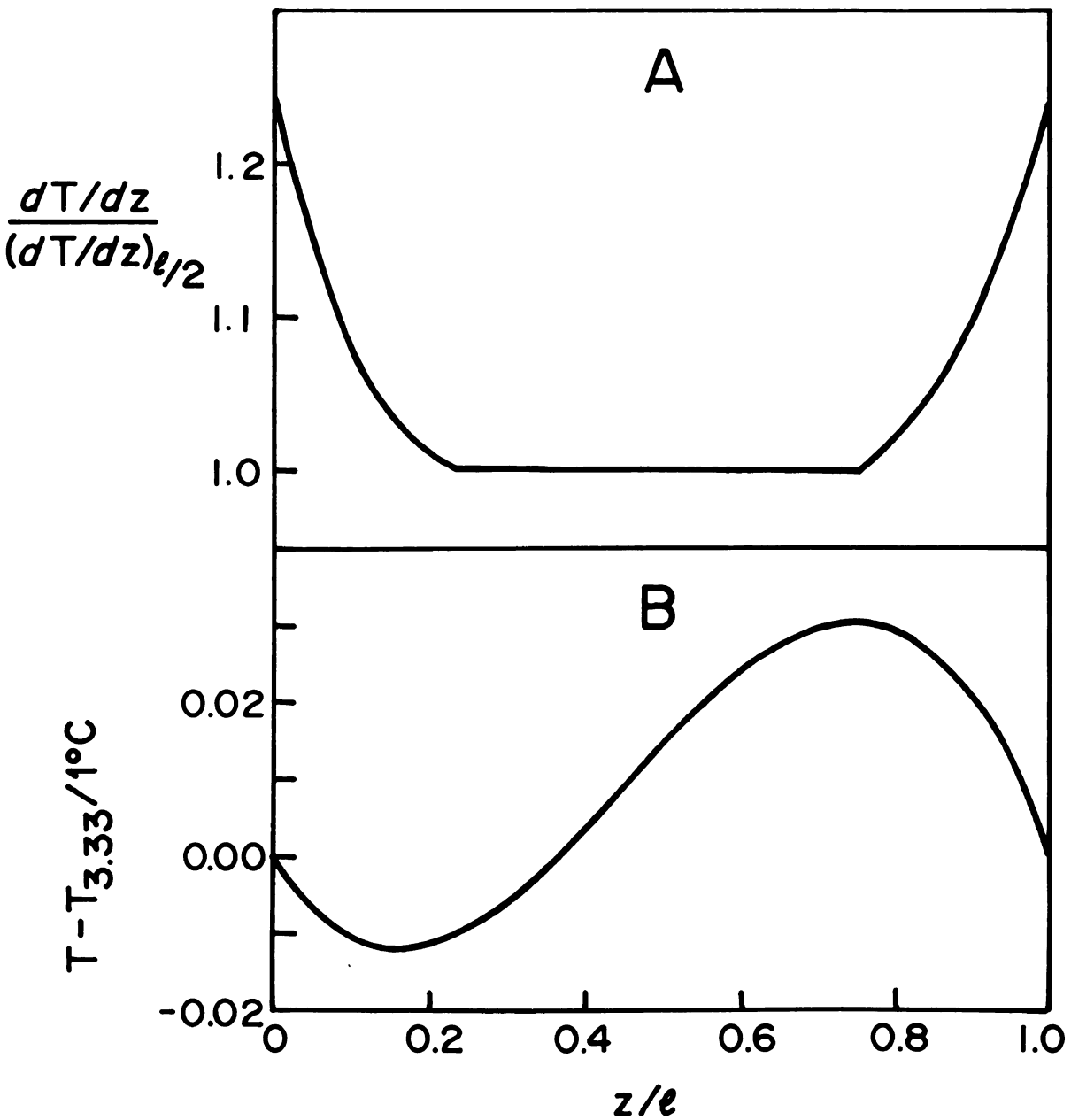
A
B
dT/dz
(dT/dz)ℓ/2
1.2
1.1
1.0
0.02
0.00
-0.02
T-T3.33/1°C
0
0.2
0.4
0.6
0.8
1.0
z/ℓ

they speculate that the unexpected nonlinearities are due to anomalous interactions between liquid and metal boundaries. Olson[12] has computed the temperature distribution necessary to explain the parabolic fringe shape exhibited by carbon tetrachloride between silver plates($\underline{l}$ = 0.810 cm, ΔT_o = 2.800°C). The resulting deviation from linearity is plotted versus $z/\underline{l}$ in Figure 4.1B. Near the upper plate the temperature is a maximum of 0.015°C less than the prediction of Equation 4.2. Near the lower wall the temperature is a maximum of 0.030°C greater than the prediction of Equation 4.2. In the central region (0.2 cm $\leq z \leq$ 0.55 cm) the temperature distribution is essentially linear.

Gurenkova et al[13] have used a double beam diffraction interferometer to evaluate temperature distributions. They found distributions qualitatively similar to those of Figure 4.1 for toluene, hexane, and octane. The nonlinearities for water and liquid alcohols were negligibly small.

4.2 Nonlinear Temperature Distributions: Ethyl Acetate, Benzene, Carbon Tetrachloride

All liquids studied are high purity. Methanol is "acetone free" Matheson, Coleman, and Bell A.C.S. Analyzed Reagent. Benzene is Matheson, Coleman, and Bell Spectroquality. Carbon tetrachloride is Baker Analyzed "Spectrophotometric" Reagent with 0.00 absorbance at 400 nm. Ethyl acetate is Mallinckrodt A.C.S. Analytical

Reagent. These organic reagents are freshly opened. Doubly distilled water with an electrical conductivity of o.4umho/cm is degassed by boiling just prior to use. This eliminates troublesome air bubbles within the liquid cell.

When the large temperature gradients needed to study nonlinear temperature distributions are applied to the pure organic liquids, strong refraction of the interferometric light beam causes the beam to be refracted completely out of the optical train. This makes it impossible to count photometrically the number, N(H/2), of fringes which evolve at the image center, and the experimental procedure of Section 3.3 must be altered. All isothermal experimental aspects remain unchanged he nonisothermal aspects are modified as follows: once the nonequilibrium, steady state temperature distribution is established, lens L1 is lowered until (1) the interferometric light beam traverses the optical train, and (2) the cell face is sharply focused. The fringe shape is measured from a photograph of the steady state image. Assuming T(H/2) is the mean of T_U and T_L, N(H/2) is calculated from Equation 3.6. The sum of the fringe shape and N(H/2) is the fringe number, N(Z).

Table 4.1 contains the indices of refraction at 632.8 nm which are used with the methods of Section 3.6 to evaluate the temperature distribution, T(z). In computing these functions, the temperature dependent

Table 4.1

Temperature dependence of refractive indices: $n = a + bT + cT^2$ at 632.8 nm, 1 atm. σ is the uncertainty in a computed value of n; T is in ^{o}C.

Liquid	a	$10^4 b/^{o}C^{-1}$	$10^6 c/^{o}C^{-2}$	σ	Reference
H_2O	1.333499	-0.4459	-1.2510	3×10^{-5}	Waxler et al[14]
C_6H_6	1.510525	-6.3395	0.1046	1×10^{-5}	Reisler et al[15]
CCl_4	1.470218	-5.8478	-0.2407	1×10^{-5}	Reisler et al[15]
CH_3OH	1.334830	-3.7430	-0.1847	1×10^{-5}	Reisler et al[15]
$CH_3COOC_2H_5$	1.3810	-5.0	0.0	$\geq 10^{-4}$	Johnson and Smith[16]

parameters A(T), B(T), and C(T) of Cauchy's formula,[20]

$$n(T,\lambda) = A(T) + B(T)/\lambda^2 + C(T)/\lambda^4, \qquad (4.12)$$

are evaluated by the method of least squares from reported refractive indices at specific temperature and variable wavelength. A(T), B(T), and C(T) are then fitted to the best quadratic temperature equation with the least squares method. Table 4.1 lists the final results evaluated at 632.8 nm. The standard deviation of $n(T,\lambda)$ determined in this manner agrees with the experimental data within the reported experimental uncertainty. Table 4.2 lists thermal conductivity functions used in the calculation of $T_{3.33}$.

Two aspects of the data reduction must be justified: (1) neglect of the pressure dependence of refractive indices and (2) Equation 3.24. Concerning the pressure dependence, $(\partial n/\partial P)_T = 5.057 \times 10^{-5}$ atm^{-1} for benzene at 24.80°C, 1 atm, and 643.9 nm;[14] $(\partial n/\partial P)_T = 1.462 \times 10^{-5}$ atm^{-1} for water at 23.1°C, 1 atm, and 589.3 nm;[21] and $(\partial n/\partial P)_T = 4.056 \times 10^{-5}$ atm^{-1} for methanol at 22.8°C, 1 atm, and 589.3 nm.[21] Thus, a fluctuation of 0.1 atm causes a refractive index fluctuation which is smaller than the experimental uncertainties reported in Table 4.1. Furthermore, since $(\partial n/\partial T)_P = -1.071 \times 10^{-4}$ °C^{-1} for water at 1 atm and 632.8 nm, the refractive index of water decreases by about 10^{-3} units during a temperature increase of 10°C, a typical temperature difference between plates; but the refractive index increases by about 5×10^{-6} units during a pressure increase of 0.1 atm. Even at these large variations of

Table 4.2

Temperature dependence of thermal conductivity: $10^6 k = a + bT + cT^2$, $d \leq T \leq e$ at 1 atm. k is in W/cm °C; T is in °C.

Liquid	a	b	c	d/°C	e/°C	Reference
H_2O	5620.0	20.22	-0.08230	0	100	McLaughlin(1964)[17]
C_6H_6	1527	-2.608	0.0	15	71	Tsederberg(1965)[18]
$CH_3COOC_2H_5$	1528	-3.018	0.0	16	50	Tsederberg(1965)[18]
CCl_4	1087.57	-1.913772	0.0	-18	105	Powell et al(1966)[19]

pressure, the pressure induced refractive index variation is less than 1% of a typical temperature induced variation. These points justify the neglect of pressure variation.

Equation 3.24 asserts that when the cell face is focused:

$$Z(z_o) = (H/\underline{l})z_o \qquad (4.13)$$

where Z is the vertical image coordinate of a photon pencil which enters the liquid at the vertical coordinate z_o; $\underline{l}$ is the cell height; and H is the isothermal image height. In general this simple relationship is incorrect. Alterations in relative lens position during the isothermal-nonisothermal experimental sequence cause changes in the magnification factor which is $H/\underline{l}$ in Equation 4.13. To prove the validity of Equation 4.13 for our experimental procedure, the nonisothermal image height predicted by Equation 4.13 is compared to the experimental, nonisothermal image height. Isothermal and nonisothermal image hieghts differ because light is refracted toward the lower temperatures, which causes a portion of the interferometric radiation to strike the lower silver plate. This portion is reflected out of the optical train, thereby reducing the image height in the nonisothermal, experimental configuration. It is easily seen from Figure 4.2 that the cross section of the interferometric beam leaving the cell-plate composite will have the effective height($\underline{l}_{eff}$) given by

$$\underline{l}_{eff} = \underline{l} - z_{end}(0) \qquad (4.14)$$

Figure 4.2

Light refraction in a nonisothermal experimental configuration; $T_U > T_L$. The pencil of light shown enters the liquid at $z_0 = 0$. It leaves at coordinate $z_f(0)$ and angle $\alpha_f(0)$. This pencil travels through the glass cell at angle $\beta_f(0)$, refracts in air, and travels at angle $\gamma_f(0)$ until direction is altered by the Bryngdahl optical train.

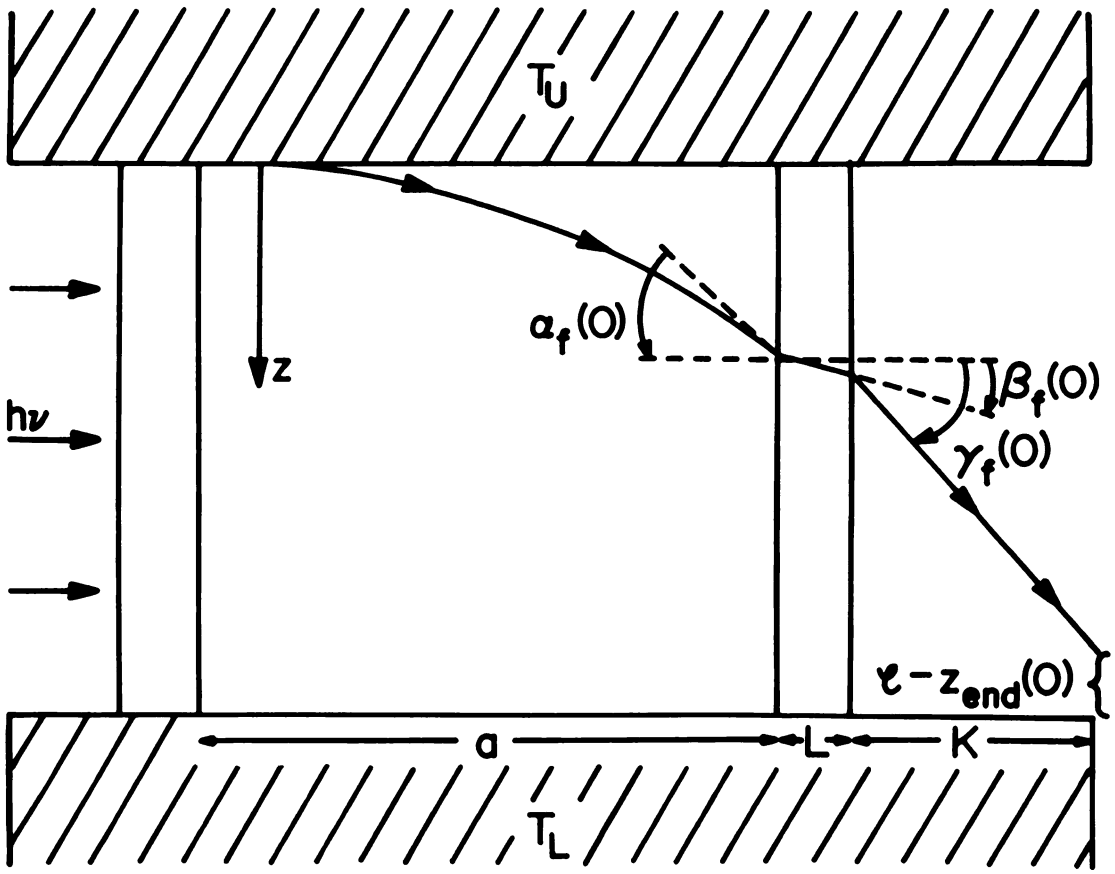
T_U
$\alpha_f(0)$
z
$h\nu$
$\beta_f(0)$
$\gamma_f(0)$
$\ell - z_{end}(0)$
a
L
K
T_L

where $z_{end}(0)$ is the vertical coordinate of the light pencil, which enters the cell at $z_o = 0$, passing beyond the silver plate. From the definition of $z_{end}(0)$, we have the trigonometric relationship

$$z_{end}(0) = z_f(0) + L \tan \beta_f(0) + K \tan \gamma_f(0) \quad (4.15)$$

where the distances L and K are defined in Figure 4.1. L and K are 0.635 cm and 2.450 cm, respectively. The angles $\alpha_f(0)$, $\beta_f(0)$, and $\gamma_f(0)$ are also defined in Figure 4.2. They are related by Snell's refraction law by[22]

$$n_f(0)\sin \alpha_f(0) = n_{glass}\sin \beta_f(0)$$
$$= n_{atm}\sin \gamma_f(0). \quad (4.16)$$

$n_f(0)$ is the liquid refractive index experienced by the upper most light pencil leaving the liquid. The refractive index of glass, n_{glass}, is 1.52; the refractive index of air, n_{atm}, is 1.000276.[23] From Equations 4.14, 4.15, and 4.16, we have

$$\underline{l} - \underline{l}_{eff} = z_f(0) + L \tan \sin^{-1}((n_f(0)/n_{glass}(0))\sin \alpha_f(0))$$
$$+ K \tan \sin^{-1}((n_f(0)/n_{atm})\sin \alpha_f(0)). \quad (4.17)$$

To find $\alpha_f(0)$, we have

$$\tan \alpha = dz/dy = ((n(z)/n(z_o))^2 - 1)^{1/2} \quad (4.18)$$

by Equation 3.12. Furthermore, combining Equations 3.16a, 3.18b, and 4.18 and evaluating the results at y = a = 5.986 cm, we have

$$\alpha_f(0) = \tan^{-1}\left(\sum_{v=1}^{2} M_v(M_1(2M_2)^{-1}(\cosh(M_2^{1/2}a) - 1))^v\right). \quad (4.19)$$

Equations 4.17 and 4.19 can now be used to calculate $\underline{l}_{eff}$. Equation 4.13 is correct if $(H/\underline{l})\underline{l}_{eff} = H_{eff}$ equals the experimentally determined, nonisothermal, image height. Table 4.3 includes the isothermal shear parameter(2D), the interfringe distance(δ), the isothermal and nonisothermal experimental image heights, and the computed effective height, H_{eff}. The last column is the per cent deviation of the calculated height from the experimentally determined height. In all instances, the deviation is 1% or less. Because deviations of this magnitude are within the uncertainty of the measured value of H, the validity of Equation 3.24 is established.

Figures 4.3 through 4.7 are photographic prints of nonisothermal configuration images of water, ethyl acetate, benzene, carbon tetrachloride, and methanol. The fringe shapes exhibited at different ΔT_o may be qualitatively discussed if we temporarily neglect the bending of light in a temperature gradient. Then the fringe number, N(z), is simply related to the temperature gradient by Equation 3.6:

$$N(z) \simeq (2Da\underline{l}/\lambda H)(dn/dT)(dT/dz). \qquad (4.20)$$

dn/dT data of Table 4.1 are linear functions of temperature in the temperature range of interest for all liquids. Thus, if dT/dz is a constant independent of z, N(z) is expected to be a linear function of z by Equation 4.20. This expectation is confirmed at all ΔT_o from the Figure 4.3 nonisothermal data for water. Water,

Table 4.3

Isothermal and nonisothermal image data.

% deviation ≡ $100(H - H_{eff})/H$. The isothermal parameters for methanol and ethyl acetate are identical. $\underline{l}$ = 1.349 cm.

Liquid	$\Delta T_o/^oC$	$T_L/^oC$	2D/cm	δ/cm	H/cm	H_{eff}/cm	% deviation
C_6H_6	0.0		0.200	0.539	4.560		
	2.399	22.539			4.450	4.450	0.00
	7.256	22.660			4.240	4.227	0.31
	10.529	22.743			4.088	4.077	0.28
	13.063	22.839			3.955	3.961	-0.15
CCl_4	0.0		0.151	0.439	3.445		
	2.637	22.423			3.341	3.357	-0.48
	5.976	22.467			3.242	3.245	-0.10
	7.729	22.566			3.150	3.186	-1.15
	12.713	22.756			2.990	3.017	-0.92
CH_3OH	0.0		0.220	0.548	4.628		
	4.739	20.921			4.500	4.486	0.31
	9.297	21.296			4.341	4.348	-0.17
	12.125	21.565			4.252	4.262	-0.24
	13.488	22.044			4.225	4.220	0.13
H_2O	0.0		0.214	0.574	4.578		
	10.028	23.159			4.504	4.479	0.55
	13.047	23.307			4.488	4.442	1.03
	16.691	23.486			4.396	4.391	0.10

Figure 4.3

Nonisothermal Bryngdahl interferometric image of water at several temperature differences between upper and lower silver plates. $\underline{l}$ = 1.349 cm; ΔT_o = 10.028°C, 13.047°C, and 16.691°C.

Water (H_2O)

1 cm

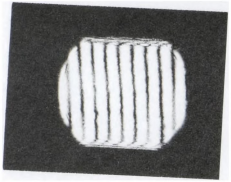

$\Delta T = 10.03^{\circ}C$

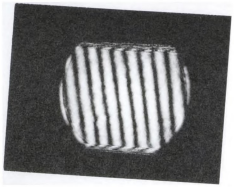

$\Delta T = 13.05^{\circ}C$

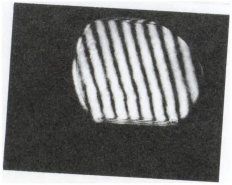

$\Delta T = 16.69^{\circ}C$

Figure 4.4

Nonisothermal Bryngdahl interferometric image of ethyl acetate at several temperature differences between upper and lower silver plates. $\underline{l}$ = 1.349 cm; ΔT_o = 2.244°C, 6.261°C, and 10.019°C.

Ethyl Acetate ($CH_3COOC_2H_5$)

1 cm

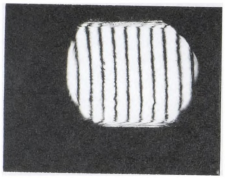

$\Delta T = 2.24^\circ C$

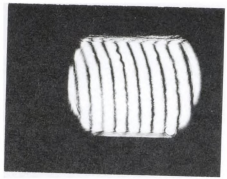

$\Delta T = 6.26^\circ C$

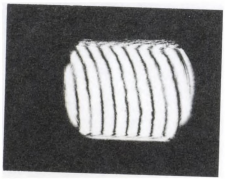

$\Delta T = 10.02^\circ C$

Figure 4.5

Nonisothermal Bryngdahl interferometric image of benzene at several temperature differences between upper and lower silver plates. $\underline{l}$ = 1.349 cm; ΔT_o = 2.399°C, 7.256°C, 10.529°C, and 13.063°C.

Benzene (C_6H_6)

1 cm

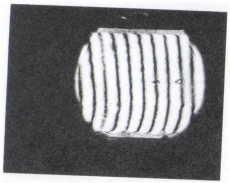

$\Delta T = 2.40^{\circ}C$

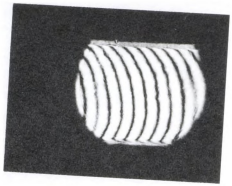

$\Delta T = 7.26^{\circ}C$

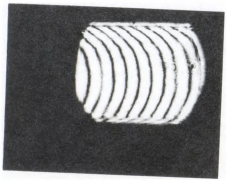

$\Delta T = 10.53^{\circ}C$

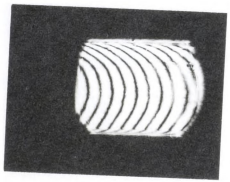

$\Delta T = 13.06^{\circ}C$

Figure 4.6

Nonisothermal Bryngdahl interferometric image of carbon tetrachloride at several temperature differences between upper and lower silver plates. $\underline{l}$ = 1.349 cm; ΔT_o = 2.637°C, 5.976°C, 7.729°C, and 12.713°C.

Carbon Tetrachloride (CCl_4)

1 cm

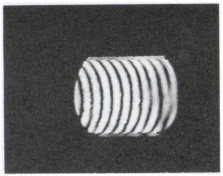

$\Delta T = 2.64^{\circ}C$

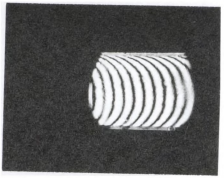

$\Delta T = 5.98^{\circ}C$

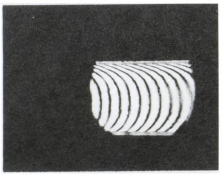

$\Delta T = 7.73^{\circ}C$

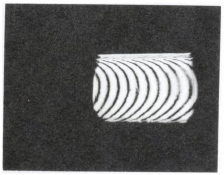

$\Delta T = 12.71^{\circ}C$

Figure 4.7

Nonisothermal Bryngdahl interferometric image of methanol at several temperature differences between upper and lower silver plates. $\underline{l}$ = 1.349 cm; ΔT_o = 4.739°C, 9.297°C, 12.125°C, and 13.488°C.

Methanol (CH_3OH)

1 cm

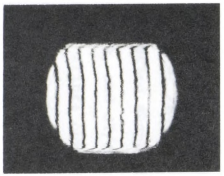

$\Delta T = 4.74\,^{\circ}C$

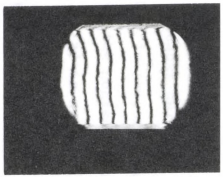

$\Delta T = 9.30\,^{\circ}C$

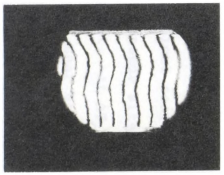

$\Delta T = 12.12\,^{\circ}C$

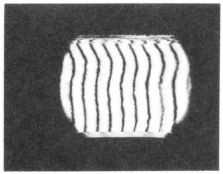

$\Delta T = 13.49\,^{\circ}C$

therefore, seems to satisfy Equation 3.33; Equation 3.33 describes the temperature distribution within observable distances from the silver-water interfaces. The temperature dependence of dn/dT for ethyl acetate, benzene, carbon tetrachloride, and methanol is only 1/10th to 1/5th that of water. Because dn/dT is essentially constant for these liquids, N(z) is proportional to the temperature derivative, dT/dz. From the nonisothermal images of ethyl acetate in Figure 4.4, N(z) is nearly independent of z at $\Delta T_o = 2.24^oC$; therefore, dT/dz is essentially a constant. However, at $\Delta T_o = 6.26^oC$, N(z) develops curvature near both the upper and lower plates. This indicates nonlinear temperature gradients in these domains. At $\Delta T_o = 6.26^oC$ and intermediate values of the vertical coordinate, the fringe shape is seen to be a linear function of the vertical coordinate. This is the expected shape when dn/dT depends slightly upon temperature, and dT/dz is a constant. At $\Delta T_o = 10.02^oC$ very pronounced fringe curvature is seen near both upper and lower silver-ethyl acetate interfaces; the central region still displays the expected linear fringe shape. These qualitative observations indicate (1) nonlinear temperature distribution near the silver-ethyl acetate interface, (2) the magnitude of the nonlinearity increases with increasing ΔT_o, and (3) there is a central region in which dT/dz is constant.

Qualitatively comparable results are found for benzene and carbon tetrachloride in Figures 4.5 and 4.6,

respectively. Only the magnitude of the nonlinearity and its extension from the metal-liquid interface vary between ethyl acetate, benzene, and carbon tetrachloride. Methanol exhibits a characteristically different fringe pattern in Figure 4.7. In the methanol nonisothermal images, the expected vertical fringe pattern has small amplitude wiggles superimposed upon it. The wiggles are time independent with amplitude which grow slightly with increasing ΔT_o. By placing a rubber bulb over the cell fill holes and "plunging," the wiggles could be made to oscillate frantically with large amplitude at high ΔT_o. These time dependent fringe shapes are characteristic of turbulent convection which strongly suggests that the irregular, time independent wiggles are caused by laminar convection. Observed laminar and turbulent motion experimentally proves the importance of end effects in the present apparatus, and the characteristic wiggles provide a convenient test for such liquid motion. For example, ethyl bromide is found to exhibit steady state fringe shapes identical to those of methanol, but the time dependent behavior can be induced at much lower ΔT_o. Thus, both methanol and ethyl bromide are unsuitable for studies of temperature distribution in nonconvecting media. The characteristic fringe pattern of methanol is also observed for ethyl acetate at ΔT_o above 12^oC, indicating a critical, liquid dependent ΔT_o above which end effects become important through their production of

convection.

To analyze quantitatively for temperature distribution, the fringe numbers are fitted in a least squares sense to spatial polynomials of degree 3 to 6. The method employed uses orthogonal Chebyshev polynomials in the discrete range.[24] Results are reported in Table 4.4. The raw data are processed by methods described in Sections 3.3 and 3.4. Temperature distributions are mapped by the method of Section 3.6 with the refractive index temperature derivatives given in Table 4.1. The temperature at $z = \underline{1}/2$ is assumed to be given by Equation 3.33 subject to the boundary conditions $T(0) = T_U$, $T(\underline{1}) = T_L$. $T_{3.33}(z)$ is computed from Equation 3.33 subject to the calculated boundary temperatures. The resulting deviation from linearity, $T(z) - T_{3.33}(z)$, for benzene and carbon tetrachloride are recorded in Figures 4.8 and 4.9, respectively.

Certain features of these figures are clear: (1) a negative deviation from linearity exists near the upper silver-liquid interface, (2) a positive deviation exists near the lower silver-liquid interface, (3) the deviation magnitude depends upon ΔT_o, and (4) a central region exists in which the deviation from linearity is linear in the vertical coordinate. There are some disturbing aspects of these figures. First, because both upper and lower plates are identical, we expect a high degree of symmetry with respect to inversion through the cell center. Figures 4.8 and 4.9 have far larger negative deviations

Table 4.4

Nonisothermal fringe number: $N\delta = \sum_{i=0}^{6} a_i x^i$ where $x = (Z - 0.254\ \text{cm})/0.254\text{cm}$.

Z and Nδ are in cm.

Benzene

ΔT_o/°C	T_L/°C	a_0/cm	$10^2 a_1$/cm	$10^2 a_2$/cm	$10^3 a_3$/cm	$10^4 a_4$/cm	$10^5 a_5$/cm	$10^6 a_6$/cm
2.399	22.539	3.488	- 6.339	0.8275	- 0.5313	0.1633	0.0	0.0
7.256	22.660	10.896	-26.12	2.682	-1.452	0.4024	0.0	0.0
10.529	22.743	15.550	-36.88	3.111	2.534	-6.646	4.745	-1.136
13.063	22.839	19.376	-65.48	12.91	-14.87	9.230	-2.171	0.0

Carbon Tetrachloride

2.637	22.423	3.127	-26.28	5.120	- 4.491	1.776	0.0	0.0
5.976	22.467	7.045	-49.91	10.58	-10.58	4.409	0.0	0.0
7.729	22.566	9.093	-81.22	25.92	-46.79	47.52	0.0	0.0
12.713	22.756	14.126	-68.42	16.12	-16.41	7.290	0.0	0.0

Ethyl Acetate

2.244	22.544	2.805	- 0.900	0.0007	0.0272	0.0	0.0	0.0
6.261	22.637	8.131	-12.52	1.217	- 0.6836	0.1725	0.0	0.0
10.019	22.869	12.859	-17.89	2.303	- 1.884	0.6364	0.0	0.0

Figure 4.8

Temperature deviation from linearity, $T(z) - T_{3.33}(z)$, for benzene at several temperature differences between upper and lower silver plates. The refractive index temperature derivatives of Table 4.1 are used in the method of Section 3.6 to compute $T(z)$ from the refined experimental data. $\underline{l}$ = 1.349 cm.

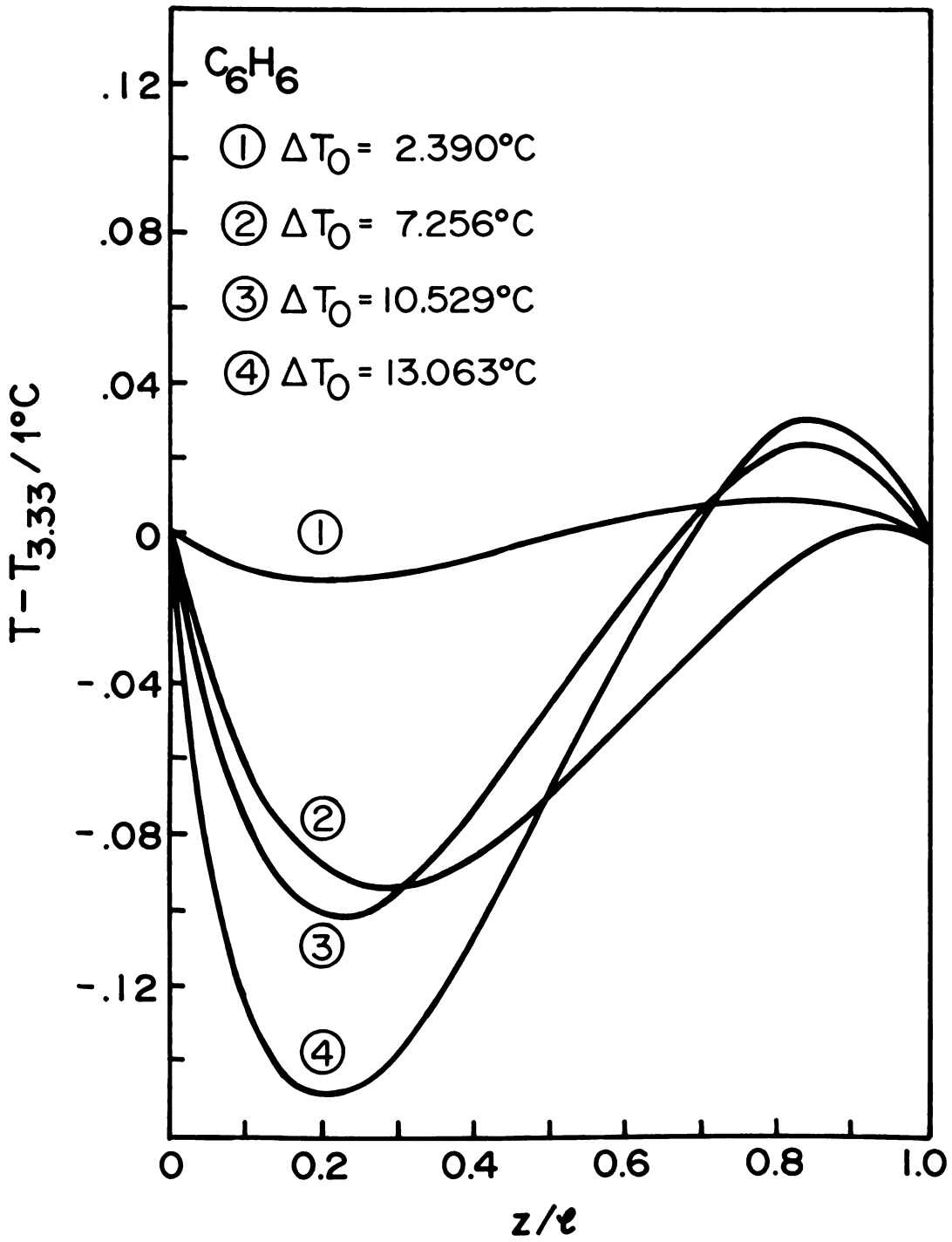
C_6H_6
① ΔT_0 = 2.390°C
② ΔT_0 = 7.256°C
③ ΔT_0 = 10.529°C
④ ΔT_0 = 13.063°C
.12
.08
.04
0
-.04
-.08
-.12
$T - T_{3.33}$ / 1°C
0
0.2
0.4
0.6
0.8
1.0
z/ℓ

Figure 4.9

Temperature deviation from linearity, $T(z) - T_{3.33}(z)$, for carbon tetrachloride at several temperature differences between upper and lower silver plates. The refractive index temperature derivatives of Table 4.1 are used in the method of Section 3.6 to compute $T(z)$ from the refined experimental data. $\underline{l}$ = 1.349 cm.

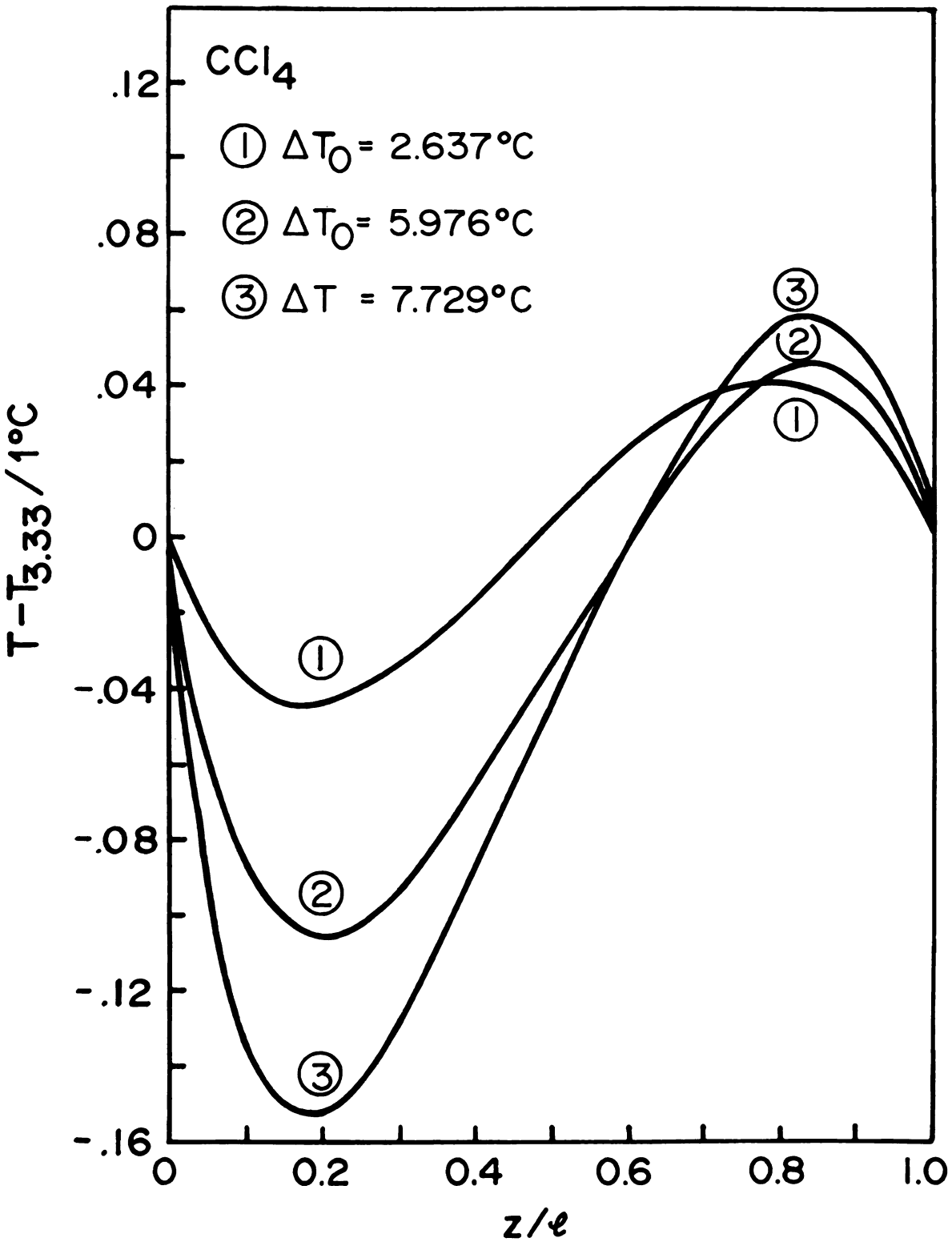
CCl4
① ΔT0 = 2.637°C
② ΔT0 = 5.976°C
③ ΔT = 7.729°C
.12
.08
.04
0
-.04
-.08
-.12
-.16
T−T3.33/1°C
0
0.2
0.4
0.6
0.8
1.0
z/ℓ

from linearity than positive; other curves are found with far larger positive deviation than negative. Second, we expect a regular increase in deviation with increasing ΔT_o; yet, near the lower plate an irregularity is found for benzene($\Delta T_o = 7.26^oC$). Systematic error, due to lens aberrations, is the cause of these disturbing points. Lowering lens L1 to bring the interferometric light beam back into the optical train and to refocus the cell face causes a repositioning of the light beam upon each lens. For example, in the isothermal configuration the light beam passes through the center of each lens. The need to lower L1 in the nonisothermal configuration, however, causes the light beam to traverse L1 just below center, L2 just above center, etc. This results in systematic distortion of the cell image. Correction for the distortion is made as follows.

Choose two points, z_1 and z_2, a distance m apart such that

$$z_1 = (\underline{l} - m)/2, \text{ and } z_2 = (\underline{l} + m)/2. \qquad (4.21)$$

Furthermore, choose the distance m such that

$$dT(z_1)/dz = dT(z_2)/dz = dT(\underline{l}/2)/dz, \qquad (4.22)$$

and make the following definitions:

$$dn(T)/dT \equiv A + BT, \qquad (4.23)$$

$$I_1 \equiv \int_{z_1}^{z_2} (dn/dz)dz, \text{ and} \qquad (4.24)$$

$$I_2 \equiv \int_{z_1}^{z_2} (d^2n/dz^2)dz. \qquad (4.25)$$

The integrals I_1 and I_2 are numerically evaluated from the refined, experimental data. Equations 4.21 to 4.25 can be combined and manipulated to show that

$$B = I_2/m(dT(\underline{l}/2)/dz)^2 \tag{4.26}$$

where B is defined by Equation 4.23. Equation 4.26 is used to estimate B by approximately the temperature derivative as $-\Delta T_o/\underline{l}$. Equations 4.21 to 4.25 can also be combined and manipulated to show that

$$aA^2 + bA + C = 0 \tag{4.27a}$$

where

$$a = T(\underline{l}/2)I_2 \tag{4.27b}$$

$$b = m(dn(\underline{l}/2)/dz)^2 - I_1 dn(\underline{l}/2)/dz + 2T(\underline{l}/2)I_2 B \tag{4.27c}$$

$$c = (I_2 B(T(\underline{l}/2))^2 - I_1 dn(\underline{l}/2)/dz)BT(\underline{l}/2). \tag{4.27d}$$

The final parameter of Equation 4.23, A, is the root of Equation 4.27. In this manner, the parameters A and B have been effectively adjusted so as to satisfy the condition stated in Equation 4.22; image distortions are thereby contained within these parameters. Choosing $m = 0.2\underline{l}$, the resulting parameters are reported in Table 4.5.

With the refractive index temperature derivatives of Table 4.5 and the methods of Section 3.6, the temperature distributions shown in Figure 4.10 through 4.12 are mapped. These figures are temperature deviation from linearity corrected for interferometric image distortion. They show

Table 4.5

Experimentally determined refractive index temperature derivatives: $dn/dT = A + BT$. A and B differ from literature values of Table 4.1 because of nonisothermal interferometric image distortion. ΔT is the interferometrically determined temperature difference $T(0) - T(\underline{l})$; $(dT/dz)_{\underline{l}/2}$ is also determined interferometrically. ΔT and $(dT/dz)_{\underline{l}/2}$ are computed with the refractive index derivatives of this table. T is in ^{o}C. $\underline{l} = 1.349$ cm.

Liquid	$\frac{\Delta T_o/\underline{l}}{^{o}C/cm}$	$10^4 A/^{o}C^{-1}$	$10^6 B/^{o}C^{-2}$	$\frac{\Delta T/\underline{l}}{^{o}C/cm}$	$\frac{-(dT/dz)_{\underline{l}/2}}{^{o}C/cm}$
$CH_3COOC_2H_5$	1.663	-4.501	-2.009	1.672	1.661
	4.641	-3.537	-5.506	4.695	4.640
	7.427	-4.363	-2.150	7.499	7.415
C_6H_6	1.778	-5.942	-1.172	1.798	1.761
	5.379	-4.536	-6.149	5.509	5.369
	7.805	-5.764	-1.460	7.961	7.744
	9.683	-5.578	-1.897	9.951	9.649
CCl_4	1.955	-7.152	6.984	2.119	1.962
	4.430	-4.707	-3.777	4.666	4.412
	5.729	-5.036	-2.408	6.047	5.705
	9.424	-6.040	1.436	9.958	9.501

Figure 4.10

Temperature deviation from linearity, $T(z) - T_{3.33}(z)$, for ethyl acetate at several temperature differences between upper and lower silver plates. These curves are corrected for image distortion by using the refractive index temperature derivatives of Table 4.5 in the method of Section 3.6 to compute T(z) from the refined experimental data. $\underline{l}$ = 1.349 cm.

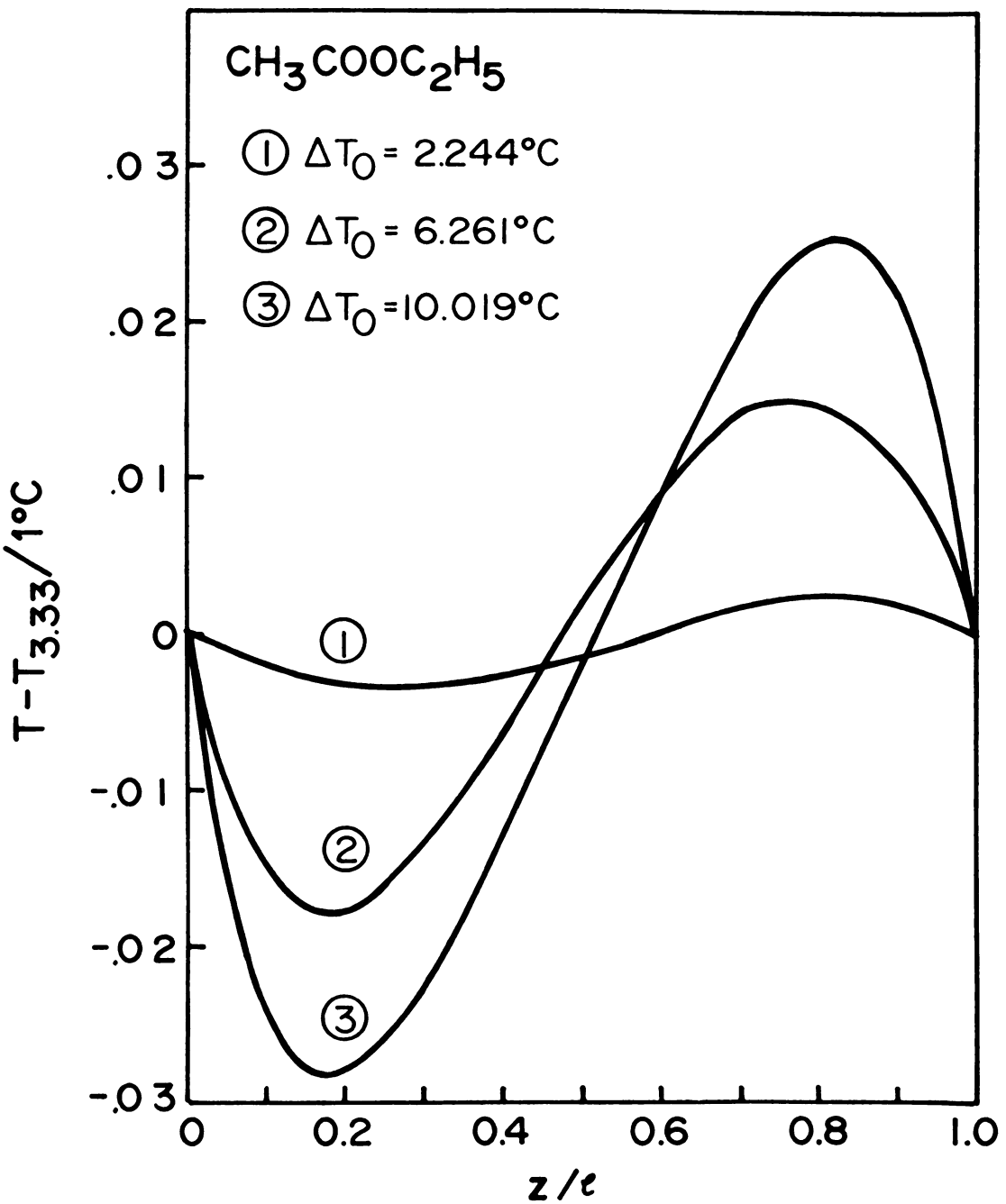
$CH_3COOC_2H_5$
① ΔT_0 = 2.244°C
② ΔT_0 = 6.261°C
③ ΔT_0 =10.019°C
.03
.02
.01
0
-.01
-.02
-.03
$T-T_{3.33}/1°C$
0
0.2
0.4
0.6
0.8
1.0
z/ℓ

Figure 4.11

Temperature deviation from linearity, $T(z) - T_{3.33}(z)$, for benzene at several temperature differences between upper and lower silver plates. These curves are corrected for image distortion by using the refractive index temperature derivatives of Table 4.5 in the method of Section 3.6 to compute T(z) from the refined experimental data. $\underline{l}$ = 1.349 cm.

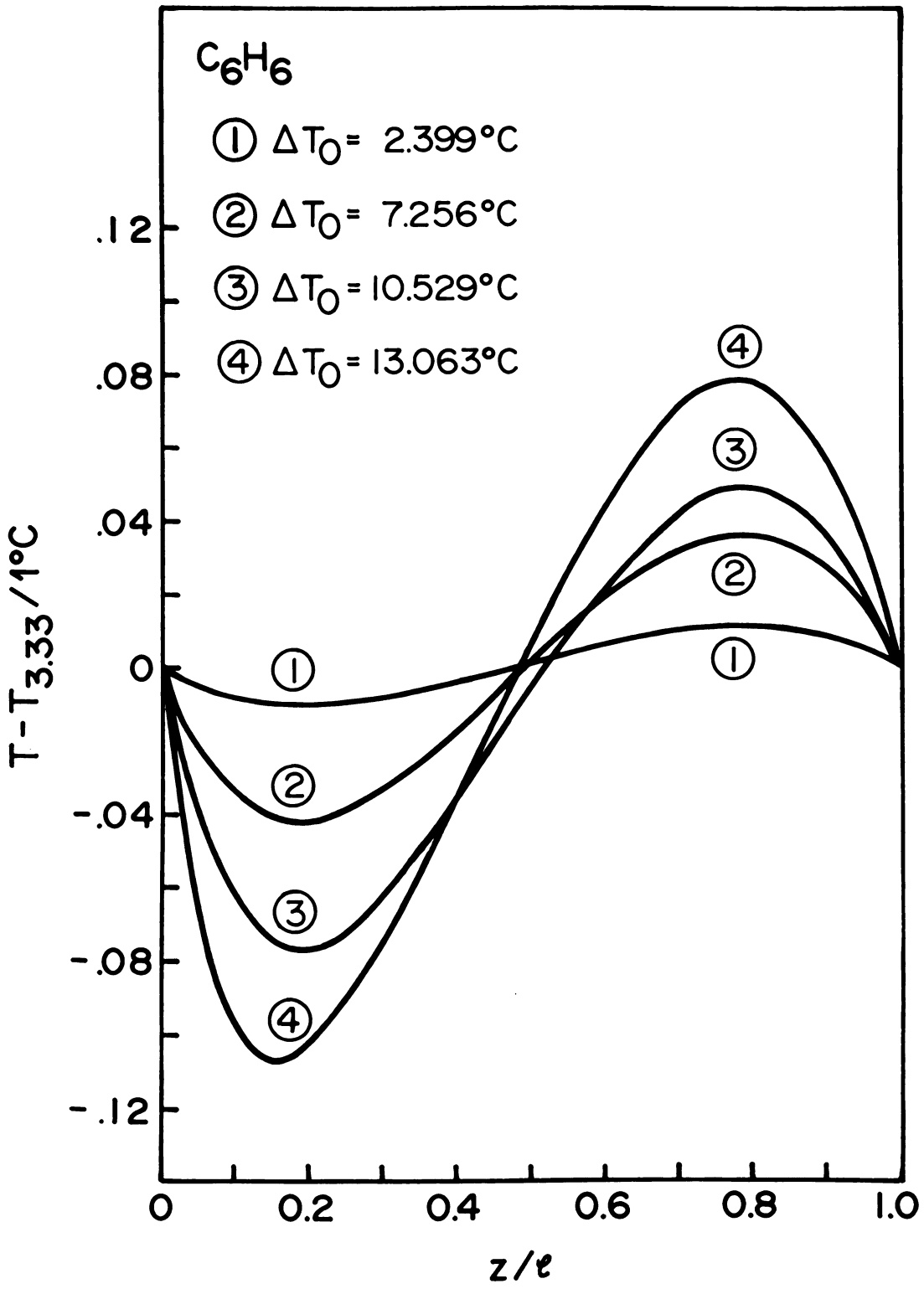
C6H6
① ΔT0 = 2.399°C
② ΔT0 = 7.256°C
③ ΔT0 = 10.529°C
④ ΔT0 = 13.063°C
.12
.08
.04
0
-.04
-.08
-.12
T-T3.33/1°C
0
0.2
0.4
0.6
0.8
1.0
z/ℓ

Figure 4.12

Temperature deviation from linearity, $T(z) - T_{3.33}(z)$, for carbon tetrachloride at several temperature differences between upper and lower silver plates. These curves are corrected for image distortion by using the refractive index temperature derivatives of Table 4.5 in the method of Section 3.6 to compute T(z) from the refined experimental data. $\underline{l}$ = 1.349 cm.

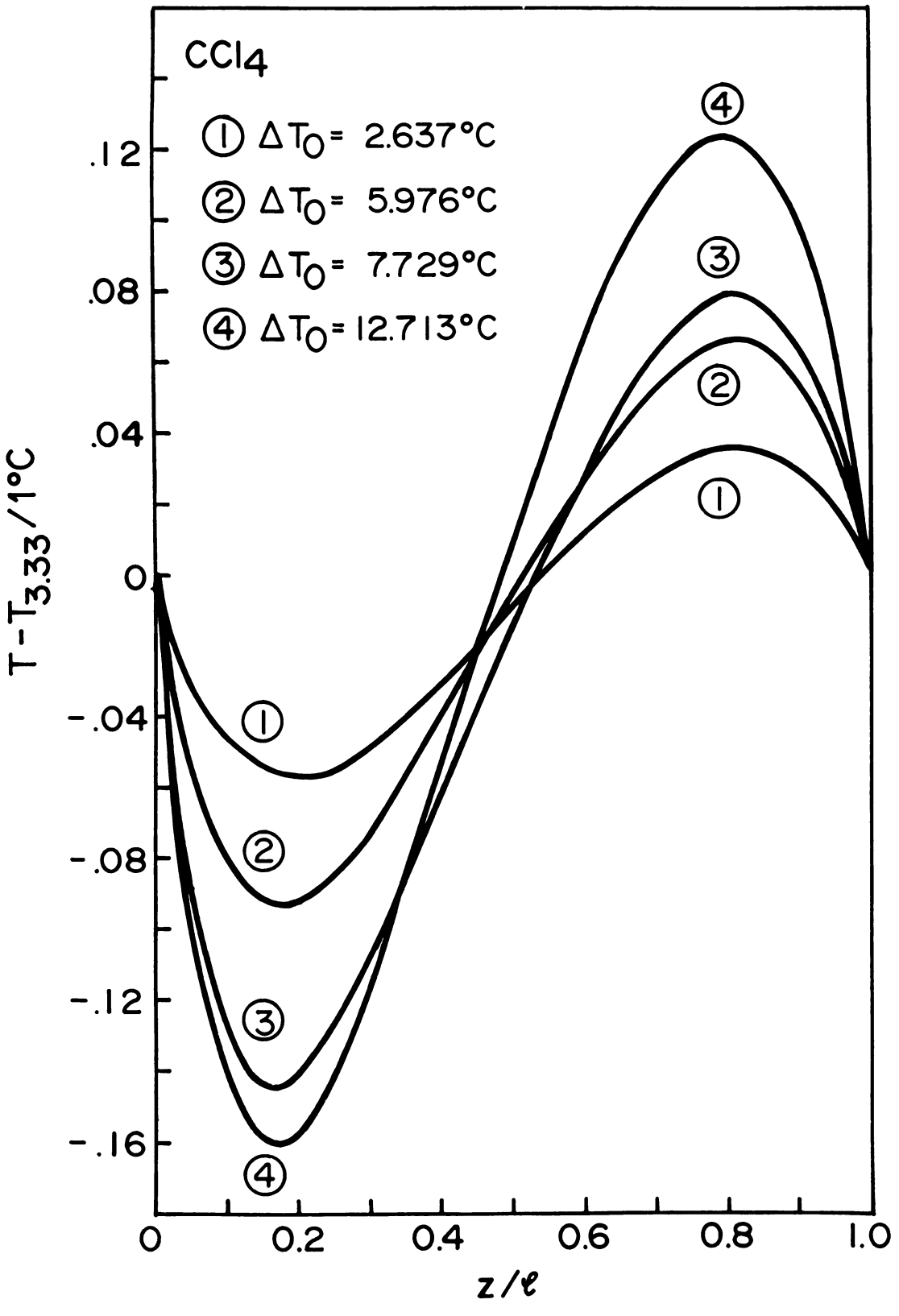
CCl4
① ΔT0 = 2.637°C
② ΔT0 = 5.976°C
③ ΔT0 = 7.729°C
④ ΔT0 = 12.713°C
T-T3.33/1°C
.12
.08
.04
0
-.04
-.08
-.12
-.16
0
0.2
0.4
0.6
0.8
1.0
z/ℓ

(1) regular increase in negative deviation with increasing ΔT_o near the upper plate, (2) regular increase in positive deviation with increasing ΔT_o near the lower plate, and (3) a central region in which the deviation is a linear function of the vertical coordinate. The maximum observed deviations are -0.028^oC at z = 0.243 cm and 0.025^oC at $\underline{l}$-z = 0.236 cm for ethyl acetate($\Delta T_o = 10.019^oC$); -0.107^oC at z = 0.216 cm and 0.079^oC at $\underline{l}$-z = 0.297 cm for benzene($\Delta T_o = 13.063^oC$); -0.160^oC at z = 0.233 cm and 0.124^oC at $\underline{l}$-z = 0.270 cm for carbon tetrachloride($\Delta T_o = 12.713^oC$).

Comparison of ΔT_o and the interferometrically determined difference between the temperature of the liquid at the upper plate and the temperature of the liquid at the lower plate, ΔT, as reported in Table 4.5, reveals discrepancy. ΔT_o is the temperature difference between upper and lower silver plates as measured by thermocouples placed just outside the cell. ΔT_o is consistently smaller than ΔT when Table 4.5 temperature derivatives are used to compute ΔT; however, ΔT_o and ΔT are identical when Table 4.1 temperature derivatives are used. This latter fact is a computational artifact, just as the similarity of $\Delta T_o/\underline{l}$ and $-dT(\underline{l}/2)/dz$(see Table 4.5) is a computational artifact in the former case. Linear least squares analysis shows

$$\Delta T - \Delta T_o = 1.00 \times 10^{-2}\Delta T_o \qquad (4.28)$$

$$\sigma = 0.9 \times 10^{-2}\ ^oC$$

for ethyl acetate;

$$\Delta T - \Delta T_o = 2.43 \times 10^{-2} \Delta T_o \qquad (4.29)$$

$$\sigma = 3.6 \times 10^{-2}\ ^oC$$

for benzene; and for carbon tetrachloride

$$\Delta T - \Delta T_o = 5.67 \times 10^{-2} \Delta T_o \qquad (4.30)$$

$$\sigma = 3.8 \times 10^{-2}\ ^oC$$

where σ is the standard deviation.

The hypothesis that these discrepancies are a true reflection of temperature control and measurement technique is tested by replacing the liquid cell with a white pine block (5.900 cm x 5.876 cm x 1.915 cm). Twenty-two nonisothermal experiments in which ΔT is measured by thermocouples placed at the center of the wood-silver interfaces and ΔT_o is measured by thermocouples placed just outside the wood cell show

$$\Delta T - \Delta T_o = 2.37 \times 10^{-2} \Delta T_o \qquad (4.31)$$

$$\sigma = 1.0 \times 10^{-2}\ ^oC$$

where $-4.7^oC \leqslant \Delta T_o \leqslant 8.1^oC$. ΔT_o is smaller than ΔT. The discrepancy is due to the water flow in upper and lower water jackets which is effectively from a position corresponding to the metal-liquid(or wood) interface center toward the outer edges. Because heat flow is away from the upper plate, the heat bath water cools in flowing toward the outer edges. In addition, heat flow is toward the lower plate; therefore, heat bath water in the lower water jacket heats in flowing toward the outer edges. This results in a measured temperature difference, ΔT_o, which is smaller than the temperature difference ΔT.

The reduced temperature gradient(RTG) is defined as the ratio of temperature gradient to temperature gradient at $z/\underline{l} = 0.5$. Several important features are apparent in the RTG of Figure 4.13. First, no systematic behavior of RTG is found with increasing ΔT_o; this ratio seems to be independent of the applied temperature gradient, ΔT_o. Consequently, RTG's of differing ΔT_o are averaged for each particular liquid. A second characteristic of RTG curves is the exhibited nonlinearity near the solid-liquid interfaces. At the upper interface, the temperature gradient is 4.5% greater than $(dT/dz)_{\underline{1}/2}$ for ethyl acetate, 12.5% greater for benzene, and 30% greater for carbon tetrachloride. These represent extremely large increases in temperature gradient as interfaces are approached. Central regions of RTG curves demonstrate the validity of the Fourier-Laplace description of temperature far from interfaces. Centrally, the temperature gradient is constant. A final characteristic feature of RTG curves is the relative magnitude of temperature gradient increase as the lower plate is approached; the temperature gradient increases as the lower plate is approached, but the magnitude of increase is smaller than that observed as the upper plate is approached. We believe these relative differences to be due to data extrapolation problems, not to physical differences between upper and lower silver plates. At the lower plate a portion of the interferometric light beam has struck and been reflected by the plate;

Figure 4.13

Reduced temperature gradient, $(dT/dz)/(dT/dz)_{\underline{l}/2}$, for ethyl acetate, benzene, and carbon tetrachloride. Corrections have been made for interferometric image distortion. $\underline{l}$ = 1.349 cm.

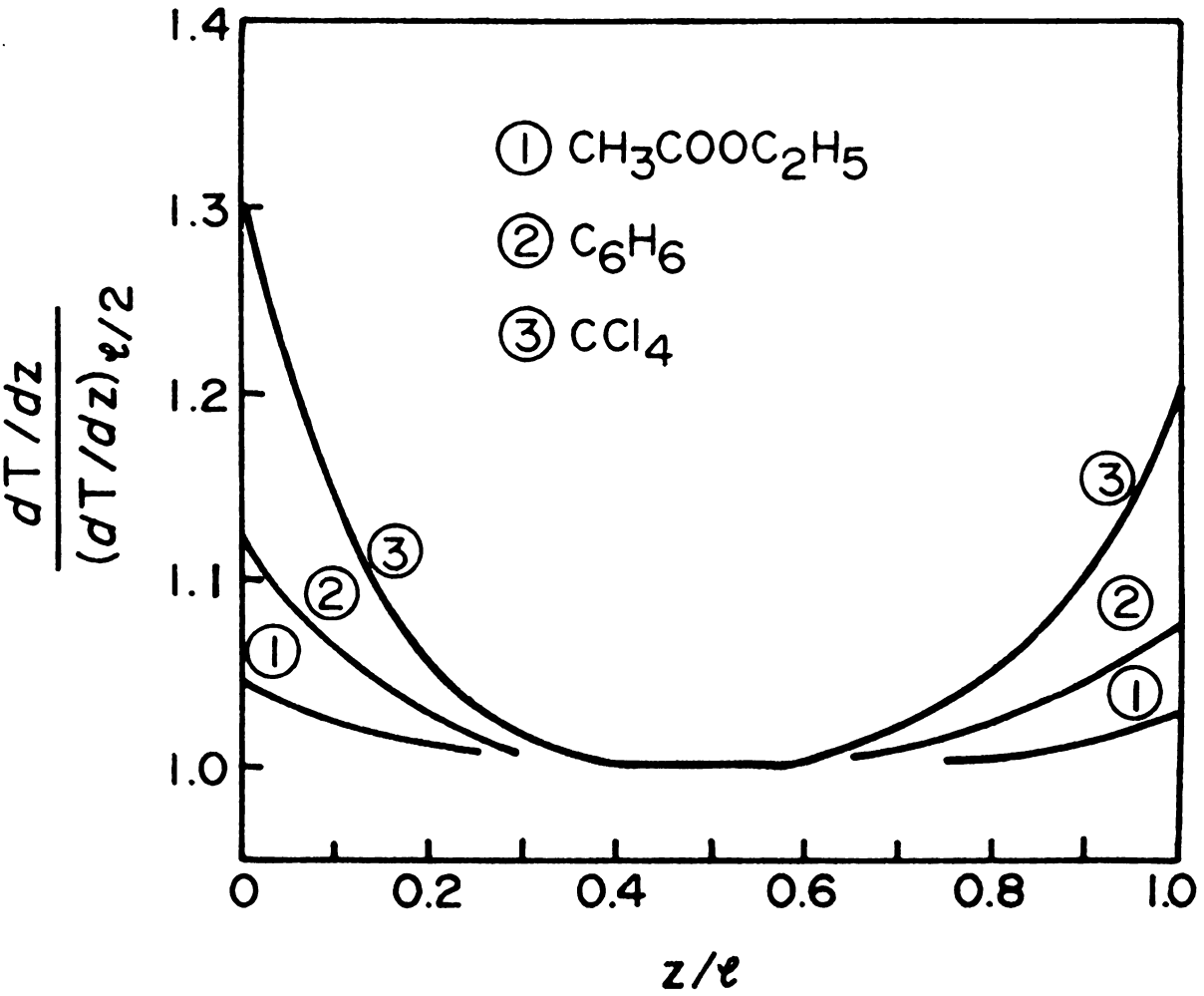
1.4
1.3
1.2
1.1
1.0
0
0.2
0.4
0.6
0.8
1.0
z/ℓ
dT/dz / (dT/dz)ℓ/2
① CH3COOC2H5
② C6H6
③ CCl4

Figure 4.14

Integrated absolute deviation from linearity, $(1/\underline{l}) \int_0^{\underline{l}} |T - T_{3.33}| dz$, as a function of ΔT_o. Corrections have been made for interferometric image distortion. The placement of the water curve is discussed in Section 4.3. $\underline{l}$ = 1.349 cm for ethyl acetate, benzene, and carbon tetrachloride. $\underline{l}$ = 0.474 cm for water.

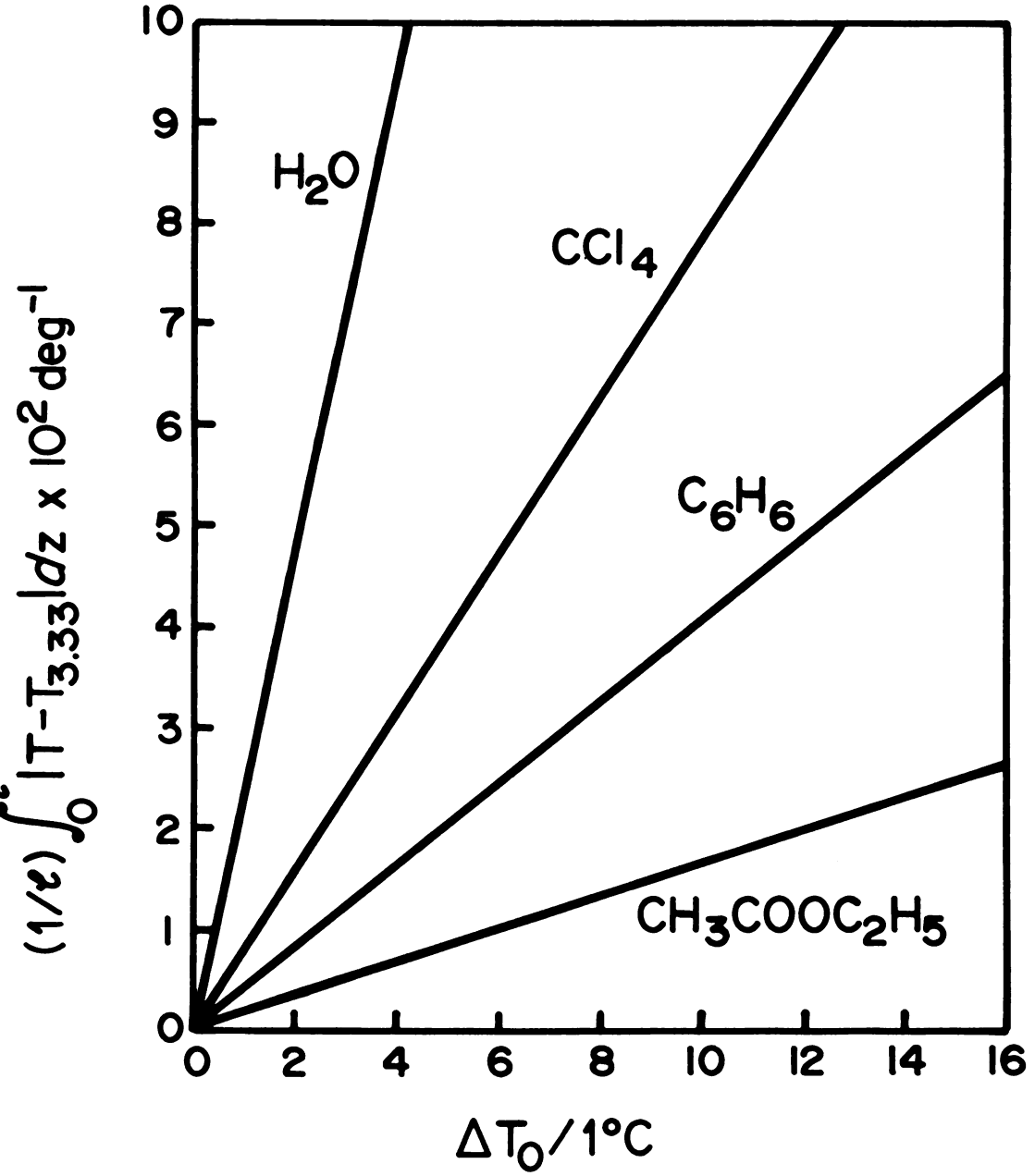
10
9
8
7
6
5
4
3
2
1
0
0
2
4
6
8
10
12
14
16
H2O
CCl4
C6H6
CH3COOC2H5
(1/ℓ) ∫0ℓ |T−T3.33|dz x 10² deg⁻¹
ΔT0/1°C

this portion provides no experimental data. The interval not observed is $\underline{l}-\underline{l}_{eff}$(Equation 4.17). Temperature in this interval is computed by extrapolating the observed fringe shapes of Table 4.4. This procedure underestimates the growth in N(z) as the lower plate is approached and thereby underestimates the growth in temperature gradient. The extent of the unobserved interval can be calculated from the data of Table 4.3 by taking the image height(H) at $\Delta T_o = 0$, subtracting H_{eff} at a particular value of ΔT_o, and dividing by $H/\underline{l}$. For benzene at $\Delta T_o = 13.063^oC$, the unobserved interval extends 0.177 cm from the lower plate. For smaller ΔT_o, the interval is smaller.

Figure 4.14 is another useful representation of the observed nonlinear temperature distributions. The curves are the integrated absolute deviation from linearity. They are functions of ΔT_o, and the magnitude of their first derivatives orders liquids as to the magnitude of exhibited nonlinearity. Where σ is the standard deviation, we find

$$(1/\underline{l}) \int_0^{\underline{l}} |T - T_{3.33}| \, dz = 1.655 \times 10^{-3} \Delta T_o \qquad (4.32)$$

$$\sigma = 1.1 \times 10^{-3} \, ^oC$$

for ethyl acetate,

$$(1/\underline{l}) \int_0^{\underline{l}} |T - T_{3.33}| \, dz = 4.059 \times 10^{-3} \Delta T_o \qquad (4.33)$$

$$\sigma = 3.9 \times 10^{-3} \, ^oC$$

for benzene, and

$$(1/\underline{l}) \int_0^{\underline{l}} |T - T_{3.33}| dz = 7.839 \times 10^{-3} \Delta T_o \qquad (4.34)$$

$$\sigma = 8.8 \times 10^{-3} \ ^oC$$

for carbon tetrachloride. As discussed above, the temperature distribution in water is described by the Fourier-Laplace equation. Thus, neglecting the possibility of temperature jump at the silver-liquid interface, an integrated absolute deviation from linearity of zero is expected for water. Figure 4.14, however, assigns water an entirely unexpected position. This placement is discussed in Section 4.3.

4.3 Temperature Dependence of the Refractive Index of Water

Interferometric determinations of the temperature derivatives of the refractive index of water seem to depend upon whether an isothermal or a nonisothermal experiment is utilized. This is illustrated in Figure 4.15 where

$$\Delta_i = 100((dn/dT)_i - (dn/dT)_{TT})/(dn/dT)_{TT}. \qquad (4.35)$$

$(dn/dT)_i$ is the first derivative of the refractive index with respect to the temperature, as determined by research group i at 1 atmosphere pressure. The absolute refractive index measurements of Tilton and Taylor(TT)[25] are generally considered most reliable and their thirteen parameter equation for $n(\lambda,T)$ is used as a standard of reference. Calculations of $(dn/dT)_i$ in Figure 4.15 are based upon the best linear least square fit of the temperature variation, except for the value reported by Olson and Horne[11] which is for a single temperature only(see Table 4.6). All

Figure 4.15

Per cent deviation of $dn(\lambda,T)/dT$ from values reported by Tilton and Taylor for water at 1 atm. See Equation 4.35. I = isothermal determination, N = nonisothermal determination.

(1) I. Hawkes and Astheimer.[26]

(2) I. Eight wavelengths, Waxler et al.[14,27]

(3) I. Andreasson et al.[28]

(4) I. Dobbins and Peck.[29]

(5) N. Bryngdahl.[30]

(6) N. Olson and Horne.[11]

(7) N. Equation 4.38: Data of this work analyzed with methods of Section 3.5 and $T(0) = T_U$, $T(1) = T_L$ assumption.

(8) N. Equation 4.41: Implied by the ratio of Equation 4.40.

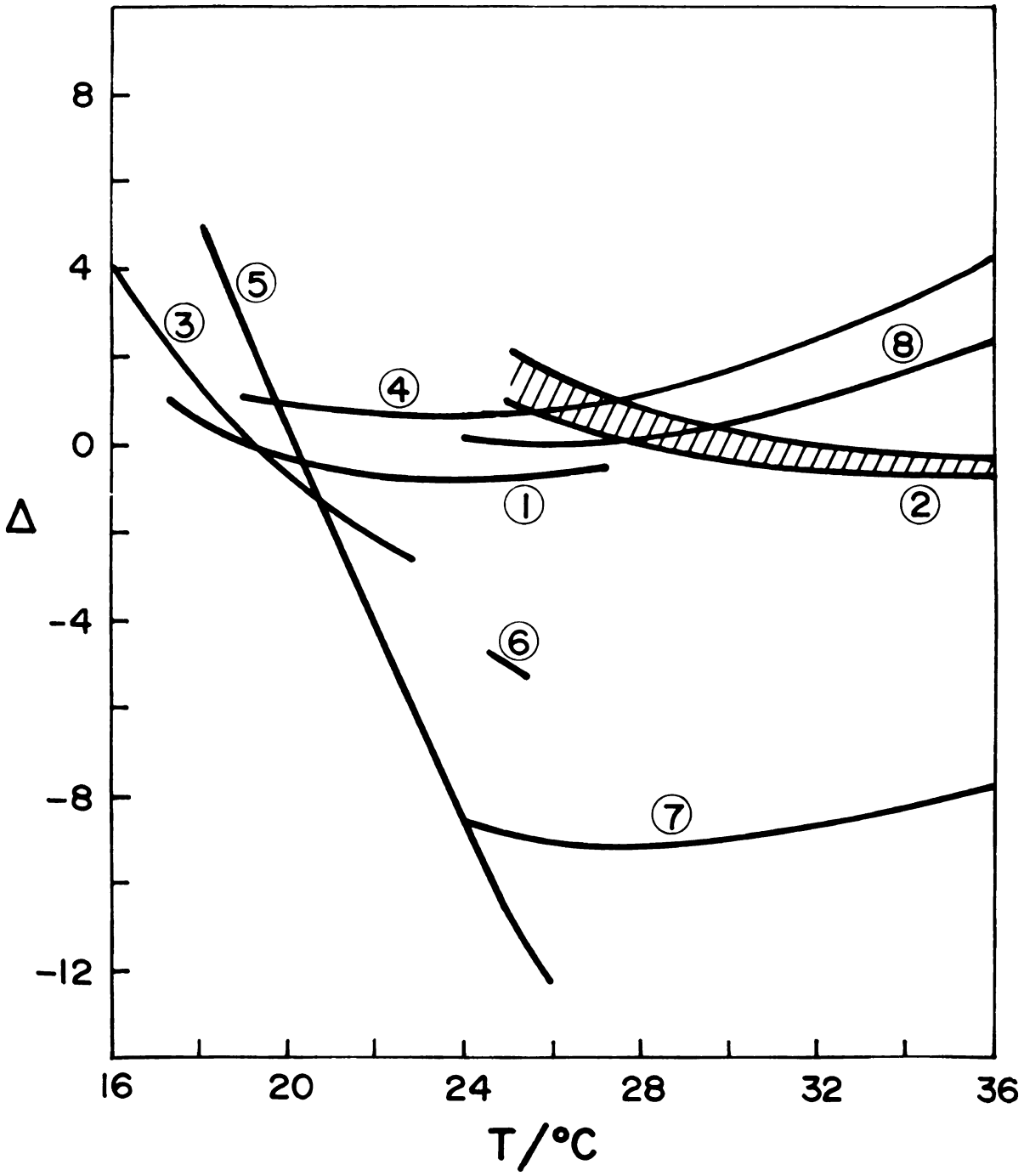
8
4
0
-4
-8
-12
Δ
16
20
24
28
32
36
T/°C
①
②
③
④
⑤
⑥
⑦
⑧

Table 4.6

Temperature dependence of the refractive index of water as determined by isothermal(I) or nonisothermal(N) methods: $-(dn/dT)10^4 \equiv a + bT$, where $c \leq T \leq d$. The parameters a and b are reported in the literature or evaluated with a least squares analysis of reported experimental data at 1 atm. T and λ are in $^{\circ}C$ and nm, respectively. r^2 is interpreted as the proportion of total variation about $-(dn/dT)10^4$ explained by the regression; $0 \leq r^2 \leq 1$. If $r^2 = 1$, the fit is perfect.

Research Group	Method	λ/nm	$a/^{\circ}C^{-1}$	$10^2 b/^{\circ}C^{-2}$	$c/^{\circ}C$	$d/^{\circ}C$	r^2
Hawkes and Astheimer[26]	I	589.3	0.2522	3.158	17	27	0.997
Waxler *et al*[14]	I	643.8	0.4801	2.414	25	54	1.00
Andreasson *et al*[28]	I	632.8	0.3495	2.622	16	23	——
Dobbins and Peck[29]	I	632.8	0.2449	3.220	19	37	——
Bryngdahl[30]	N	546.1	0.7297	0.866	18	26	0.845
Olson and Horne[11]	N	632.8	0.404	2.34	25	25	——

interferometric studies which utilize isothermal states of water[14, 25-29] agree with TT to within 4% in the temperature range for which they are valid. The positive curvature which results in a maximum positive 4% deviation is due to the slight nonlinearity between dn/dT and T which is fully described in the values of TT. However, the two nonisothermal determinations,[11,30] both of which employ Bryngdahl interferometry, markedly differ from the results of TT. It is possible that temperature jumps in the nonisothermal, nonconvecting steady state may contribute to or be the cause of this discrepancy. The hypothesis of the existence of temperature jumps at the metal-water interface is a natural extrapolation of observed nonlinear temperature distributions(Section 4.2) in which the deviation from linearity is negative at the upper interface and positive at the lower interface. However, in the case of temperature jump, the spatial interval of nonlinearity would be smaller than that observable with the Bryngdahl interferometer(less than 0.107 cm for the present apparatus). Such physical phenomena would appear as a temperature jump: the interferometrically measured temperature difference between the liquid at the upper metal-water interface and the liquid at the lower metal-water interface, ΔT, would be less than the measured temperature difference between upper and lower metal plates, ΔT_o, while the observed temperature distribution is linear.

To test this hypothesis we have examined water in the temperature range 24-40°C with the experimental procedure of Section 3.3. The cell height($\underline{l}$) and length (a) are 0.474 cm and 6.771 cm, respectively. The raw data are reported in Table 4.7. The fringe number associated with the vertical coordinate $\underline{l}/2$ times the interfringe distance, δ, has an uncertainty of $\pm$0.003 cm, and the angle of fringe from the vertical, β, has an uncertainty of $\pm$10 min of arc. β is corrected for deviant verticality of the isothermal image by subtracting the tangent of the isothermal angle from the tangent of the nonisothermal. This equals the tangent of the corrected angle. The isothermal angle is typically 10-20 min of arc. The temperature at $z/\underline{l} = 0.5$ is assumed to be given by Equation 3.33 subject to the boundary conditions $T(0) = T_U$ and $T(\underline{l}) = T_L$. First and second derivatives of the refractive index with respect to temperature are mapped from the refined data at $z/\underline{l} = 0.5$ with the methods of Section 3.5. The first derivatives are then fitted by least squares to the best linear temperature equation. The second derivatives are simply averaged and standard deviation calculated. In the evaluation of the regression coefficients a and b for a function such as

$$f(T) = a + bT \tag{4.36}$$

by the method of least squares, the standard error of estimate of f on $T(\sigma)$ is computed along with the standard error of the regression coefficient $a(\sigma_a)$, the standard error of the regression coefficient $b(\sigma_b)$, and the coefficient of

Table 4.7

Nonisothermal experimental water data. $N(\underline{l}/2)$ is the fringe number at image center. β is the angle from vertical of fringe in deg.min and corrected for deviant verticality of the isothermal image. Angles of experiments of identical ΔT_o and T_L have been averaged. The isothermal parameters are $H = 4.713$ cm, $2D = 0.463$ cm, and $\delta = 1.239$ cm with standard deviations of 0.023 cm, 0.018 cm, and 0.018 cm, respectively, for 67 isothermal experiments. $\underline{l} = 0.474$ cm, $a = 6.771$ cm.

ΔT_o/°C	T_L/°C	$N(\underline{l}/2)$	β/deg.min
2.306	23.042	2.232	1.46
2.306	23.042	2.248	1.46
2.667	22.961	2.605	2.29
2.667	22.961	2.588	2.29
3.137	22.818	3.023	3.33
3.137	22.818	3.013	3.33
3.137	22.818	3.021	3.33
3.137	22.818	3.042	3.33
4.199	22.934	4.153	6.10
4.390	22.880	4.310	6.59
5.360	23.026	5.370	10.34
5.360	23.026	5.394	10.34
5.627	23.364	5.761	11.25
5.627	23.364	5.724	11.25
5.695	23.292	5.754	11.00
5.695	23.292	5.792	11.00
6.596	23.340	6.841	14.59
6.596	23.340	6.849	14.59
6.732	23.415	7.020	15.35
3.435	30.393	3.952	3.29
3.214	29.278	3.788	3.41
3.214	29.278	3.754	3.41
3.764	29.152	4.409	4.60
3.764	29.152	4.448	4.60
3.554	29.214	4.121	4.33
4.112	29.142	4.836	5.59
4.112	29.142	4.793	5.59
4.115	29.187	4.880	6.12
4.115	29.187	4.876	6.12
5.091	29.209	6.080	8.57
5.364	29.198	6.415	9.45
5.364	29.198	6.431	9.45
5.195	29.353	6.192	8.59
5.195	29.353	6.180	8.59
5.774	29.377	6.902	11.22

Table 4.7(cont'd.)

ΔT_o/°C	T_L/°C	N($\underline{1}$/2)	β/deg.min
5.774	29.377	6.904	11.22
6.151	29.391	7.387	12.55
6.151	29.391	7.412	12.55
4.365	31.388	5.401	6.34
4.365	31.388	5.372	6.34
4.413	31.525	5.444	6.26
4.413	31.525	5.435	6.26
4.498	31.679	5.685	7.03
4.498	31.679	5.701	7.03
5.597	31.650	7.050	10.39
5.597	31.650	7.055	10.39
4.569	32.424	5.802	7.06
4.569	32.424	5.752	7.06
5.481	32.400	6.967	10.13
5.481	32.400	6.949	10.13
5.726	32.412	7.337	10.33
5.174	30.986	6.393	9.27
5.174	30.986	6.393	9.27
5.604	31.064	6.934	10.27
5.604	31.064	6.935	10.27
5.916	31.069	7.360	11.49
7.781	31.188	9.889	20.06
7.443	31.189	9.450	18.39
6.519	31.292	8.141	14.10
5.750	32.868	7.384	11.18
6.029	32.932	7.788	12.18
6.029	32.932	7.816	12.18
6.315	32.964	8.153	13.54
6.813	33.000	8.875	16.17
6.813	33.000	8.876	16.17
5.805	34.304	7.638	10.12
5.805	34.304	7.688	10.12
5.412	34.738	7.166	9.17
5.023	35.180	6.712	8.37
4.910	35.282	6.540	8.25
4.631	35.566	6.186	7.34
4.116	36.164	5.567	5.48
4.116	36.164	5.507	5.48
4.419	36.310	5.980	6.45
4.987	36.466	6.802	8.28
5.415	36.549	7.402	9.49

determination(r^2). σ, σ_a, σ_b, and r^2 are defined for m experiments by[31,32]

$$\sigma = ((m-2)^{-1}\,\Sigma(f_i - f)^2)^{1/2}, \tag{4.37a}$$

$$\sigma_a = (m^{-1}(\Sigma T_i^2 - m^{-1}(\Sigma T_i)^2)^{-1}\,\Sigma T_i^2)^{1/2}, \tag{4.37b}$$

$$\sigma_b = (\Sigma T_i^2 - m^{-1}(\Sigma T_i)^2)^{-1/2}, \tag{4.37c}$$

and

$$r^2 = (\Sigma f_i T_i - m^{-1}\Sigma f_i \Sigma T_i)^2(\Sigma T_i - m^{-1}(\Sigma T_i)^2)^{-1} \cdot (\Sigma f_i^2 - m^{-1}(\Sigma f_i)^2)^{-1}. \tag{4.37d}$$

The coefficient of determination, r^2, is interpreted as the proportion of total variation of f explained by regression; $0 \leq r^2 \leq 1$. If $r^2 = 1$ the fit is perfect.

The above analytical procedure is illustrated in Figure 4.16. With it, we find

$$-(dn/dT)10^4 = 0.2822 + 0.02671T \tag{4.38}$$

$$\sigma = 0.01614\,^{\circ}C^{-1}$$

$$\sigma_a = 0.01349\,^{\circ}C^{-1}$$

$$\sigma_b = 0.00042\,^{\circ}C^{-2}$$

$$r^2 = 0.983$$

where T is in $^{\circ}C$. The standard error of about 1.5% and the coefficient of determination demonstrate that Equation 4.38 fits the data very well. We also find

$$-(d^2n/dT^2)10^4 = 0.02486\,^{\circ}C^{-2} \tag{4.39}$$

$$\sigma = 0.00098\,^{\circ}C^{-2}.$$

The second derivative of Equation 4.38 is about 7% higher than Equation 4.39. This is a bit large to be explained

Figure 4.16

Temperature dependence of the refractive index. The raw experimental data is refined with the method of Section 3.4, and dn/dT mapped with the method of Section 3.5 assuming that $T(0) = T_U$ and $T(\underline{1}) = T_L$. Equation 4.38(solid line) is the best linear fit of the resulting temperature derivatives.

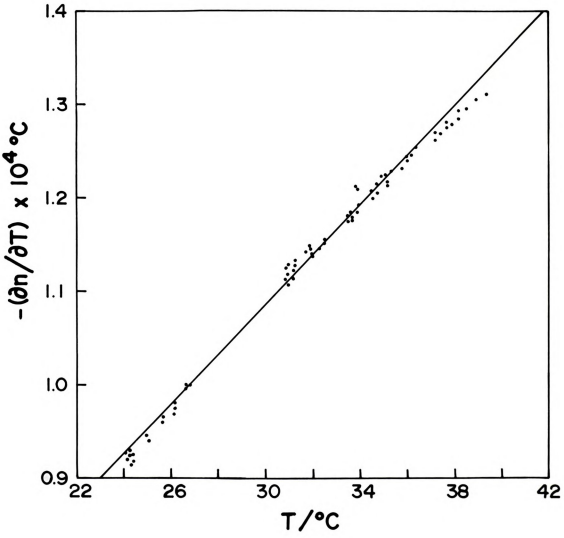
1.4
1.3
1.2
1.1
1.0
0.9
-(∂n/∂T) x 10⁴ °C
22
26
30
34
38
42
T/°C

by the regression coefficients σ_b of Equation 4.38 and σ of Equation 4.39. More disturbing is the discrepancy between Equation 4.38 and the values of Tilton and Taylor; Figure 4.15 shows Equation 4.38 to be 8-9% lower, a magnitude which is much larger than the 1.5% standard error.

Quite another result is found when the experimental first derivatives divided by the square root of the experimental second derivatives are fitted to a linear temperature equation. Then

$$-(dn/dT)10^2/(-d^2n/dT^2)^{1/2} = 1.62619 + 0.17455T \qquad (4.40)$$

$$\sigma = 0.1206$$

$$\sigma_a = 0.1008$$

$$\sigma_b = 0.0031^{\circ}C$$

$$r^2 = 0.977.$$

This analysis is illustrated in Figure 4.17. Equation 4.40 implies that

$$-(dn/dT)10^4 = 0.2838 + 0.03047T \qquad (4.41)$$

where the estimated uncertainty in the calculated value of the derivative is 2%. Figure 4.15 shows Equation 4.41 to be in very good agreement with Tilton and Taylor.

The failure of Equation 4.38 to agree with isothermal determinations of dn/dT in the experimental temperature range and the success of Equation 4.41 can be qualitatively discussed by neglecting both the bending of light in temperature gradients and small temperature

Figure 4.17

$f(T) = -(dn/dT)10^2/(-d^2n/dT^2)^{1/2}$. The data are computed by refining the raw data with the method of Section 3.4, and mapping dn/dT and d^2n/dT^2 with the method of Section 3.5 assuming that $T(0) = T_U$ and $T(\underline{1}) = T_L$. Equation 4.40(solid line) is the best linear fit of the above ratio. The dashed line is predicted by Equation 4.38.

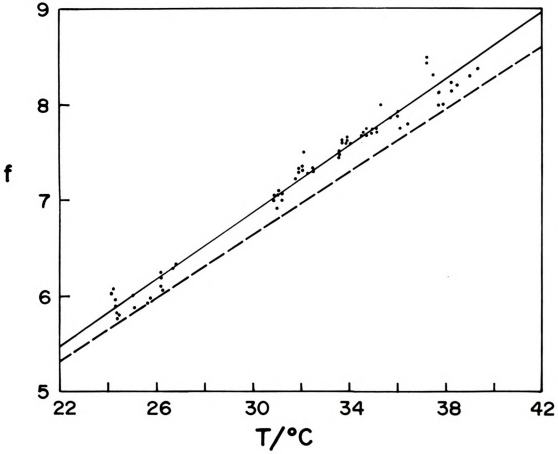
9
8
7
6
5
f
22
26
30
34
38
42
T/°C

dependence of the thermal conductivity. Then Equations 3.6 and 3.28 yield two important equations for media which exhibit straight line fringe patterns in the nonisothermal state. The first equation is

$$-dn/dT = D_1 N/\Delta T \tag{4.42}$$

where dn/dT is the refractive index temperature derivative of the cell center, N is the number of fringes which evolve at the image coordinate corresponding to cell center, ΔT is the temperature difference between liquid at upper and lower interfaces, and D_1 is a constant determined from the isothermal configuration cell image. The second equation of importance is

$$-d^2n/dT^2 = D_1 D_2 \tan\beta /(\Delta T)^2 \tag{4.43}$$

where d^2n/dT^2 is second derivative at cell center, β is the fringe angle from the vertical in the nonisothermal, steady state configuration, and D_2 is a constant determined from the isothermal configuration cell image. The difficulty with Equation 4.42 and 4.43 is ΔT. ΔT is a quantity which is not directly measured in the present experimental arrangement. Assumptions regarding ΔT may lead to erroneous results. For example, suppose that

$$\Delta T = \Delta T_o = T_U - T_L. \tag{4.44}$$

In this case all quantities in Equations 4.42 and 4.43 are experimentally determined and the desired derivatives can be calculated. Equation 4.44 is assumed by Bryngdahl,[30] Olson and Horne,[11] and in the data analysis of this work

which culminates in Equation 4.38 and 4.39. Suppose, however, that water exhibits a temperature jump. In such a case ΔT will be less than ΔT_o and use of ΔT_o will yield computed derivatives which are smaller than the true derivatives. This is the trend of Bryngdahl's refractive index temperature derivatives above 20^oC(see Figure 4.15), of Olson and Horne's at 25^oC, and of Equation 4.38 between 24^oC and 40^oC. Fortunately, it is possible to avoid the ΔT problem by eliminating ΔT from Equations 4.42 and 4.43. This yields

$$-(dn/dT)/(-d^2n/dT^2)^{1/2} = (D_1/D_2)^{1/2}N/(\tan\beta)^{1/2}. \quad (4.45)$$

Because the evaluation of dn/dT via Equation 4.45 does not involve ΔT, results should agree wtih isothermal determinations. This explains the success of Equation 4.40.

It may be that the temperature measurement technique, not a temperature jump, is responsible for the discrepancy between Equation 4.38 and 4.41; however, the "wood cell" experiments described in Section 4.2 strongly indicate that the technique is slightly compensating and not creating an apparent temperature jump. Further, the variance between Equation 4.38, Bryngdahl, and Olson and Horne is expected because the magnitude of any temperature jump will depend upon the interactions between the solid boundaries and the liquid. This interaction is a function of composition, structure, and condition of the solid surface.

The functional dependence of ΔT upon ΔT_o can be estimated with Equation 4.42. Substituting Equation 4.38 for D_1N and Equation 4.41 for dn/dT, we find

$$T = 0.994((1 + 0.0947T)/(1 + 0.1074T))\Delta T_o \qquad (4.46)$$

where $24^oC \leq T \leq 40^oC$, $2^oC \leq \Delta T_o \leq 8^oC$. Averaging this relationship over the applicable temperature range, yields

$$\Delta T - \Delta T_o = -9.671 \times 10^{-2}\Delta T_o. \qquad (4.47)$$

Further, since

$$T - T_{3.33} = (\Delta T - \Delta T_o)(\tfrac{1}{2} - z/\underline{1}), \qquad (4.48)$$

the integrated absolute deviation is

$$(1/\underline{1}) \int_0^{\underline{1}} |T - T_{3.33}| dz = 2.414 \times 10^{-2}\Delta T_o. \qquad (4.49)$$

Figure 4.14 illustrates that

$$H_2O > CCl_4 > C_6H_6 > CH_3COOC_2H_5 \qquad (4.50)$$

is the observed liquid order for integrated absolute deviation.

The physical literature contains several reports of unexplained water density fluctuation in the neighborhood of 35^oC. Hawkes and Astheimer[26,33] have encountered small, time-dependent fringe wiggle during isothermal Jamin interferometric studies of the refractive index of water. These wiggles correspond to density fluctuation of $\Delta\rho/\rho = 6 \times 10^{-6}$ and appear in the 34^oC to 45^oC interval. Varying the temperature during 3062 isothermal Michelson interferometric evaluations of the refractive index of water,

Dobbins and Peck[29] found no evidence of any abrupt, large refractive index change. Possible irregularity is, however, indicated in their plot of mean deviation of the experimental refractive index versus temperature. The plot reveals rapid change at 34.5°C. Andaloro et al[34] report a subtle transition in water between 30°C and 40°C. Their study of the weakly absorbed 1.2 u combination band of water yields Arrhenius plots of integrated component intensity ratios which show neatly defined breaks occurring in the 30°C to 40°C temperature interval. Outside this interval, the experimental points are well aligned. The Bryngdahl interferometric fringe pattern of this work does not directly indicate the presence of this anomalous phenomena. Yet, the increased deviation in the ratio of $(dn/dT)/(d^2n/dT^2)^{1/2}$ above 35°C, shown in Figure 4.17, is further indirect evidence of its existence.

4.4 Discussion

New computations, experimental observations, and experimental deficiencies have been reported. First, computed nonisothermal image heights have been confirmed experimentally, proving the validity of data analysis with respect to the experimental procedures. To our knowledge, this is the first time that the essential correctness of the mathematical analysis of nonisothermal data has been experimentally proven, not simply assumed. Characteristic fringe patterns for laminar and turbulent flows, driven by

end effects, have also been observed. This is important because absence of these characteristic patterns implies absence of convective liquid flow. Thus, convective flow does not contribute or cause the observed nonlinear temperature distributions. Corrections, however, are found to be necessary for nonisothermal image distortion which results from lens aberrations. Finally, the thermocouple measurement ΔT_o has proven to be an imperfect representation of ΔT. This demonstrates the need for improved temperature control and measurement. Both image distortion and temperature control problems must be considered in future nonisothermal, cell system and optical train design.

After consideration of the above nonisothermal experimental problems, the temperature distribution predicted by the Fourier-Laplace temperature equation for a nonconvecting liquid is found to fail near the silver-liquid interface for ethyl acetate, benzene, and carbon tetrachloride. The observed nonlinear temperature distributions are reported in three forms: (1) temperature deviation form linearity(Figures 4.10-4.12), (2) reduced temperature gradient(RTG, Figure 4.13), and (3) integrated absolute deviation form linearity(Figure 4.14). Each form has an advantage. The temperature deviation from linearity curves directly demonstrate the magnitude of the temperature deviation from that predicted by the Fourier-Laplace equation. They are functions of both applied temperature gradient and

vertical coordinate. RTG curves indicate that the temperature gradient divided by the temperature gradient at cell center is independent of applied temperature gradient within experimental uncertainty. Furthermore, RTG curves reveal dramatic increases in temperature gradient as the metal-liquid interface is approached. The magnitude of the increase is liquid dependent and found to be 4.5% for ethyl acetate, 12.5% for benzene, and 30% for carbon tetrachloride when the metal is highly polished silver. Curves of integrated absolute deviation from linearity (functions of the applied temperature gradient) conveniently order liquids according to the relative magnitude of their exhibited deviation from linearity. A nonzero curve is associated with liquids which exhibit temperature jumps at the metal-liquid interface. Observed nonlinear temperature distributions are found to extend 0.2-0.3 cm from the interface for ethyl acetate, benzene, and carbon tetrachloride. Evidence strongly suggests that water exhibits a temperature jump.

Knowledge of liquid nonlinear temperature distributions makes possible an increase in the accuracy of experimentally determined Soret coefficients,

$$\alpha = (-T/C_1C_2)(dC_1/dz)/(dT/dz), \qquad (4.51)$$

nonisothermally determined refractive index temperature derivatives,

$$dn/dT = (dn/dz)/(dT/dz), \qquad (4.52)$$

and interior conducibilities,

$$k = -J_z/(dT/dz). \qquad (4.53)$$

Because nonlinear temperature distributions associated with interface effects have temperature gradients smaller than $\Delta T/\underline{l}$ at cell center, use of the common gradient approximation

$$dT(\underline{l}/2)/dz \simeq -\Delta T/\underline{l}$$

in Equation 4.51-4.53 yields computed values of α, dn/dT, and k which are lower than the true liquid properties. Table 4.5 shows that the linear assumption yields a 1% systematic error for ethyl acetate, a 3% error for benzene, and a 6% error for carbon tetrachloride. Figure 4.15 suggests an 8% error for water. Errors of this magnitude are much larger than typical experimental inaccuracy of 1-2% reported by independent research groups for both temperature derivatives of refractive indices and thermal conductivities of carbon tetrachloride, benzene, and water.[19]

The nonisothermal, Bryngdahl interferometric image also provides criteria for the establishment of liquid thermal conductivity standards. Any liquid which exhibits both linear fringe pattern and absence of a temperature jump problem similar to that observed for water will be an excellent standard. The temperature distribution in such a liquid is independent of cell size and boundary material, making the thermal conductivity measurements laboratory independent and highly reproducible.

Nonlinear temperature distributions may prove very useful in testing the validity of radiation energy transport

models for the liquid phase. Taking the viewpoint that Fourier's interior conducibility incorporates all energy transport processes characteristic of the liquid far from walls, the time-independent, nonconvecting temperature equation becomes

$$(d/dz)k(dT/dz) = -\sigma \qquad (4.54)$$

where k is the interior conducibility. $\sigma(z)$ is the energy source term. It contains (1) all energy transport processes occurring within the liquid but not described by the interior conducibility and (2) all energy transport processes described by the interior conducibility but not occurring within the liquid. To conceptualize and understand, consider the averaged photon events of Figure 4.18. Photon events far from walls are depicted in Figure 4.18A. When molecule 1 emits a photon and molecule 2 absorbs that photon, the horizontal layer of molecule 2 is heated because the horizontal layer of molecule 1 has higher temperature. Likewise, the emission and absorption of a photon between molecules 3 and 4 is also a photon energy transport event. All such events are described by the interior conducibility.(Other energy tansport processes contained within the interior conducibility include vibration-vibration, translation-translation, vibration-translation, and vibration-rotation energy transfer during molecular collisions.) Placement of a perfect mirror between molecules 1 and 3 alters the energy transport processes. The photon emitted by molecule 1 is now

Figure 4.18

(A) Molecule 1 emits an "average" photon which is absorbed by molecule 2. This energy transport process heats the horizontal layer of molecule 2 because the photon originates within a layer of higher temperature.

(B) Placement of a perfect mirror between molecules 1 and 3 alters photon energy transport processes. The photon absorbed by molecule 2 now originates from molecule 3. Since the horizontal layer of molecule 3 is of lower temperature than the layer of molecule 1, energy flux differs from the above figure. See text.

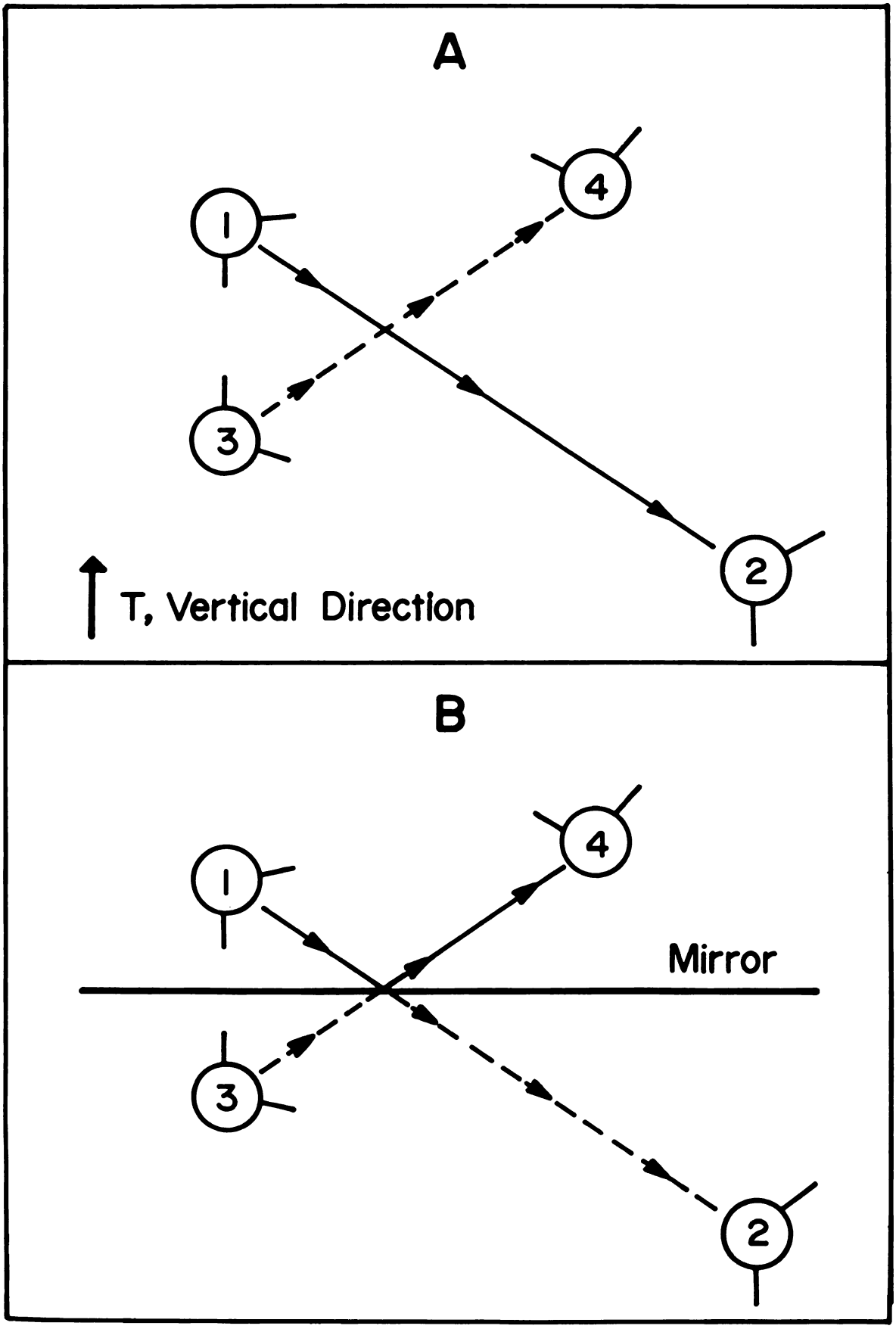
A
1
2
3
4
T, Vertical Direction
B
1
2
3
4
Mirror

reflected and abosrbed by molecule 4. But, Fourier's heat flux law, ignorant of the mirror's presence, says that the photon absorbed by molecule 4 originates from molecule 3 whose horizontal layer is lower in temperature than that of molecule 1. The actual photon absorbed has more energy on the average. Consequently, positive deviation from linearity is found near the lower wall. Similarly, Fourier's heat flux law says that the photon absorbed by molecule 2 originates from molecule 1. This is wrong. Because of the mirror's presence, the photon has originated from molecule 3 whose horizontal layer is lower in energy. This results in negative deviation from the temperature predicted by the Fourier-Laplace temperature equation near the upper wall. By these arguments the extent of the nonlinearity from the liquid-metal interface is roughly the inverse Lambert absorption coefficient of the lowest energy vibrational mode. For water this is 7×10^{-4} cm ($\tilde{\nu} = 200\ cm^{-1}$);[35] for carbon tetrachloride it is 0.13 cm ($\tilde{\nu} = 320\ cm^{-1}$).[8]

The simplest mathematical model for the energy source term: (1) assumes temperature nonlinearity is due solely to photon events, (2) treats the metal boundary as a non-emitting, non-absorbing, perfect mirror, (3) forbids multiple reflection, and (4) treats the liquid as a non-photon-scattering, isotropic media. Summing all reflection associated emission-absorption events per unit time and subtracting all emission-absorption events which due to

the presence of walls cannot occur yields the energy source. We find

$$\sigma(z) = \int_0^\infty \sigma(z,\upsilon)d\upsilon \tag{4.55}$$

where

$$\begin{aligned}\sigma(z,\upsilon)/2\pi a(\upsilon) = &\int_0^{\underline{1}} dz_1 \int_{-1}^{0} du B(z_1,\upsilon)e^{(a(\upsilon)/u)(z_1+z)} \\ &-\int_{-\infty}^{0} dz_1 \int_0^1 du B(z_1,\upsilon)e^{(a(\upsilon)/u)(z-z_1)} \\ &+\int_0^{\underline{1}} dz_1 \int_0^1 du B(z_1,\upsilon)e^{-(a(\upsilon)/u)((\underline{1}-z_1)+(\underline{1}-z))} \\ &-\int_{\underline{1}}^{\infty} dz_1 \int_{-1}^{0} du B(z_1,\upsilon)e^{(a(\upsilon)/u)(z_1-z)},\end{aligned} \tag{4.56}$$

$$u = \cos\phi, \tag{4.57}$$

$$a(\upsilon) = a(z,\upsilon) = \alpha(z,\upsilon)(1 - e^{-\theta}), \tag{4.58}$$

$$\theta = h\upsilon/kT, \tag{4.59}$$

$$\begin{aligned}B(z,\upsilon) &= B(T(z),\upsilon) \\ &= (2h\upsilon^3/c^2)/(e^\theta - 1).\end{aligned} \tag{4.60}$$

υ, ϕ, h, k, c, and $B(T,\upsilon)$ are the photon frequency, vertical angle, Planck's constant, Boltzmann's constant, speed of light, and black body radiation intensity, respectively. $\alpha(z,\upsilon)$ is the Lambert absorption coefficient at the temperature T(z). More complicating features may be built into the model. These include emission and absorption of photons by the metal boundaries, spectral reflection, and photon scattering by the liquid media. Once a particular model has been shown to accurately predict the observed

nonlinear temperature distributions, the model is proven. Liquid radiation events may then be substracted from the interior conducibility, leaving all energy transport due to non-radiation processes. This will be an unambiguous liquid property which may be called the thermal conductivity.

Many review papers exist dealing with the counting of photon events in gaseous atmospheres,[36-41] liquids,[4,5] and solids.[42] The work of Pomraning[43,44] may prove particularly useful in pursuing the above program.

CHAPTER 5

NONISOTHERMAL, CONVECTING LIQUID STATES

5.1 Introduction

As temperature increases, liquid density decreases. Consequently, when a horizontal parallel plate apparatus is heated from below, the liquid density decreases as the lower plate is approached. This results in a liquid layer which is unstable to convective motion, provided the resulting buoyant force exceeds the viscous dissipation force. The transition from nonconvection to convection as the buoyant force is increased is generally called "Bénard convection" in recognition of Bénard's[1] 1901 observations of hexagonal convection cells in very thin liquid layers with a free surface. However, it is now generally believed that surface tension effects played an important role in Bénard's experiments.[2-4] In this chapter and the relevant references, the layers are relatively deep and confined within rigid boundaries. Thus, surface tension plays no role. The transition is also called the "Rayleigh-Jeffreys instability" in recognition of their theoretical contributions.

The important parameter describing the relative magnitude of buoyant and viscous force is the dimensionless

Rayleigh number defined by

$$R = -g\alpha\rho^2\tilde{C}_V l^3 \Delta T/k\eta, \tag{5.1}$$

where ρ, $\tilde{C}_V$, k, and η are the mass density, specific heat, thermal conductivity, and viscosity, respectively. g is the gravitational constant(980.2 cm sec^{-2}) and α is the coefficient of expansion. When heating from below, ΔT is negative and R is positive. Linear stability analysis of the hydrodynamic equations describing $\rho(\underset{\sim}{r},t)$, $T(\underset{\sim}{r},t)$, and the barycentric velocity, $v(\underset{\sim}{r},t)$, show that in the Boussinesq approximation a transition from nonconvection to time-independent convection occurs at the Rayleigh number

$$R_I = 1707.76 \tag{5.2}$$

for a fluid between rigid boundaries. This theoretical result has been reviewed by Chandrasekhar.[5] For $R < R_I$, the fluid is at rest and energy is transported by conduction alone; for $R > R_I$, steady state convection of the fluid contributes to energy transport.

It has been found experimentally that several additional transitions occur with increasing Rayleigh number.[6-12] These are: (a) a two-dimensional steady flow to three-dimensional steady flow transition at R_{II}, (b) a three-dimensional steady flow to three-dimensional time-dependent flow transition at R_{III}, (c) a time-dependent flow to time-dependent flow of increased frequency transition at R_{IV}, and (d) a time-dependent flow to turbulent flow

transition at R_V. Krishnamurti[10,11] has compiled evidence of these transitions and has shown that the transitions are dependent upon the dimensionless Prandtl number defined by

$$Pr = \eta \tilde{C}_V / k. \tag{5.3}$$

This is a ratio of viscous energy dissipation to thermal conductivity. Generally, the critical Rayleigh numbers increase toward a limiting value with increasing Prandtl number.

Detailed reviews of the Benard problem are available.[5,13-18] Works which relate the concepts and mathematics of the Benard instability with the Taylor problem, the Landau phase transition, lasing, and oscillating chemical reactions are also available.[19-21]

In this chapter we explore the application of Bryngdahl interferometry to the analysis of the Rayleigh instabilities. Consequently, the thrust of the chapter is experimental. All measured quantities are compared with relevant experimental studies which have been reported in the literature. Questions include: What transitions can be observed with the Bryngdahl interferometer? What temperature distributions are observed between transitions? Do time-periodic states exist in the fluid? If so, what is the period? Are aperiodic states a possibility? If so, for what Rayleigh numbers and what is the observed frequency spectrum? To answer these questions, we have studied water with the experimental techniques and data analysis described in Chapter 3 but with an experimental arrangement in which

$$\Delta T_o = T_U - T_L < 0. \tag{5.4}$$

The cell used has a height, $\underline{l}$, of 1.440 cm and measures 5.961 cm along the optical path. It is 7.0 cm wide. The mean temperatues, T_M, of individual experiments varies between 22.3°C and 32.0°C. ΔT_o values vary between -0.02°C and -12.4°C. Furthermore, using the density, coefficient of expansion, coefficient of compressibility, and heat capacity compilation of Kell,[22] the thermal conductivity evaluation of McLaughlin,[23] and viscosity reported in the Handbook of Chemistry and Physics,[24] we find that for water

$$-(R/\underline{l}^3\Delta T)10^{-4}\ \text{cm}^3\ ^\circ\text{C} = -9.6914 \times 10^{-1} + 1.7429 \times 10^{-1}T - 5.3120 \times 10^{-3}T^2 + 1.5528 \times 10^{-4}T^3 - 1.4803 \times 10^{-6}T^4, \tag{5.5}$$

and

$$Pr = 13.044 - 4.4926 \times 10^{-1}T + 9.1933 \times 10^{-3}T^2 - 1.1055 \times 10^{-4}T^3 + 5.9166 \times 10^{-7}T^4. \tag{5.6}$$

T is in °C, $20^\circ\text{C} \leq T \leq 35^\circ\text{C}$, and P = 1 atm.

5.2 Temperature Distributions and the First Rayleigh Transition

Figure 5.1 reproduces the nonisothermal Bryngdahl images of thirty-two experiments in the order of increasing Rayleigh number. It is apparent that even at the lowest Rayleigh number(9.3×10^3) the fringe pattern is essentially vertical but with curvature near the upper and lower boundaries characteristic of nonlinear temperature distribution. Vertical fringe patterns of negligible shift are characteristic of isothermal regions. Up to $R = 2.9 \times 10^4$ the curvature increases gradually, and comparison of Figure 5.1 with Figure 4.3 shows that time-independent fluid flow is the predominant mode of energy transport. The straight, tilted fringe characteristic of pure thermal conduction of energy is absent.

Between $R = 2.9 \times 10^4$ and 3.3×10^4, the time-independent boundary layers become well-formed and distinctly contrast the central isothermal region in which $dT/dz = 0$. The boundary layers extend approximately $0.2\underline{l}$ into the fluid. The isothermal region is $0.6\underline{l}$ in extent. The thermal boundary layers grow in strength with increasing Rayleigh number. However, at $R = 5.40 \times 10^4$ a photomultiplier at image center indicates the appearance of small amplitude, time-dependent fluctuations which are superimposed upon the time-independent pattern. The amplitude of the fluctuations grow with increasing Rayleigh number and are visually recognized in the image at $R = 8.4 \times 10^4$. Finally, between

Figure 5.1

Nonisothermal Bryngdahl cell images. $\underline{l}$ = 1.440 cm, a = 5.961 cm, H = 3.175 cm, 2D = 0.138 cm, δ = 0.353 cm. Equation 4.47 is used to evaluate ΔT for given ΔT_o.

Exp.	$10^{-4}R(T_M,\Delta T)$	Pr	Exp.	$10^{-4}R(T_M,\Delta T)$	Pr
1	0.929	6.30	17	7.670	6.14
2	1.433	6.28	18	8.366	6.14
3	1.796	6.27	19	9.224	6.13
4	1.998	6.28	20	9.822	6.11
5	2.268	6.28	21	10.49	6.11
6	2.577	6.27	22	11.18	6.10
7	2.888	6.27	23	12.00	6.10
8	3.321	6.26	24	12.74	6.08
9	3.808	6.25	25	13.73	6.07
10	4.136	6.25	26	14.20	6.06
11	4.426	6.24	27	21.41	6.53
12	4.859	6.24	28	30.56	6.34
13	5.365	6.20	29	37.08	6.22
14	5.700	6.19	30	43.43	6.10
15	6.377	6.17	31	57.44	5.90
16	7.347	6.15	32	72.15	5.72

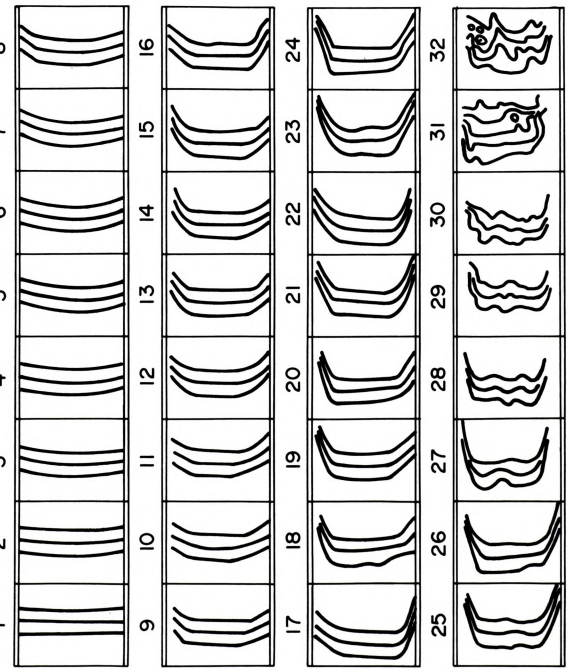
1
2
3
4
5
6
7
8
9
10
11
12
13
14
15
16
17
18
19
20
21
22
23
24
25
26
27
28
29
30
31
32
0
t
z

$R = 5.7 \times 10^5$ and 7.2×10^5 the fluctuations become so strong as to destroy the characteristic fringe pattern of isothermal layers and boundary layers. A transition to turbulence is evident.

The temperature distributions of Figure 5.2 are mapped from the refined data using the method of Section 3.6. They are considered to be the average temperature experienced by a photon pencil along the optical path. The thermal boundary layers and isothermal region discussed above are quantitiatively displayed in this figure.

An important aspect is the absence of "temperature inversion" in the domain $0.2 < z/\underline{l} < 0.8$. In their evaluation of horizontally averaged temperature distributions, Deardorff and Willis[7] have used a resistance wire probe to measure temperature gradient. They report distributions at $R = 6.3 \times 10^5$, 2.5×10^6, and 1.0×10^7 which qualitatively agree with Figure 5.2 However, Gille's[8] measurement of the horizontally averaged temperature distribution with a Michelson interferometer at $R = 2.73 \times 10^4$ reveals temperature inversion in the central region. The reversal is about 1.5% of the impressed temperature difference. Finally, the Mach-Zehnder interferometrically determined temperature profiles of Farhadieh and Tankin[12] provide direct evidence of a 6% temperature inversion at $R = 1.57 \times 10^4$ and 2.36×10^4. This result verifies numerical computations at high Rayleigh numbers of Veronis.[25] We believe that the inversion has not been observed with the Bryngdahl interfer-

Figure 5.2

Temperature distributions for various impressed temperature gradient.

$-\Delta T_o/1^oC$	$10^{-4}R(T_M,\Delta T)$
0.299	1.43
0.417	2.00
0.689	3.32
0.854	4.14
1.000	4.86

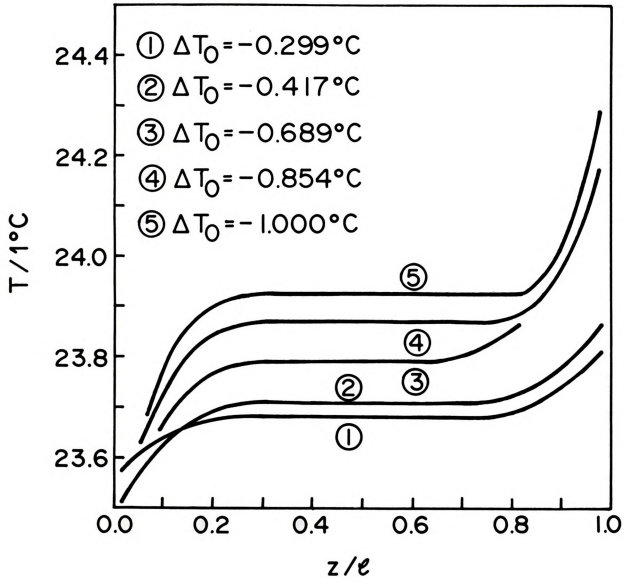
① ΔT0 = −0.299°C
② ΔT0 = −0.417°C
③ ΔT0 = −0.689°C
④ ΔT0 = −0.854°C
⑤ ΔT0 = −1.000°C
T/1°C
24.4
24.2
24.0
23.8
23.6
0.0
0.2
0.4
0.6
0.8
1.0
z/ℓ

ometer because of the very small total fringe shift at image center caused by such small temperature gradients. At $R \sim 2 \times 10^4$ a 6% inversion results in a total fringe shift of only 0.01 cm for the optical train used in this series of experiments. Furthermore, the expected fringe shift at larger Rayleigh numbers are masked by time-dependent fringe fluctuation. These observations indicate that the direct temperature measurement techniques provided by Michelson and Mach-Zehnder interferometry are to be preferred in the analysis of very small temperature phenomena for which temperature gradients are nearly constant.

Figure 5.3 compares the experimentally found temperature derivatives at $z = \underline{1}$ with the values expected for pure conduction. The experimental gradients are far larger. In addition, the sudden increase in the standard deviation at $R(T_M,\Delta T_o) = 3.7 \times 10^4$ indicates a transition to time-dependent flow. This is the critical Rayleigh number R_{III} within an uncertainty of $\pm$12%. With the correction of Equation 4.47 we find

$$R_{III}(T_M,\Delta T) = 3.3 \times 10^4 \pm 12\%. \qquad (5.7)$$

This agrees well with Krishnamurti's[11] value of $3.59 \times 10^4 \pm 15\%$. However, Schmidt and Saunders[27] report a transition from laminar to turbulent flow at $R \sim 4.7 \times 10^4$ while Malkus[6] claims that this transition occurs between 1×10^4 and 3×10^4.

Figure 5.3

Experimentally determined boundary($z = \underline{1}$) temperature gradient as a function of Rayleigh number. Curve 1 is the linear least squares analysis of data(Equation 5.8); Curve 2 is the prediction of the Laplace equation description of temperature.

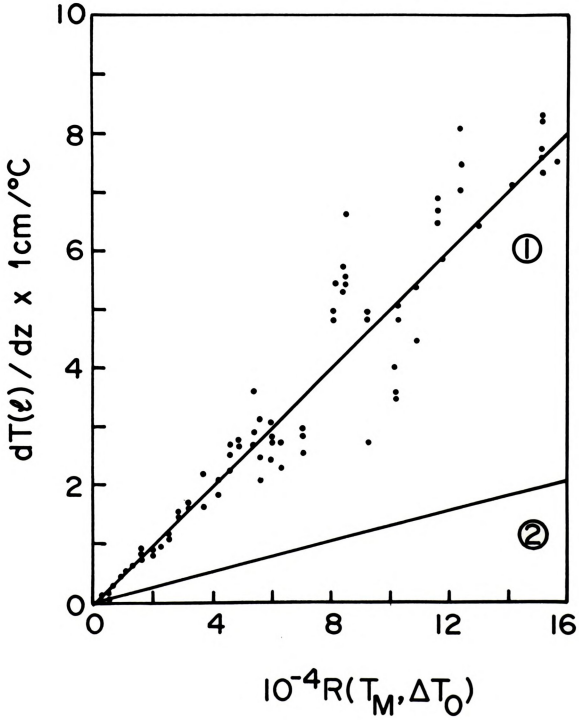
10
8
6
4
2
0
0
4
8
12
16
dT(ℓ) / dz x 1cm/°C
10^-4 R(T_M, ΔT_0)
①
②

Linear least squares analysis of the data $R(T_M,\Delta T_o) \leq 4.2 \times 10^4$ yields

$$dT(\underline{1})/dz = -7.177 \times 10^{-2} + 5.075 \times 10^{-5} R(T_M,\Delta T_o) \quad (5.8)$$

$$\sigma = 0.133$$

$$\sigma_a = 4.42 \times 10^{-2}$$

$$\sigma_b = 1.94 \times 10^{-6}$$

$$r^2 = 0.957.$$

The gradient expected for pure thermal conduction is

$$\begin{aligned} dT(\underline{1})/dz &= -\Delta T_o/\underline{1} \qquad (5.9) \\ &= -R(T_M,\Delta T_o)/(\underline{1}R(\langle T_M \rangle,\Delta T_o)/\Delta T_o) \\ &= 1.3138 \times 10^{-5} R(T_M,\Delta T_o). \end{aligned}$$

The intersection of Equation 5.8 and 5.9 is the critical Rayleigh number for the transition from nonconvection to steady state convection. It is

$$R_I(T_M,\Delta T_o) = 1908 \pm 137. \quad (5.10)$$

This value is significantly higher than the theoretical value of 1708. However, the experimental result is considerably improved with the correction of Equation 4.47. Applying the correction, Equation 5.7 becomes

$$dT(\underline{1})/dz = -7.177 \times 10^{-2} + 5.619 \times 10^{-5} R(T_M,\Delta T). \quad (5.11)$$

The intersection of Equations 5.9 and 5.11 is

$$R_I(T_M,\Delta T) = 1667 \pm 137. \quad (5.12)$$

Table 5.1

Experimental evaluations of the first critical Rayleigh number. σ is the standard deviation or uncertainty.

Reference	R_I	σ	Fluid
Schmidt and Milverton(1935)[26]	1770	140	water
Schmidt and Saunders(1938)[27]	1750	100	water
Malkus(1954)[6]	1700	80	water
Silveston(1958)[28]	1700	51	water, glycol
Gille and Goody(1964)[29]	1786	16	air
Thompson and Sagin(1966)[30]	1793	80	argon, air, CO_2
Rossby(1969)[9]	1750	130	water, silicon oil, Hg
Tarhadieh and Tankin(1974)[12]	1700	30	water
This work	1667	137	water

Figure 5.4

Time sequential temperature distributions for $R(T_M,\Delta T) = 1.37 \times 10^5$.

Curve	t/1 sec	C/1°C
1	0	0.0
2	15	0.1
3	30	0.2
4	45	0.3
5	60	0.4
6	75	0.5
7	90	0.6
8	105	0.7

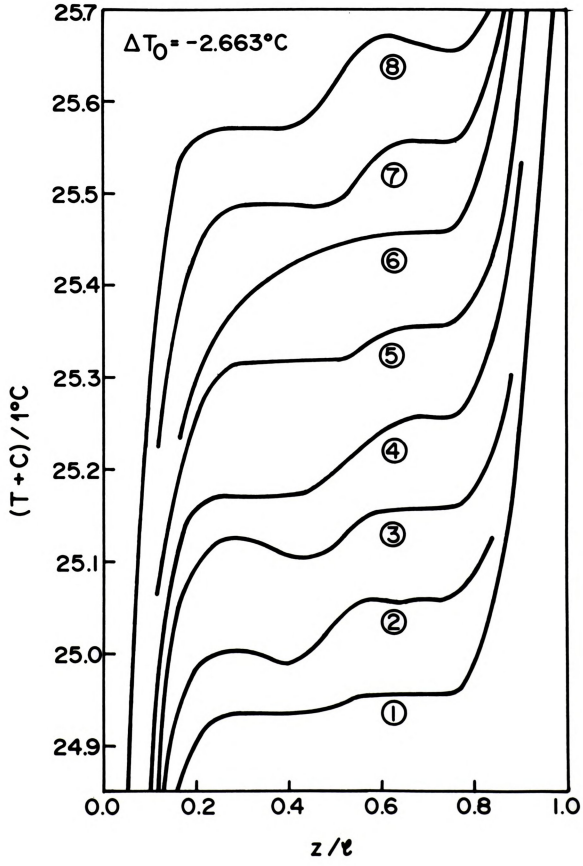
$\Delta T_0 = -2.663°C$
(T + C) / 1°C
z / ℓ
25.7
25.6
25.5
25.4
25.3
25.2
25.1
25.0
24.9
0.0
0.2
0.4
0.6
0.8
1.0
①
②
③
④
⑤
⑥
⑦
⑧

The agreement of this value with the theoretical value is further evidence for the existence of the temperature jump discussed in Section 4.3. It also justifies the use of Equation 4.47 in converting $R(T_M,\Delta T_o)$ values to the $R(T_M,\Delta T)$ values reported in many of the figures of this chapter.

Table 5.1 compares experimentally determined values of the first critical Rayleigh number. A final example of temperature distribution is provided by the time-sequential distributions at $R(T_M,\Delta T) = 1.37 \times 10^5$ shown in Figure 5.4.

5.3 Fluctuations and Frequency Spectrum

For Rayleigh numbers not much higher than approximately 4×10^4, the intensity fluctuations of the Bryngdahl image can be very periodic. The output of a photomultiplier placed at image center reveals that at $R = 8.37 \times 10^4$ the fringe oscillate with a period of 0.5 min(Figure 5.5). Dividing this period by the basic time unit $\rho\tilde{C}_V l^2/k$(i.e., 1.425×10^3 sec at 24.5°C for water) yields the dimensionless period $\tau = 2.11 \times 10^{-2}$. This is intermediate between the shortest period oscillations($\tau = 1.6 \times 10^{-2}$ and 2.6×10^{-2}) reported by Krishnamurti.[11]

Both the intensity fluctuation rate and amplitude increase with Rayleigh number, and the photomultiplier output is visually aperiodic for the Rayleigh numbers of Figure 5.6. The fluctuations provide a convenient method

Figure 5.5

Intensity fluctuations at image center of Bryngdahl image for $R(T_M, \Delta T) = 8.37 \times 10^4$.

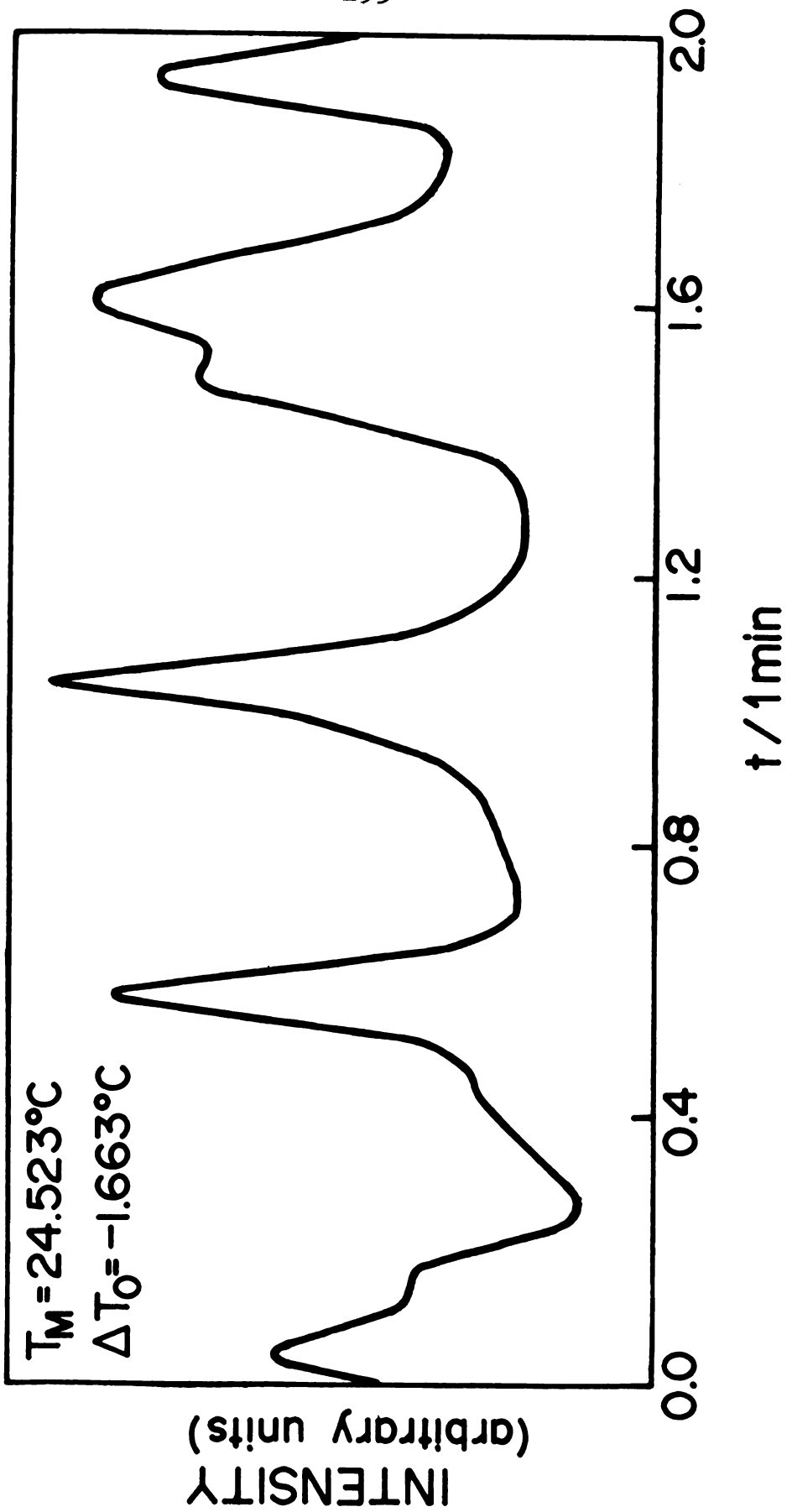
INTENSITY
(arbitrary units)
0.0
0.4
0.8
1.2
1.6
2.0
t/1min
T_M=24.523°C
ΔT_0=-1.663°C

Figure 5.6

Intensity fluctuations at image center of Bryngdahl image for various impressed temperature gradients.

$-\Delta T_o/1^oC$	$10^{-5}R(T_M,\Delta T)$
4.088	2.93
4.878	2.14
6.511	3.06
7.582	3.71

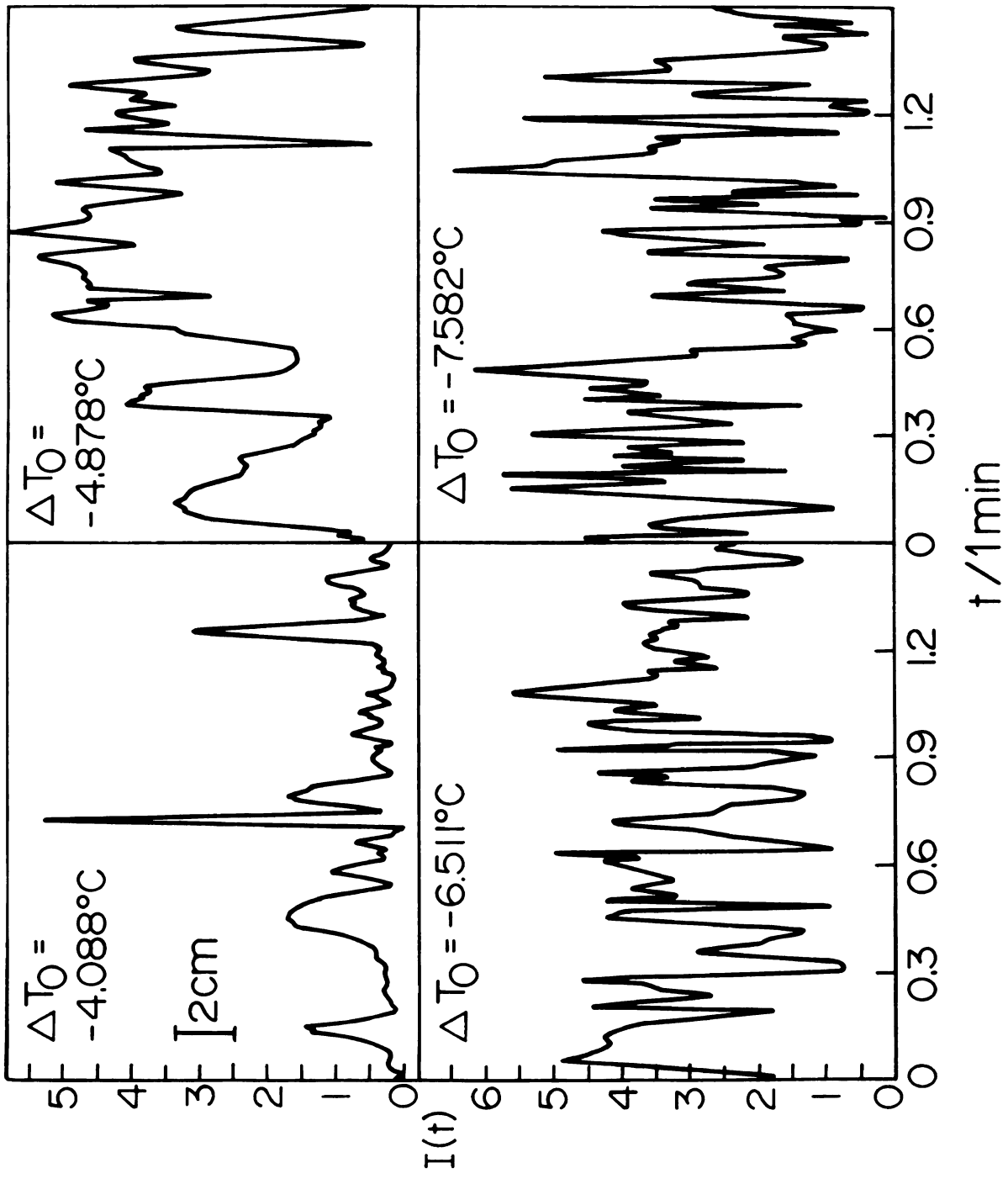
ΔT₀ = -4.088°C
ΔT₀ = -4.878°C
ΔT₀ = -6.511°C
ΔT₀ = -7.582°C
2cm
I(t)
t/1min
0
0.3
0.6
0.9
1.2
1
2
3
4
5
6

for the determination of the critical Rayleigh transition R_{IV}. A plot of the fluctuation rate as a function of ΔT_o (Figure 5.7) indicates the linear relationship

$$\text{no. fluctuations per min} = 3.970(|\Delta T_o| - 0.805) \qquad (5.13)$$

$$\sigma = 2.625$$

$$\sigma_a = 1.064$$

$$\sigma_b = 0.174$$

$$r^2 = 0.970.$$

The standard error of the regression coefficients improve when the functional dependence upon Rayleigh number is considered. Then

$$\text{no. fluctuations per min} = 6.457 \times 10^{-5}(R(T_M,\Delta T_o) - 4.898 \times 10^4) \qquad (5.14)$$

$$\sigma = 1.568$$

$$\sigma_a = 0.631$$

$$\sigma_b = 1.676 \times 10^{-6}$$

$$r^2 = 0.989.$$

Equation 5.13 states that an apparent transition from small amplitude fluctuations(not detectable with the photomultiplier) to large amplitude fluctuations occurs at $\langle \Delta T_o \rangle_{IV} = -0.805^oC$. Equation 5.14 establishes the critical Rayleigh number $R_{IV}(T_M,\Delta T_o) = 4.90 \times 10^4 \pm 14\%$. Applying the temperature jump correction, the result is

$$R_{IV}(T_M,\Delta T) = 4.42 \times 10^4 \pm 14\%. \qquad (5.15)$$

Figure 5.7

Bryngdahl image intensity fluctuation rate at cell center versus impressed temperature gradient and versus Rayleigh number. The solid lines are Equations 5.13 and 5.14.

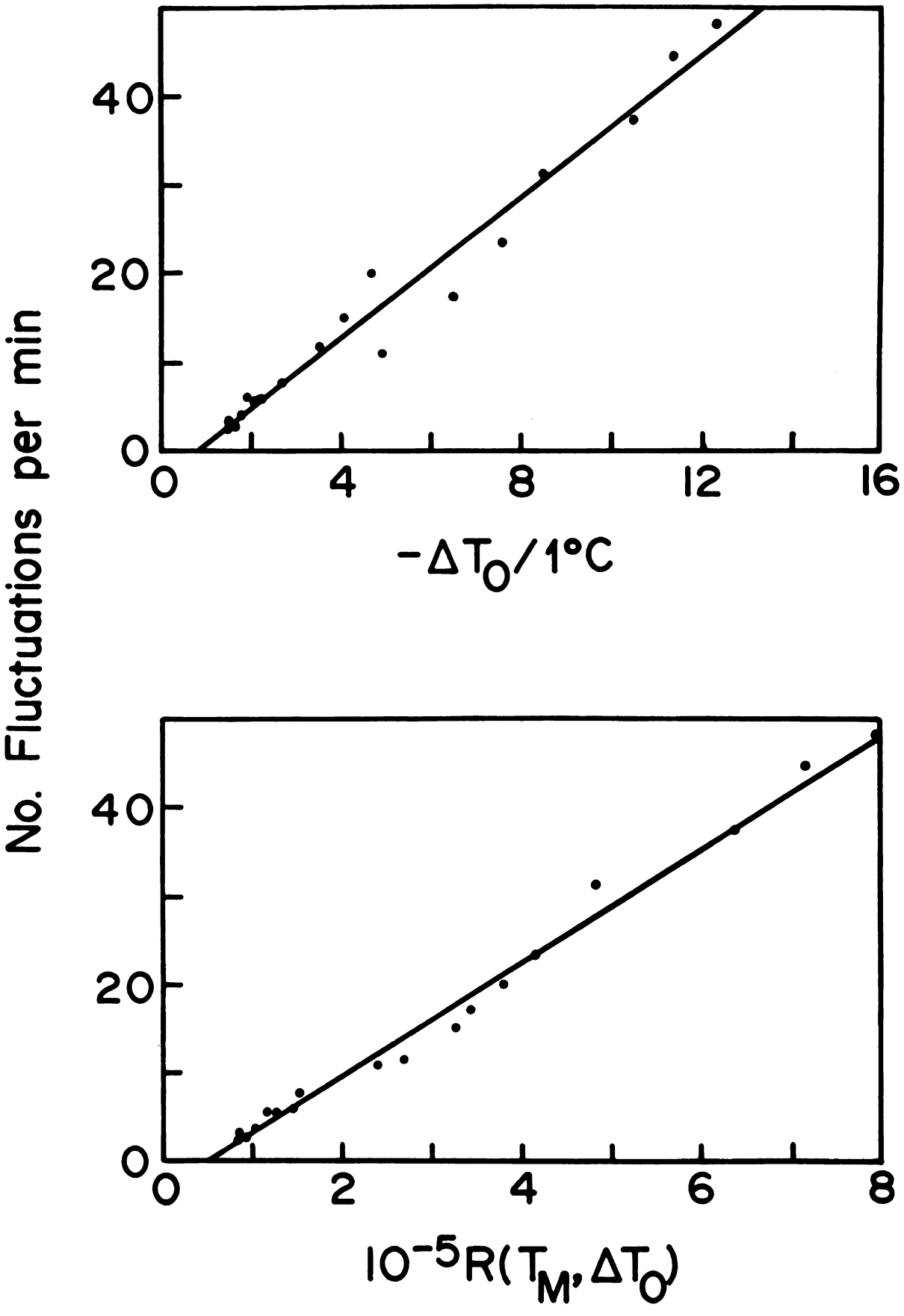
No. Fluctuations per min
40
20
0
0
4
8
12
16
$-\Delta T_0/1°C$
40
20
0
0
2
4
6
8
$10^{-5}R(T_M, \Delta T_0)$

This is in excellent agreement with Krishnamurti's[11] report of $R_{IV} \sim 4.4 \times 10^4$. Malkus[6] also observed a transition from one turbulent mode to another but at $R \sim 5.5 \times 10^4$.

The frequency spectrum of the fluctuations is the Fourier transform of the photomultiplier output autocorrelation function. It is very important in developing an understanding of aperiodic motions.[31,32] Let $\Delta I(t)$ be the photomultiplier output at time t minus the time averaged output. The autocorrelation function, $R(t)$, is then defined to be

$$R(t) = \lim_{X \to \infty} (1/|X|) \int_0^X \Delta I(t_1) \Delta I(t_1 + t) dt_1. \tag{5.16}$$

This is an even function; therefore, the Fourier transform of $R(t)$, $F(\omega)$, is

$$F(\omega) = \lim_{X \to \infty} \int_{-X}^{X} R(t) \cos(\omega t) dt. \tag{5.17}$$

The importance of $F(\omega)$ is demonstrated by the Wiener-Khintchine theorem:[33]

$$F(\omega) = |\text{Fourier transform of } \Delta I(t)|^2 \tag{5.18a}$$

$$= |\pi A(\omega)|^2 \tag{5.18b}$$

where

$$I(t) = \int_0^\infty A(\omega) \cos(\omega t) d\omega. \tag{5.18c}$$

Thus, $F(\omega)$ is proportional to the square of the harmonic frequency amplitude. Applying this correlation analysis to the intensity fluctuations of Figure 5.6, the integrals of Equation 5.16 and 5.17 are numerically evaluated with the trapezoidal rule.[34] Furthermore, the time increment $\Delta t = 0.01$ min and the time interval $X = 5$ min are used.

Figure 5.8 is the autocorrelation function for $\Delta T = -6.849^{o}C$ and $R(T_M,\Delta T) = 3.71 \times 10^5$. Figure 5.9 indicates that $F(\omega)/\epsilon$ where

$$\epsilon = \langle \Delta T \rangle_{IV} - \Delta T \tag{5.19}$$

is approximately independent of the impressed temperature difference. Four harmonics in the ratio $\omega_1/\omega_2/\omega_3/\omega_4 \sim 1/3/9/14$ are distinctly visible and the best exponential description of the maxima is

$$F(\omega)/\epsilon \sim e^{-0.0132\,\omega} \tag{5.20}$$

where ω has the dimension min^{-1}. The only comparable observations are those of Krishnamurti.[11] Her reported oscillation periods of light scattering from aluminum flakes seem to be components of the two lowest frequency peaks shown in Figure 5.9.

5.4 Summary

Bryngdahl interferometrically determined temperature derivatives have proven very useful in the detection and quantitative evaluation of critical transitions between different modes of flow. Experimental determination of

Figure 5.8

Autocorrelation function of $\Delta I(t)$ for $\Delta T = -6.849^{o}C$ and $R(T_M, \Delta T) = 3.71 \times 10^5$.

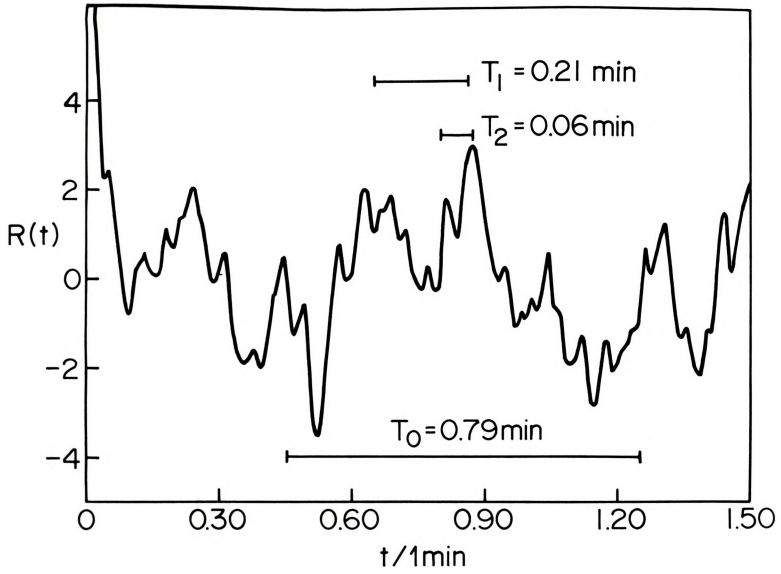
T_1 = 0.21 min
T_2 = 0.06 min
T_0 = 0.79 min
R(t)
4
2
0
-2
-4
0
0.30
0.60
0.90
1.20
1.50
t/1min

Figure 5.9

Fourier transform of autocorrelation function of $\Delta I(t)$ divided by $\epsilon = |\Delta T| - 0.727^{o}C$. The solid line of curve D is proportional to Equation 5.20; the experimental points are the maxima of curves A, B, and C. T is in ^{o}C.

	$-\Delta T$	T_M	$10^{-5}R(T_M,\Delta T)$
A(o)	3.693	31.633	2.93
B(□)	5.881	23.342	3.06
C(Δ)	6.849	24.033	3.71

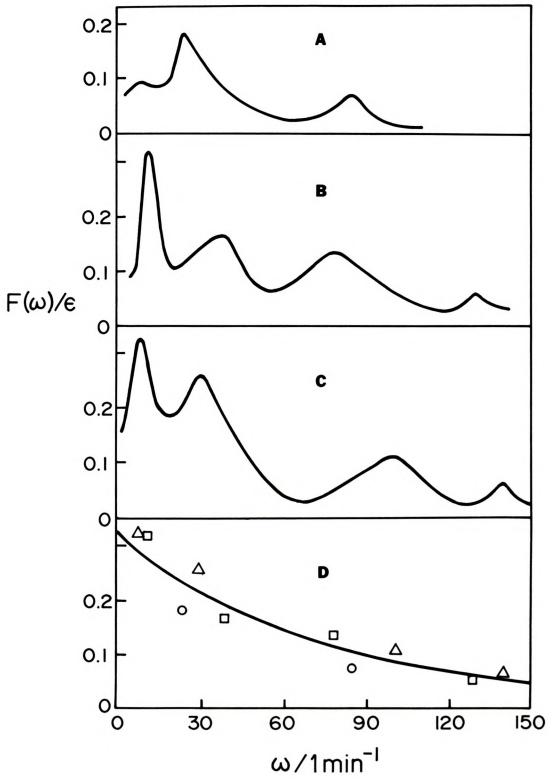
A
B
C
D
0.2
0.1
0
F(ω)/ε
0
30
60
90
120
150
ω/1min⁻¹

boundary temperature gradients as a function of Rayleigh number has yielded the critical Rayleigh transitons $R_I = 1667 \pm 137$ and $R_{III} = 3.3 \times 10^4 \pm 12\%$ for water. It has not proven possible to detect temperature inversion at intermediate distances from boundaries because of the small, nearly constant, temperature gradients involved.

Fluctuations in the Bryngdahl interferometer image have proven to be extremely valuable in the study of time-dependent properties. First, the fluctuations provide strong evidence of the existence of a fourth Rayleigh transition at $R_{IV} = 4.42 \times 10^4 \pm 14\%$. Second, autocorrelation analysis of intensity fluctuations reveals four major frequency bands at $\omega \sim 10$, 30, 90, and 140 min^{-1}. The intensity of the bands seems to be proportional to $\epsilon = \langle \Delta T \rangle_{IV} - \Delta T$ and they decrease exponentially with the angular frequency 75.8 min^{-1}. Both theoretical and further experimental work are needed to determine whether these frequency bands are the manifestation of buoyancy effects driven by thermodynamic fluctuations within the liquid or whether one or more of the bands are due to instabilities driven by room and plate vibrations. Because of the unique nature of the Bryngdahl interferometric observations, no relevant literature comparison is possible. Lack of a theoretical description provides a good, although extremely difficult, field of research. Numerical computations[35,36] show that temperature fluctuations can be conceptualized as thermal elements or "plumes" which break away from the

lower thermal layer and rise in the cooler, denser surroundings.

Bryngdahl interferometry cannot detect the transition from two-dimensional flow to three-dimensional flow at R_{II} because of the absence of both temperature fluctuations and nonlinear variation of the boundary temperature gradient with Rayleigh number. Busse's[37] theoretical study of two-dimensional convection demonstrates that such a transition is possible at $R = 2.3 \times 10^4$ for high Prandtl number fluids. However, in the limit of small Prandtl number, Busse finds that two-dimensional rolls become unstable to oscillatory three-dimensional disturbances when the amplitude of the convective motion exceeds a finite critical value.[38] It may be possible to detect this transition with the Bryngdahl interferometer.

Finally, the successful evaluation of R_{III} and R_{IV} for water suggests that Bryngdahl interferometry can be used to determine the dependence of the critical Rayleigh numbers upon Prandtl number. This dependence is believed to be very strong for Prandtl numbers lower than that of water.[11]

APPENDIX

APPENDIX

FOURIER POWER SERIES SOLUTION OF THE VIBRATIONAL RELAXATION EQUATION

The general differential form of the vibrational relaxation models of Chapter 2 is

$$(-1)^k(1-e^{-\theta})d^kx_n/d\zeta^k + ne^{-\theta}x_{n-1} + (n+1)x_{n+1} + ((n+1)e^{-\theta} + n)x_n = 0. \tag{A.1}$$

Model 1 has $k = 2$ and $\zeta = (K/D)^{1/2}z$; Model 2 has $k = 1$ and $\zeta = (K/V)z$. This equation must be solved subject to the conditions

$$x_n(\zeta) = x_n(0) \quad \text{at } \zeta = 0 \qquad \text{and} \tag{A.2}$$

$$\lim_{\zeta\to\infty} x_n(\zeta) = (1-e^{-\theta})e^{-n\theta}. \tag{A.3}$$

Further, it is assumed that the variation of θ with ζ is negligible.

Taking the solution to have the form

$$x_n(\zeta) = \sum_{u=0}^{\infty} a_u \underline{l}_n(u)e^{-u^{1/k}\zeta}, \tag{A.4}$$

we find from Equation A.1 that

$$(1-e^{-\theta})u\underline{l}_n + ne^{-\theta}\underline{l}_{n-1} + (n+1)\underline{l}_{n+1} + ((n+1)e^{-\theta} + n)\underline{l}_n = 0. \tag{A.5}$$

Gottlieb(Am. J. Math., 60, 453(1938)) has shown that the polynomials which satisfy this recurrence formula are

$$\underline{l}_n(u) = e^{-n\theta}\sum_{v=0}^{n}(1-e^{\theta})^v\binom{n}{v}\binom{u}{v}. \tag{A.6}$$

Montroll and Shuler(J. Chem. Phys., 26, 454(1957)) have shown that

$$\underline{l}_n(u) = F(-n, u+1, 1; 1-e^{-\theta}) \tag{A.7}$$

where F(a, b, c; z) is the hypergeometric function. The Gottlieb polynomials have the following properties:

$$e^{n\theta}\underline{l}_n(u) = e^{u\theta}\underline{l}_u(n), \tag{A.8}$$

$$\sum_{v=0}^{\infty} e^{-v\theta}\underline{l}_n(v)\underline{l}_m(v) = e^{-n\theta}(1-e^{-\theta})^{-1}\delta_{n,m}, \tag{A.9}$$

and

$$\sum_{n=0}^{\infty} e^{n\theta}\underline{l}_n(v)\underline{l}_n(u) = e^{v\theta}(1-e^{-\theta})^{-1}\delta_{v,u} \tag{A.10}$$

where $\delta_{n,m}$ is the Kronecker delta. To evaluate the functions a_u, left operate on Equation A.5 with the summation operator $\sum_{n=0}^{\infty} e^{n\theta}\underline{l}_n(v)$; then, evaluate the results at $\zeta = 0$. Using Equations A.8-A.10, it is found that

$$a_u = e^{-u\theta}(1-e^{-\theta})\sum_{n=0}^{\infty} e^{n\theta}\underline{l}_n(u)x_n(0). \tag{A.11}$$

Finally, by Equations A.4, A.6, and A.11

$$\lim_{\zeta\to\infty} x_n = a_0 \underline{l}_n(0) = a_0 e^{-n\theta}$$

$$= e^{-n\theta}(1-e^{-\theta}) \sum_{n=0}^{\infty} x_n(0)$$

$$= e^{-n\theta}(1-e^{-\theta}).$$

The last equation follows from the normalization of probability.

In summary, the solution of Equation A.1 is

$$x_n(\zeta) = \sum_{u=0}^{\infty} a_u \underline{l}_n(u) e^{-u^{1/k}\zeta} \tag{A.12}$$

where

$$\underline{l}_n(u) = e^{-n\theta} \sum_{v=0}^{n} (1-e^{\theta})^v \binom{n}{v}\binom{u}{v} \tag{A.13}$$

and

$$a_u = e^{-u\theta}(1-e^{-\theta}) \sum_{n=0}^{\infty} e^{n\theta} \underline{l}_n(u) x_n(0). \tag{A.14}$$

LIST OF REFERENCES

Chapter 1 References

1. J. Kestin, ed., Transport Phenomena-1973, a Brown University Seminar, (American Institute of Physics, 1973).

2. R.D. Levine and J. Jortner, ed., Molecular Energy Transfer, (John Wiley, 1976).

3. J. Fourier, Theorie Analytique de la Chaleur, 1822; translated by A. Freeman, 1878; Dover, 1955.

4. C. Truesdell and R.A. Toupin, in The Encyclopedia of Physics, Vol. III/1, ed. by S. Flugge, (Springer-Verlag, 1960). The Classical Field Theories.

5. B.D. Coleman and W. Noll, Arch. Rat. Mech. Anal., 13, 167 (1963). The Thermodynamics of Elastic Materials with Heat Conduction and Viscosity.

6. B.D. Coleman and V.J. Mizel, Arch. Rat. Mech. Anal., 13, 245 (1963). Thermodynamics and Departures from Fourier's Law of Heat Conduction.

7. M.E. Gurtin and A.C. Pipkin, Arch. Rat. Mech. Anal., 31, 113 (1968). A General Theory of Heat Conduction with Finite Wave Speeds.

8. H.J. Petroski, Arch. Rat. Mech. Anal., 35,342 (1969). On the Use of Steady Linear Temperature Fields to Characterize a Class of Rigid Heat Conductors.

9. I. Muller, Arch. Rat. Mech. Anal., 41, 319 (1971). The Coldness, a Universal Function in Thermoelastic Bodies.

10. W. Noll, Arch. Rat. Mech. Anal., 52, 62 (1973). Lectures on the Foundations of Continuum Mechanics and Thermodynamics.

11. R.C. Batra, Arch. Rat. Mech. Anal., 53, 359 (1974). A Thermodynamic Theory of Rigid Heat Conductors.

12. P. Dean, in Transfer and Storage of Energy by Molecules, Vol. 4, ed. by G.M. Burnett, A.M. North, and J.N. Sherwood, (John Wiley, 1974). Phonon Processes in Amorphous Solids.

13. A.Z. Chechel'nitskii, High Temp. (USSR), 10,251 (1972). On the Thermal Conductivity of Fused Quartz in the Temperature Range 350-1100K.

14. E.N. Bezrukova, A.A. Men', and O.A. Sergeev, High Temp. (USSR), 11, 79 (1973). Photon Conductivity of Solids.

15. A.A. Men' and A.Z. Chechel'nitskii, High Temp. (USSR), 11, 1176 (1973). Thermal Conductivity of Fused Quartz.

16. R. Viskanta and E.E. Anderson, Ad. Heat Transfer, 11, 317 (1975). Heat Transfer in Semitransparent Solids.

17. M. Jakob, Heat Transfer, (John Wiley, 1949).

18. H.S. Carslaw and J.C. Jaeger, Conduction of Heat in Solids, (Oxford, 1959).

19. S.S. Kutateladze and V.M. Borishanskii, A Concise Encyclopedia of Heat Transfer, (Pergamon Press, 1966).

20. W. Leidenfrost, in Thermal Conductivity Proceedings of the Eighth Conference, ed. by C.Y. Ho and R.E. Taylor, (Plenum, 1969). Critical Analysis of the Experimental Determination of the Thermal Conductivity of Steam.

21. W. Leidenfrost, in Measurement Techniques in Heat Transfer, ed. by E.R.G. Eckert and R.J. Goldstein, p. 397, (AGARDograph 130, 1970). Measurement of Thermophysical Properties.

22. S.G. Brush, Arch. Hist. Exact Sciences, 11, 38 (1973). The Development of the Kinetic Theory of Gases.

23. G.G. Stokes, Cambridge and Dublin Math. J., 6, 215 (1851). On the Conduction of Heat in Crystals. Reprinted in Mathematical and Physical Papers by the Late Sir George Gabriel Stokes, Vol.3, p. 203, (Johnson Reprint Corp., 1966).

24. H.L. Johnston and E.R. Grilly, J. Chem. Phys., 14, 233 (1946). The Thermal Conductivity of Eight Common Gases between 80 K and 380 K.

25. H. Geier and K. Schafer, Allgem. Warmetechnik, 10, 70 (1961). Warmeleitfahigkeit von Reinen Gasen und Gasmischen Zwischen 0°C and 1200°C.

26. R.W. Powell, C.Y. Ho, and P.E. Liley, Thermal Conductivity of Selected Materials, (NSRDS-NBS 8, November 1966).

27. J. Gille and R. Goody, J. Fluid Mech., 20, 47 (1964). Convection in a Radiating Gas.

28. W.P. Schimmel, J.L. Novotny, and F.A. Olsofka, Heat Transfer, 3, R2.1, (Elsevier, 1970). Interferometric Study of Radiation-Conduction Interaction.

29. T. Audunson and B. Gebhart, J. Fluid Mech., 52, 57 (1972). An Experimental and Analytical Study of Natural Convection with Appreciable Thermal Radiation Effects.

30. J.C. Bratis and J.L. Novotny, Int. J. Heat Mass Transfer, 17, 23 (1974). Radiation-Convection Interaction in the Boundary Layer Regime of an Enclosure.

31. H.A. Lorentz, Lectures on Theoretical Physics, Vol. 1, (MacMillan, 1927).

32. E.H. Kennard, Kinetic Theory of Gases,(McGraw-Hill, 1938).

33. L.B. Loeb, The Kinetic Theory of Gases,(McGraw-Hill, 1927; Dover, 1961).

34. J. Jeans, An Introduction to the Kinetic Theory of Gases,(Cambridge, 1940).

35. R.G. Vines, Rev. Pure Appl. Chem., 4, 207 (1954). The Interchange of Energy Between Molecules During Collisions in the Gas Phase at Solid Surfaces.

36. F.O. Goodman, Prog. Surf. Sci., 5, 261 (1974). Thermal Accommodation.

37. M.N. Kogan, Rarefied Gas Dynamics, (Plenum, 1969).

38. J.H. Ferziger and H.G. Kaper, Mathematical Theory of Transport Processes in Gases, (North-Holland, 1972).

Chapter 2 References

1. R.J. Rubin and K.E. Shuler, J. Chem. Phys., 25, 59 (1956). Relaxation of Vibrational Nonequilibrium Distributions. I. Collisional Relaxation of a System of Harmonic Oscillators.

2. R.J. Rubin and K.E. Shuler, J. Chem. Phys., 25, 68 (1956). Relaxation of Vibrational Nonequilibrium Distributions. II. The Effect of Collisional Transition Probabilities on the Relaxation Behavior.

3. R.J. Rubin and K.E. Shuler, J. Chem. Phys., 26, 137 (1957). On the Relaxation of Vibrational Distributions. III. The Effect of Radiative Transitions on the Relaxation Behavior.

4. E.W. Montroll and K.E. Shuler, J. Chem. Phys., 26, 454 (1957). Studies in Nonequilibrium Rate Processes. I. The Relaxation of a System of Harmonic Oscillators.

5. E. Montroll, Lect. Theor. Phys., 3, 221 (1960). Nonequilibrium Statistical Mechanics.

6. S. Chandrasekhar, Rev. Mod. Phys., 15, 1 (1943). Stocastic Problems in Physics and Astronomy.

7. E.W. Montroll and K.E. Shuler, Adv. Chem. Phys., 1, 361 (1958). The Application of the Theory of Stocastic Processes to Chemical Kinetics.

8. W.G. Vincenti and G.H. Kruger, Jr., Introduction to Physical Gas Dynamics, (John Wiley, 1965).

9. I. Oppenheim, K.E. Shuler, and G.H. Weiss, Adv. Mol. Relaxation Processes, 1, 13 (1967). Stocastic Theory of Multistate Relaxation Processes.

10. D.A. McQuarrie, J. Appl. Prob., 4, 413 (1967). Stocastic Approach to Chemical Kinetics.

11. D.A. McQuarrie, Adv. Chem. Phys., 15, 149 (1969). Stochastic Theory of Chemical Rate Processes.

12. E. Teramoto, N. Shigesada, H. Nakajima, and K. Sato, Advan. Biophys., 2, 155 (1971). Stochastic Theory of Reaction Kinetics.

13. S.H. Lin and H. Eyring, Ann. Rev. Phys. Chem., 25, 39 (1974). Stochastic Processes in Physical Chemistry.

14. L. Landau and E. Teller, Phys. Z. Sovjetunion, 10, 34 (1936). On the Theory of Sound Dispersion.

15. J.L. Stretton, in Transfer and Storage of Energy by Molecules, Vol. 2, p. 58, ed. by G.M. Burnett and A.M. North, (Wiley-Interscience, 1969). Vibrational Energy Exchange at Molecular Collisions.

16. D. Rapp and T. Kassal, Chem. Rev., 69, 61 (1969). The Theory of Vibrational Energy Transfer Between Simple Molecules in Nonreactive Collisions.

17. S. Ormonde, Rev. Mod. Phys., 47, 193 (1975). Vibrational Relaxation Theories and Measurements.

18. W. Magnus, F. Oberhettinger, and R.P. Soni, Formulas and Theorems for the Special Functions of Mathematical Physics, (Springer-Verlag, 1966).

19. M.J. Gottlieb, Am. J. Math., 60, 453 (1938). Concerning Some Polynomials Orthogonal on a Finite or Enumerable Set of Points.

20. H.Y. Wachman, J. Chem. Phys., 42, 1850 (1965). Method for Determining Accommodation Coefficients from Data in the Temperature-Jump Range without Appling Temperature-Jump Theory.

21. R.E. Harris, J. Chem. Phys., 46, 3217 (1967). On the Determination of Thermal Accommodation Coefficients in the Temperature-Jump Region.

22. S.H.P. Chen and S.C. Saxena, Int. J. Heat Mass Transfer, 17, 185 (1974). Interface Heat Transfer and Thermal Accommodation Coefficients: Heated Tungsten Wire in Nitrogen Environment.

23. B.J. Jody and S.C. Saxena, Phys. Fluids, 18, 20 (1975). Thermal Conductivity of Neon from Heat Transfer Measurements in the Continuum and Temperature-Jump Regimes.

24. T.L. Cottrell and J.C. McCoubrey, Molecular Energy Transfer in Gases, (Butterworths, 1961).

25. G.M. Burnett and A.M. North (ed.), Transfer and Storage of Energy by Molecules, Vol. 2, (Wiley, 1969).

26. B. Stevens, Collisional Activation in Gases, (Pergamon, 1967).

27. P.C.M. van Woerkom, J. de Bleijser, M. de Zwart, P.M.J. Burgers,and J.C. Leyte, Ber. Bunsenges. Physik. Chem., 78, 1303 (1974). Vibrational Relaxation in Liquids; Some Applications of the Isotopic Dilution Method.

28. W.G. Rothschild, G.J. Rosasco, and R.C. Livingston, J. Chem. Phys., 62, 1253 (1975). Dynamics of Molecular Reorientational Motion and Vibrational Relaxation in Liquids. Chloroform.

29. A. Laubereau and W. Kaiser, Ann. Rev. Phys. Chem., 26, 83 (1975). Picosecond Spectroscopy of Molecular Dynamics in Liquids.

30. W.F. Calaway and G.E. Ewing, Chem. Phys. Letters, 30, 485 (1975). Vibrational Relaxation in Liquid Nitrogen.

31. W.F. Calaway and G.E. Ewing, J. Chem. Phys., 63, 2842 (1975). Vibrational Relaxation of Small Molecules in the Liquid Phase: Liquid Nitrogen Doped with O_2, CO, and CH_4.

32. J.O. Hirschfelder, C.F. Curtiss, and R.B. Bird, Molecular Theory of Gases and Liquids, (Wiley, 1954).

33. W. Ibele, in the Handbook of Heat Transfer, ed. by W.M. Rohsenow and J.P. Hartnett, (McGraw-Hill, 1973). Thermochemical Properties.

34. T.K. Sherwood, R.L. Pigford, and C.R. Wilke, Mass Transfer, (McGraw-Hill, 1975).

35. JANAF Thermochemical Tables, 2nd ed., NSRDS-NBS 37, (June, 1971).

36. G. Herzberg, Infrared and Raman Spectra of Polyatomic Molecules, (D. Van Nostrand, 1945).

37. T. Shimanouchi, DSRDS-NBS 39, (June, 1972). Tables of Molecular Vibrational Frequencies.

38. G. Houghton, J. Chem. Phys., 40, 1628 (1964). Cubic Cell Model for Self-Diffusion in Liquids.

39. N.B. Vargaftik, Tables on the Thermophysical Properties of Liquids and Gases, (Hemisphere, 1975).

40. K. Raznjevic, Handbook of Thermodynamic Tables and Charts, (McGraw-Hill, 1976).

41. F.J. Bartoli and T.A. Litovitz, J. Chem. Phys., 56, 413 (1972). Raman Scattering: Orientational Motions in Liquids.

42. P.K. Davis and I. Oppenheim, J. Chem. Phys., 57, 505 (1972). Vibrational Relaxation in Liquids.

43. P.K. Davis, J. Chem. Phys., 57, 517 (1972). Collision Frequencies in Liquids.

44. D. Eisenberg and W. Kauzmann, The Structure and Properties of Water, (Oxford University Press, 1969).

45. C.W. Robertson, B. Curnutte, and D. Williams, Mol. Phys., 26, 183 (1973). The Infrared Spectrum of Water.

Chapter 3 References

1. E. Ingelstam, Ark. Fys., 9, 197 (1955). Measurements Of Optical Path Gradients By Means Of Birefringence Interferences.

2. E. Ingelstam, J. Opt. Soc. Am., 47 536 (1957). Some Quantitative Measurements Of Path Differences And Gradients By Means Of Phase Contrast And New Interferometric Devices.

3. O. Bryngdahl, Acta Chem. Scand., 11, 1017 (1957). A New Interferometric Method For The Determination Of Diffusion Coefficients Of Very Dilute Solutions.

4. O. Bryngdahl, Acta Chem. Scand., 12, 684 (1958). Interferometric Studies Of Boundary Formation And Deviations From Ideality In Diffusion Experiments.

5. O. Bryngdahl and S. Ljunggren, J. Phys. Chem., 64, 1264 (1960). A New Refractive Index Gradient Recording Interferometer Suitable For Studying Diffusion, Electrophoresis, And Sedimentation.

6. O. Bryngdahl, Ark. Fys., 21, 289 (1961). Genaue Bestimmungen Der Warmeleiteigenschaften In Flussigkeiten Mit Einer Scherinterferometrischen Methode.

7. O. Bryngdahl and S. Ljunggren, Acta Chem. Scand., 16, 2162 (1962). Neuartige Berechnungsmethoden Und Forderungen An Scherinterferometrische Prazisions-bestimmungen Von Diffusionskoeffizienten.

8. O. Bryngdahl, J. Opt. Soc. Am., 53, 571 (1963). Wavefront Shearing Interferometer For Direct Recording Of Refractive Index Gradient In Cartesian Coordinates.

9. S.E. Gustafsson, J.G. Becsey, and J.A. Bierlein, J. Phys. Chem., 69, 1016 (1965). Thermal Diffusion Measurements By Wavefront Shearing Interferometry.

10. S.E. Gustafsson, Z. Naturforsch., 22A, 1005 (1967). A Non-Steady-State Method Of Measuring The Thermal Conductivity Of Transparent Liquids.

11. L.W. Wendelov, L.-E. Wallin, and S.E. Gustafsson, Z. Naturforsch., 22A, 1180 (1967). Refractive Index Measurements Of Molten Salts With Wavefront Shearing Interferometry. I: Test Of Apparatus And Procedure.

12. L.W. Wendelov, S.E. Gustafsson, N.-O. Halling, and R.A.E. Kjellander, Z. Naturforsch., 22A, 1363 (1967). Refractive Index Measurements Of Molted Salts With Wavefront Shearing Interferometry. II: $LiNO_3$, $NaNO_3$, KNO_3, $RbNO_3$, And $CsNO_3$.

13. S.E. Gustafsson, N.-O. Halling, and R.A.E. Kjellander, Z. Naturforsch., 23A, 44 (1968). Optical Determinations Of Thermal Conductivity With A Plane Source Technique.

14. S.E. Gustafsson, N.-O. Halling, and R.A.E. Kjellander, Z. Naturforsch., 23A, 682 (1968). Optical Determination Of Thermal Conductivity With A Plane Source Technique. II: Molten $LiNO_3$, $RbNO_3$, And $CsNO_3$.

15. S.E. Gustafsson, L.-E. Wallin, and T.E.G. Arvidsson, Z. Naturforsch., 23A, 1261 (1968). A Plane Source Method For Measuring Interdiffusion Coefficients Of Transparent Liquids.

16. L.-E. Wallin, and S.E. Gustafsson, Z. Naturforsch., 24A, 436 (1969). On Non-Ideal Conditions In Plane Source Diffusion Experiments.

17. L.-E. Wallin, and K. Wallin, Optica Acta, 17, 381 (1970). The Savart Interferometer Modified For High Sensitivity In Measurements Of Refractive Index Gradients.

18. L.-E. Wallin, J. Chem. Phys., 52, 552 (1970). Thermal Diffusion Measurements With A Modified Savart Interferometer.

19. T.E.G. Arvidsson, S.-A. Afsenius, and S.E. Gustafsson, J. Chem. Phys., 53, 2621 (1970). Interdiffusion Measurements In Fused Alkali Nitrates By Wavefront Shearing Interferometry.

20. T.E.G. Arvidsson, S.-A. Afsenius, and S.E. Gustafsson, Z. Naturforsch., 26A, 752 (1971). Interdiffusion Studies In Molten Alkali Nitrates.

21. S.D.H. Andreasson, S.E. Gustafsson, and N.-O. Halling, J. Opt. Soc. Am., 61, 595 (1971). Measurement Of The Refractive Index Of Transparent Solids And Fluids.

22. I. Okada, and S.E. Gustafsson, Electrochim. Acta, 18, 275 (1973). Interdiffusion Of Thallous Ion In Molten Lithium Nitrate Studied By Optical Interferometry.

23. S.E. Gustafsson, E. Karawacki, and I. Okada, Z. Naturforsch, 30A, 35 (1975). A Method For Measuring Interdiffusion Coefficients In Liquids By Wavefront Shearing Interferometry.

24. E. McLaughlin, Chem. Rev., 64, 389 (1964). The Thermal Conductivity Of Liquids And Dense Gases.

25. L.H. Adams, J. Wash. Acad. Sci., 5, 265 (1915). Some Notes On The Theory Of The Rayleigh-Zeiss Interferometer.

26. W.J. Thomes, and E. McK. Nicholl, Appl. Opt., 4, 823 (1965). The Application Of The Wavefront Shearing Optical Interferometer To Diffusion Measurements.

27. W.J. Thomas, and E. McK. Nicholl, J. Appl. Chem., 17, 251 (1967). Diffusion Measurements For Ethanolamine-Water Systems With A Wavefront Shearing Interferometer.

28. W.J. Thomas, R. Khanna, and E.W. Palmer, Chem. Eng. J., 3, 112 (1972). Physical Absorption Into A Pool Of Liquid (CO_2-Water).

29. W.J. Thomas, R. Khanna, and E.W. Palmer, Chem. Eng. J., 6, 165 (1973). Convective Disturbances In Static Liquid Pools.

30. W.J. Thomas, and M.S. Ray, Chem. Eng. J., 9, 71 (1975). A Study Of Gas Desorption From Static Liquid Pools.

31. C.N. Pepela, B.J. Steel, and P.J. Dunlop, J. Am. Chem. Soc., 92, 6743 (1970). A Diffusion Study At 25°C With A Shearing Diffusiometer. A Comparison With The Gouy And Conductance Methods.

32. G.R. Staker, and P.J. Dunlop, J. Chem. Eng. Data, 18, 61 (1973). Use Of A New Cell To Measure Diffusion Coefficients For The Systems Benzene-Carbon Tetrachloride And Sucrose-Water At 25°C.

33. T.G. Anderson, and F.H. Horne, J. Chem. Phys., 55, 2831 (1971). Pure Thermal Diffusion. II: Experimental Thermal Diffusion Factors And Mutual Diffusion Coefficients For CCl_4-C_6H_{12}.

34. J.D. Olson, and F.H. Horne, J. Chem. Phys., 58, 2321 (1973). Direct Determination Of Temperature Dependence Of Refractive Index Of Liquids.

35. M. Mitchell, and H.J.V. Tyrrell, J. Chem. Soc. (London), 68 F2, 385 (1972). Diffusion Of Benzene, Phenol, And Resorcinol In Propan-1,2-diol, And The Validity Of The Stokes-Einstein Equation.

36. C.J. Skipp, and H.J.V. Tyrrell, J. Chem. Soc. (London), 71 F1, 1744 (1975). Diffusion In Viscous Solvents. II: Planar And Spherical Molecules In Propane-1,2-diol At 15, 25, and 35°C.

37. B. Porsch, and M. Kubin, Coll. Czech. Chem. Commun., 33, 1028 (1968). Limits Of Use Of A Polarization Interferometer For The Measurement Of Diffusion Coefficients At Very Low Concentrations.

38. M. Kubin, and B. Porsch, Eur. Polymer J., 6, 97 (1970). Estimation Of Polymer Polydispersity By Diffusion Measurements At Low Concentration.

39. B. Porsch, and M. Kubin, Coll. Czech. Chem. Commun., 36, 4046 (1971). Flowing-Boundary Diffusion Cell And The Determination Of Zero-Time Correction In Free Diffusion Measurements In Very Dilute Polymer Solutions With A Polarization Interferometer.

40. B. Porsch, and M. Kubin, Coll. Czech. Chem. Commun., 37, 824 (1972). Determination Of Criteria Of Polymer Polydispersity Based On The Free Diffusion Measurements With A Polarization Interferometer.

41. B. Porsch, Coll. Czech. Chem. Commun., 37, 3426 (1972). A Simple And Exact Calculation Method For Binary Diffusion Coefficients From The Data Of Polarization Interferometer.

42. B. Porsch, and M. Kubin, Eur. Polymer J., 9, 1013 (1973). Concentration Dependence Of The Diffusion Coefficient Of Polydisperse Polystyrene In Dilute Solution.

43. L.J. Gosting, Adv. Protein Chem., 429 (1956). Measurement And Interpretation Of Diffusion Coefficients Of Proteins.

44. O. Bryngdahl, Prog. Opt., 4, 39 (1965). Applications Of Shearing Interferometry.

45. L.G. Longsworth, Phys. Tech. Biol. Res., IIA, 85 (1968). Diffusion In Liquids.

46. R.J. Goldstein, Measurement Techniques In Heat Transfer, ed. by E.R.G. Eckert and R.J. Goldstein, Ch.4, 177 (AGARDograph 130, 1970). Optical Measurement Of Temperature.

47. W. Hauf, and U. Grigull, Adv. Heat Transfer, 6, 134 (1970). Optical Methods In Heat Transfer.

48. R.N. O'Brien, Phys. Methods Chem., IIIA, ed. by A. Weissberger and R.W. Rossiter, 1 (John Wiley, 1972). Interferometry.

49. P.J. Dunlop, B.J. Steel, and J.E. Lane, Phys. Methods Chem., IV, ed. by A. Weissberger and B.W. Rossiter, 205 (John Wiley, 1972). Experimental Methods For Studying Diffusion In Liquids, Gases, And Solids.

50. R.H. Muller, Adv. Electrochem. And Electrochem. Eng., 9, 281 (1973). Double Beam Interferometry For Electrochemical Studies.

51. H. Ertl, R.K. Ghai, and F.A.L. Dullien, AIChE J., 20, 1 (1974). Liquid Diffusion Of Nonelectrolytes.

52. T.A. Anderson, Ph.D. Thesis, Michigan State University, 1968. Pure Thermal Diffusion.

53. J.D. Olson, Ph.D. Thesis, Michigan State University, 1972. Interferometric Examination Of Temperature Distributions In Liquids: Refractive Index And Thermal Conductivity.

54. NBS Special Publication 300, V. 2 (August 1968). Precision Measurement And Calibration Temperature.

55. T.J. Quinn, and J.P. Compton, Rep. Prog. Phys., 38, 151 (1975). The Foundations Of Thermometry.

56. NBS Monograph 126 (April 1972). Platinum Resistance Thermometry.

57. NBS Monograph 125 (March 1974). Thermocouple Reference Tables Based On The IPTS-68.

58. H. Svensson, Optica Acta, 1, 25 (1954). The Second Order Aberrations In The Interferometric Measurement Of Concentration Gradients.

59. R. Forsberg, and H. Svensson, Optica Acta, 2, 90 (1954). The Second Order Aberrations In The Interferometric Measurement Of Concentration Gradients. II: Experimental Verification Of Theory.

60. H. Svensson, Optica Acta, 3, 164 (1956). The Third Order Aberrations In The Interferometric Measurement Of Concentration Gradients.

61. K.W. Beach, R.H. Muller, and C.W. Tobias, J. Opt. Soc. Am., 63, 559 (1973). Light Deflection Effects In The Interferometry Of One Dimensional Refractive Index Fields.

62. D.T. Moore, J. Opt. Soc. Am., 65, 451 (1975). Ray Tracing In Gradient Index Media.

63. E.A. McLean, L. Sica, and A.J. Glass, Appl. Phys. Letters, 13, 369 (1968). Interferometric Observation Of Absorption Induced Index Change Associated With Thermal Blooming.

64. M. Giglio, and A. Vendramini, Appl. Phys. Letters, 25, 555 (1974). Thermal Lens Effect In A Binary Liquid Mixture: A New Effect.

65. J.P. Gordon, R.C.C. Leite, R.S. Moore, S.P.S. Porto, and J.R. Whinnery, J. Appl. Phys., 36, 3 (1965). Long Transient Effects In Lasers With Inserted Liquid Samples.

66. J.R. Whinnery, Acc. Chem. Res., 7, 225 (1974). Laser Measurement Of Optical Absorption In Liquids.

67. L.R. Bissonnette, Appl.Opt., 12, 719 (1973). Thermally Induced Nonlinear Propagation Of A Laser Beam In An Absorbing Fluid Medium.

68. G. Thomaes, J. Chem. Phys., 25, 32 (1956). Thermal Diffusion Near The Critical Solution Point.

69. M. Giglio, and A. Vendramini, Phys. Rev. Letters, 34, 561 (1975). Thermal Diffusion Measurements Near A Consolute Critical Point.

70. W. Pauli, Optics And The Theory Of Electrons, ed. by C.P. Enz (MIT Press, 1973).

71. F.B. Hildebrand, Methods Of Applied Mathematics, 2nd Edition (Prentice-Hall, 1965).

72. S.R. De Groot, and P. Mazur, Non-Equilibrium Thermodynamics, (North-Holland, 1969).

73. R. Haase, Thermodynamics Of Irreversible Processes, (Addison-Wesley,1969).

74. L.D. Landau, and E.M. Lifshitz, Fluid Mechanics, (Pergamon Press, 1959).

Chapter 4 References

1. J. Fourier, Theorie Analytique de la Chaleur, 1822; translated by A. Freeman, 1878; Dover, 1955.

2. O.K. Bates, Ind. Eng. Chem., 25, 431 (1933). Thermal Conductivity of Liquids.

3. L.G. Longsworth, J. Phys. Chem., 61, 1557 (1957). The Temperature Dependence of the Soret Coefficient of Aqueous Potassium Chloride.

4. H. Poltz, Int. J. Heat Mass Transfer, 8, 515 (1965). Die Warmeleitfahigkeit von Flussigkeiten II.

5. H. Poltz, Int. J. Heat Mass Transfer, 8, 609 (1965). Die Warmeleitfahigkeit von Flussigkeiten III.

6. H. Poltz and R. Jugel, Int. J. Heat Mass Transfer, 10, 1075 (1967). Thermal Conductivity of Liquids IV.

7. H. Poltz, NBS Special Publication 302 (September 1968). Some Aspects Concerning Thermal Conductivity Data of Liquids and Proposals for New Standard Reference Materials.

8. J.L. Novotny and J. C. Bratis, J. Quant. Spectrosc. Radiat. Transfer, 12, 901 (1972). Radiative Transfer in Liquid CCl_4.

9. J.L. Novotny, D.E. Negrelli, and T. Van den Driessche, J. Heat Transfer, 96, 27 (1974). Total Band Absorption Models for Absorbing-Emitting Loquids: CCl_4.

10. G. Schodel and U. Grigull, Heat Transfer, 3, R2.2 (Elsevier, Amsterdam, 1970). Kombinierte Warmeleitung und Warmestrahlung in Flussigkeiten.

11. J.D. Olson and F.H. Horne, J. Chem. Phys., 58,2321 (1973). Direct Determination of Temperature Dependence of Refractive Index of Liquids.

12. J.D. Olson, Ph.D. Thesis, Michigan State University, 1972. Interferometric Examination of Temperature Distributions in Liquids: Refractive Index and Thermal Conductivity.

13. T.V. Gurenkova, P.A. Norden, and A.G. Usmanov, J. Eng. Phys.(USSR), 24, 940 (1973). On the Question of the Influence of Radiation on the Thermal Conductivity of Plane Layers of Liquids.

14. R.M. Waxler, C.E. Weir, H.W. Schamp, Jr., J. Research NBS, 68A, 489 (1964). Effect of Pressure and Temperature Upon the Optical Dispersion of Benzene, Carbon Tetrachloride, and Water.

15. E. Reisler, H. Eisenberg, A.P. Minton, J.C.S. Faraday II, 68, 1001 (1972). Temperature and Density Dependence of the Refractive Index of Pure Liquids.

16. B.L. Johnson and J. Smith, Refractive Indices and Densities of Some Common Polymer Solvents, p. 27, in Light Scattering From Polymer Solutions, ed. by M.B. Huglin (Academic Press, 1972).

17. E. McLaughlin, Chem. Rev., 64, 389 (1964). The Thermal Conductivity of Liquids and Dense Gases.

18. N.V. Tsederberg, Thermal Conductivity of Gases and Liquids, (M.I.T. Press, 1965).

19. R.W. Powell, C.Y. Ho, and P.E. Liley, Thermal Conductivity of Selected Materials, (NSRDS-NBS 8, November 1966).

20. R.W. Wood, Physical Optics, (MacMillan, 1934).

21. E. Reisler and H. Eisenberg, J. Chem. Phys., 43, 3875 (1965). Refractive Indices and Piezo-Optic Coefficients of Deuteruim Oxide, Methanol, and Other Pure Liquids.

22. E. Hecht and A. Zajac, Optics, (Addison-Wesley, 1975).

23. Handbook of Chemistry and Physics, 49th Edition (Chemical Rubber Co., 1968).

24. U.W. Hochstrasser, in Handbook of Mathematical Functions, ed. by M. Abramowitz and I.A. Stegun (Dover, 1968). Orthogonal Polynomials.

25. L.W. Tilton and J.K. Taylor, J. Research NBS, 20, 419 (1938). Refractive Index and Dispersion of Distilled Water For Visible Radiation at Temperatures 0 to 60 °C.

26. J.B. Hawkes and R.W. Astheimer, J. Opt. Soc. Am., 38, 804 (1948). The Temperature Coefficient of the Refractive Index of Water.

27. R.M. Waxler and C.E. Weir, J. Research NBS, 67A, 163 (1963). Effect of Pressure and Temperature on the Refractive Indices of Benzene, Carbon Tetrachloride, and Water.

28. S.D.H. Andreasson, S.E. Gustafsson, and N. Halling, J. Opt. Soc. Am., 61, 595 (1971). Measurement of the Refractive Index of Transparent Solids and Fluids.

29. H.M. Dobbins and E.R. Peck, J. Opt. Soc. Am., 63, 318 (1973). Change of Refractive Index of Water as a Function of Temperature.

30. O. Bryngdahl, Ark. Fys., 21, 289 (1961). Genaue Bestimmungen der Warmeleiteigenschaften in Flussigkeiten mit einer Scherinterferometrischen Methode.

31. P.R. Bevington, Data Reduction and Error Analysis For the Physical Sciences, (McGraw-Hill, 1969).

32. G.W. Snedecor and W.G. Cochran, Statistical Methods, (Iowa State University Press, 1967).

33. J.B. Hawkes and R.W. Astheimer, J. Opt. Soc. Am., 64, 105 (1974). Optical Properties of Water in the Neighborhood of 35°C.

34. G. Andaloro, M.B.P. Vittorelli, and M.U. Palma, J. Soln. Chem., 4, 215 (1975). Anomalies in the Temperature Dependence of the 1.2u Absorption of Liquid Water.

35. C.W. Robertson, B. Curnutte, and D. Williams, Mol. Phys., 26, 183 (1973). The Infra-Red Spectrum of Water.

36. S. Chandrasekhar, Radiative Transfer, (Dover, 1960).

37. R.M. Goody, Atmospheric Radiation I. Theoretical Basis, (Oxford, 1964).

38. R.D. Cess, Ad. Heat Transfer, 1, 1 (1964). The Interaction of Thermal Radiation with Conduction and Convection Heat Transfer.

39. D.H. Sampson, Radiative Contributions to Energy and Momentum Transport in a Gas, (Interscience, 1965).

40. C.L. Tien, Ad. Heat Transfer, 5, 254 (1968). Thermal Radiation Properties of Gases.

41. R.D. Cess and S.N. Tiwari, Ad. Heat Transfer, 8, 229 (1972). Infrared Radiative Energy Transfer in Gases.

42. R. Viskanta and E.E. Anderson, Ad. Heat Transfer, 11, 318 (1975). Heat Transfer in Semitransparent Solids.

43. G.C. Pomraning, Prog. High Temp. Phys. and Chem., 4, 1 (1971). High Temperature Radiative Transfer and Hydrodynamics.

44. G.C. Pomraning, The Equations of Radiation Hydrodynamics, (Pergamon Press, 1973).

Chapter 5 References

1. H. Bénard, Ann. Chim. Phys., 23, 62 (1901). Les Tourbillons Cellulaires dans une Nappe Liquide Transportant de la Chaleur par Convection en Regime Permanent.

2. J.R.A. Pearson, J. Fluid Mech., 4, 489 (1958). On Convection Cells Induced by Surface Tension.

3. D.A. Nield, J. Fluid Mech., 19, 341 (1964). Surface Tension and Bouyancy Effects in Cellular Convection.

4. D.A. Nield, J. Fluid Mech., 71, 441 (1975). The Onset of Transient Convection Instability.

5. S. Chandrasekhar, Hydrodynamic and Hydromagnetic Stability, (Oxford, 1961).

6. W.V.R. Malkus, Proc. Roy. Soc., A 225, 185 (1954). Discrete Transitions in Turbulent Convection.

7. J.W. Deardorff and G.E. Willis, J. Fluid Mech., 28, 675 (1967). Investigation of Turbulent Thermal Convection between Horizontal Plates.

8. J. Gille, J. Fluid Mech., 30, 371 (1967). Interferometric Measurement of Temperature Gradient Reversal in a Layer of Convecting Air.

9. H.T. Rossby, J. Fluid Mech., 36, 309 (1969). A Study of Benard Convection with and without Rotation.

10. R. Krishnamurti, J. Fluid Mech., 42, 295 (1970). On the Transition to Turbulent Convection. I. The Transition from Two-to Three-Dimensional Flow.

11. R. Krishnamurti, J. Fluid Mech., 42, 309 (1970). On the Transition to Turbulent Convection. II. The Transition to Time-Dependent Flow.

12. R. Farhadieh and R.S. Tankin, J. Fluid Mech., 66, 739 (1974). Interferometric Study of Two-Dimensional Benard Convection Cells.

13. L.A. Segel, in Nonequilibrium Thermodynamics, Variational Techniques, and Stability, ed. by Donnelly, Herman, and Prigogine, (University of Chicago Press, 1966).

14. E.L. Koschmieder, Advan. Chem. Phys., 26, 177 (1973). Benard Convection.

15. J.S. Turner, Buoyancy Effects in Fluids, (Cambridge, 1973).

16. P.H. Roberts, Advan. Chem. Phys., 32, 17 (1975). Concepts in Hydrodynamic Stability Theory.

17. J.A. Whitehead, Jr., in Fluctuations, Instabilities, and Phase Transitions, ed. by T. Riste, (Plenum, 1975). A Survey of Hydrodynamic Instabilities.

18. M.G. Velarde, in Hydrodynamics, ed. by R. Balian, (Gordon and Breach, 1974).

19. R. Graham, Springer Tracts Mod. Phys., 66,1 (1973). Statistical Theory of Instabilities in Stationary Nonequilibrium Systems with Applications to Lasers and Nonlinear Optics.

20. R. Graham, Phys. Rev., A 10, 1762 (1974). Hydrodynamic Fluctuations Near the Convection Instability.

21. H. Haken, Rev. Mod. Phys., 47, 67 (1975). Cooperative Phenomena in Systems Far from Thermal Equilibrium and in Nonphysical Systems.

22. G.S. Kell, J. Chem. Eng. Data, 20, 97 (1975). Density, Thermal Expansion, and Compressibility of Liquid Water from 0° to 150°C: Correlations and Tables for Atmospheric Pressure and Saturation Reviewed and Expressed on 1968 Temperature Scale.

23. E. McLaughlin, Chem. Rev., 64, 389 (1964). The Thermal Conductivity of Liquids and Dense Gases.

24. Handbook of Chemistry and Physics, 49 (Chemical Rubber Co., 1968).

25. G. Veronis, J. Fluid Mech., 26, 49 (1966). Large Amplitude Benard Convection.

26. R.J. Schmidt and S.W. Milverton, Proc. Roy. Soc., A 152, 586 (1935). On the Instability of a Fluid when Heated from Below.

27. R.J. Schmidt and D.A. Saunders, Proc. Roy. Soc., A 165, 216 (1938). On the Motion of a Fluid Heated from Below.

28. P.L. Silveston, Forsch. Ing. Wes., 24, 59 (1958). Warmedurchgang in Waagerechten Flussigkeitsschichten.

29. J. Gille and R. Goody, J. Fluid Mech., 20, 47 (1964). Convection in a Radiating Gas.

30. H.A. Thompson and H.H. Sogin, J. Fluid Mech., 24, 451 (1966). Experiments on the Onset of Thermal Convection in Horizontal Layers of Gases.

31. F.H. Lange, Correlation Techniques, (D. Van Nostrand, 1967).

32. S. Panchev, Random Functions and Turbulence, (Pergamon Press, 1971).

33. D.C. Champeney, Fourier Transforms and Their Physical Applications, (Academic Press, 1973).

34. P.J. Davis and I. Polonsky, in Handbook of Mathematical Functions, ed. by M. Abramowitz and I.A. Stegun, p. 875 (Dover, 1968). Numerical Interpolation, Differentiation and Integration.

35. J.W. Elder, J. Fluid Mech., 32, 69 (1968). The Unstable Thermal Interface.

36. J.W. Elder, J. Fluid Mech., 35, 417 (1969). The Temporal Development of a Model of High Rayleigh Number Convection.

37. F.H. Busse, J. Math. Phys., 46, 140 (1967). On the Instability of Two-Dimensional Convection in a Layer Heated from Below.

38. F.H. Busse, J. Fluid Mech., 52, 97 (1972). The Oscillatory Instability of Convection Rolls in a Low Prandtl Number Fluid.

MICHIGAN STATE UNIVERSITY LIBRARIES
3 1293 03082 4209